Unbonded Pre-tensioned Bridge Columns with Rocking Detail

Jeffrey Schaefer

A thesis
submitted in partial fulfillment of the
requirements for the degree of

Master of Science in Civil Engineering

University of Washington
2013

Committee:
Marc Eberhard
John Stanton
Michael Motley

Program Authorized to Offer Degree:
Civil Engineering

UNIVERSITY OF WASHINGTON

ABSTRACT

Unbonded Pre-tensioned Bridge Columns with Steel Rocking Shells

JEFFREY SCHAEFER

CHAIR OF THE SUPERVISORY COMMITTEE:

PROFESSOR MARC O. EBERHARD

CIVIL ENGINEERING

A new pre-tensioned precast bridge system has been developed that provides seismic regions the means to construct high-performance bridges that can be built quickly. The columns are designed to rock as rigid bodies, and their ends are protected against damage by a steel shoe detail. The precast feature of the system will reduce traffic delays by moving construction off-site. The pretensioning feature leads to reduced residual displacements after an earthquake. The use of epoxy-coated strands and the quality control available in a precasting plant lead to enhanced durability.

The seismic performance of the system was evaluated with pseudo-static tests of two column-footing sub-assemblies. In one column-footing sub-assembly, a ductile fiber-reinforced concrete (HyFRC developed by Ostertag) was used to fill the steel shoe and the region immediately above it. This column also contained a steel dowel bar that extended down from the

body of the column into the footing. The other column did not possess any ductile concrete or dowel bar. During the tests, the columns had very low residual displacements and negligible damage to the concrete, even after being subjected to drift ratios of over 10%.

ACKNOWLEDGMENTS

This research was supported by the Pacific Earthquake Engineering Facility (PEER) Center and the National Science Foundation for Earthquake Engineering Research Program (Award #1207903). Any opinions, findings, and conclusions or recommendations expressed in this material are those of the authors and do not necessarily reflect those of the funding agencies.

This project would not have been possible without the help from my wife Rachel Schaefer, and colleagues Travis Thornstad, Olafur Haraldson, Bryan Kennedy and other graduate students at the University of Washington. Additional support was provided by Vince Chaijaroen, Structural Laboratory Manager at the University of Washington.

CONTENTS

LIST OF FIGURES

LIST OF TABLES

1 Introduction

This report describes the development and experimental testing of the column-to-footing connection for a new bridge bent system. The advantages of this system, as compared to its conventional counterpart, include:

- accelerated bridge construction,
- improved seismic performance through re-centering,
- forestalling of column spalling and bar buckling, and
- delayed bar fracture.

Figure 1.1. illustrates the developed system schematically.

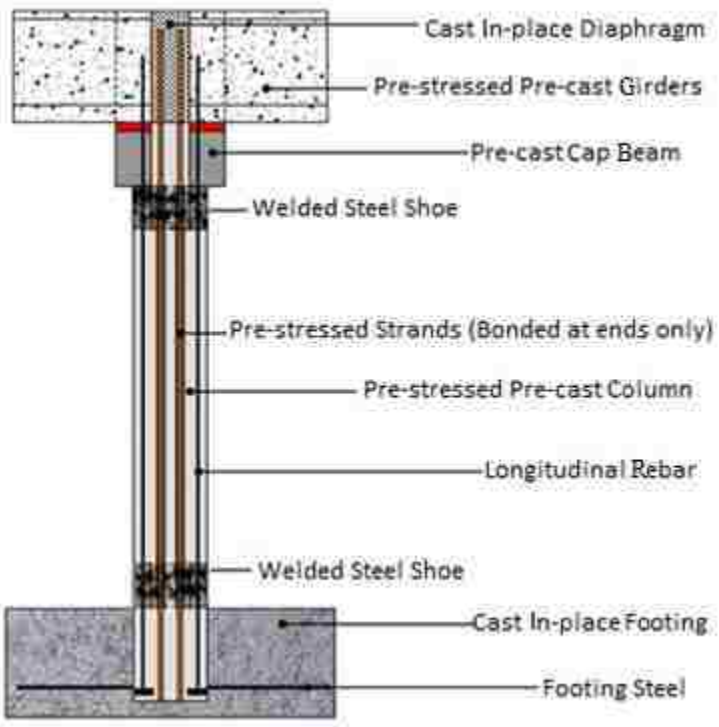

Figure 1.1 Elevation of pre-stressed concrete column system.

The most significant differences between this bridge bent system and a conventional, cast-in-place reinforced concrete bent system are:

- The columns and beams are precast to accelerate construction (Section 1.1).

- The system uses a wet socket connection (Haraldsson et al. 2011) between the column and the cast-in-place footing (Section 1.2).
- The system combines a grouted-duct connection between the column and the precast crossbeam (Pang et al. 2008) and a reduced column section that extends into the cap beam (Davis et al. 2011) (Section 1.2).
- Unbonded pre-stressing tendons run through the length of the column to encourage post-earthquake re-centering (Davis et al. 2011) (Section 1.3).
- A steel shoe encases the concrete in each plastic-hinge region to concentrate earthquake-induced rotations at a single location (Section 1.4).
- One version of the system includes Hybrid Fiber Reinforced Concrete (HyFRC) in the regions of expected deformation concentrated (Section 1.5).

1.1 PRECASTING COMPONENTS TO ACCELERATE BRIDGE CONSTRUCTION

A precast bridge system has many advantages over one that is cast in-place to the economy, the environment and public safety. In precast bridge construction, the structural components are fabricated off-site. This feature reduces the amount of time workers need to spend on-site, which decreases the duration of road and lane closures. The resulting increased traffic flow due to the shortened on-site construction time will decrease commute times and gas consumption, resulting in additional savings, and will also reduce harmful emissions released into the atmosphere (Khaleghi et al. 2012). Lastly, fabrication within a manufacturing facility leads to better quality control.

Despite the advantages of precast bridge systems, some agencies in seismically active regions have been reluctant to adopt them. States with seismic hazards, such as Washington State, have used precast bridge girders for more than fifty years (Khaleghi et al., 2012), but rarely have such agencies used precast bridge columns or cap beams. The reluctance to use the latter is driven by the high-performance demands of the beam-to-column connection and by traditional contractor preference. During an earthquake, these connections experience the highest deformations and forces. Designing a connection to withstand such loading is a difficult challenge, particularly if the bridge elements are precast and inherently separate. Additionally, contractors generally are more experienced and comfortable with cast-in-place systems, causing them to hesitate before using a precast system.

To demonstrate the constuctibility of the new system, the State of Washington Department of Transportation (with the support of the Federal Highway Administration) worked with a contractor to implement non-prestressed precast bents in a bridge over Interstate 5 (Khaleghi et al., 2012). A pre-tensioned version of the system would use similar connection details and so be equally constructible.

1.2 SOCKET CONNECTIONS

A bridge column-to-footing socket connection was developed at the University of Washington in collaboration with Berger/ABAM Engineers, Concrete Technology Corporation, Tri-State Construction and the Washington State Department of Transportation (WSDOT) (Haraldsson et al., 2011). It contained no prestressing, but it was subsequently adapted for use with pre-tensioned columns (Davis et al, 2012). In a conventional cast in-place column, the longitudinal reinforcement at the base of the column is bent out and anchored into the cast-in-place footing. In a precast system, three alternatives are available:

- Construct the precast column with steel protruding laterally outwards at its base, and embed it in a cast-in-place footing.
- Construct the column with holes through which footing steel can pass, then cast the footing in place around the column.
- Construct the footing first, with protruding vertical starter bars that connect to the column's longitudinal reinforcement via grouted-sleeve connectors.

The first option would make transportation of the column to the jobsite extremely difficult, as the protruding steel would be awkward to stack and would pose a safety hazard. The second option would require very tight tolerances and would lead to a cumbersome erection process . The third option also requires small tolerances and constructability challenges. Additionally, the third option results in undesirably high strain concentrations in the footing reinforcement due to the high stiffness of the splice-sleeve connectors. While industry uses the third option often, researchers sought a better solution.

As a result, researchers developed a new connection, the "wet socket" connection. In this connection, the precast column is set in the excavation, the footing steel is placed, and then the footing concrete is cast. The column has straight longitudinal reinforcement, developed using anchor heads at the end of the reinforcing bars. This is a variant on the "dry socket" connection, in which the column is aligned and inserted into an opening in the previously cast footing. Grout is then introduced to fill the gap between the column and footing faces. This dry connection is currently used in parts of Europe, Japan and New Zealand (Osanai 1996). The wet socket connection differs in that the footing is cast in place after the column has been placed, and its use eliminates the need to form an opening in the footing and grout it later. Additionally, the surface of the precast column is mechanically roughened where it is in contact with the cast-in-place concrete of the footing. . This roughening increases the friction between the two interfaces enough that the column forces are adequately transferred into the footing.

The construction process of the wet socket column connection is straightforward (Figure 1.2). First, contractors excavate the ground. Then they place the footing rebar and erect the column. Since the column contains only straight longitudinal rebar with nothing protruding, the column fits easily into the opening in the footing rebar. Once the column is erected, the footing concrete is cast and allowed to gain strength. After the footing gains sufficient strength, the precast cap beam is lowered onto the column, and the ducts are grouted.

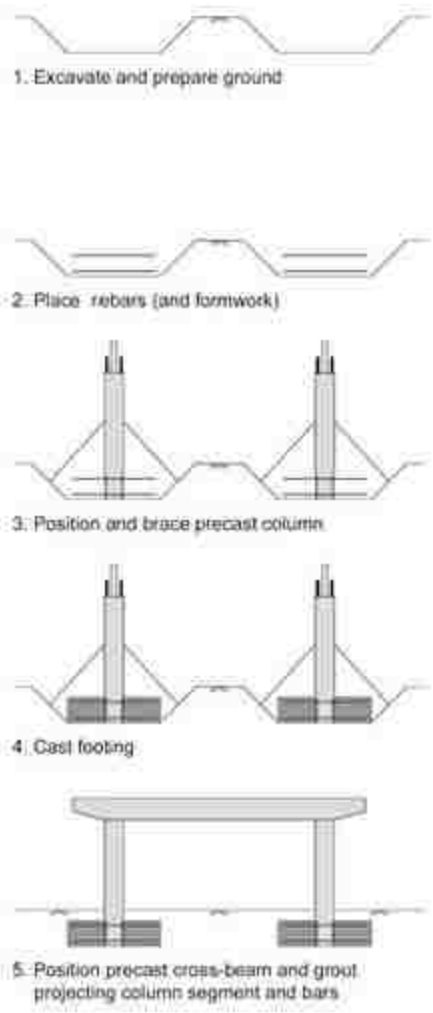

Figure 1.2 The process of using socket connection to accelerate construction.

A variation of the dry socket connection is used at the top of the column (Figure 1.3). Instead of the entire column extending into the precast cap beam, which would greatly decrease the cross beam area and strength, a reduced portion of the column is roughened and protruded upwards (Davis et al., 2011) supplemented by the extension of the longitudinal reinforcement into grouted ducts (Pang et al., 2009).

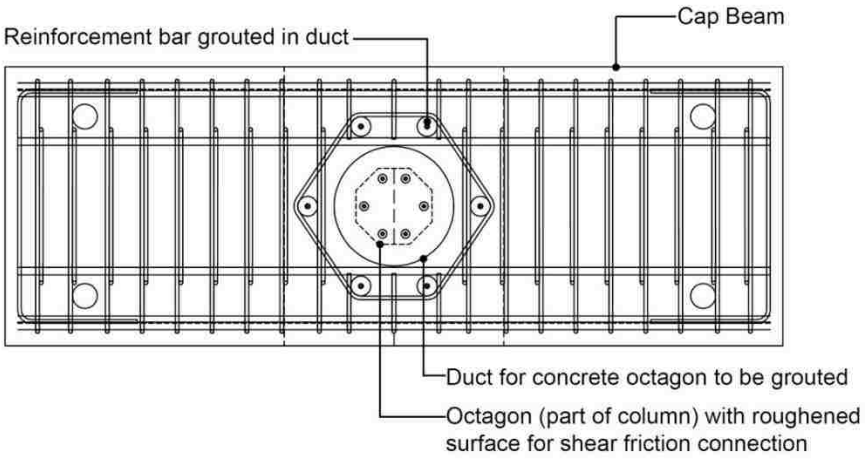

Figure 1.3 Main parts of column to cap beam socket connection.

1.3 UNBONDED PRESTRESSING TO REDUCE RESIDUAL DISPLACEMENTS

Residual displacements of bridges can hinder recovery efforts in seismically active regions. It is uneconomical to design a conventional structure to remain elastic throughout the duration of a severe earthquake; however, when a structure yields, it becomes permanently deformed, meaning that it typically will not return to its initial position after the loading is removed. This behavior is characteristic of conventional reinforced concrete systems (Figure 1.4a). This permanent deformation (residual displacement) is undesirable, because it can cause loss of function in the structure, particularly in bridges where a deformed surface (or joint interface) could make the road impassable. Furthermore, repairing bridges with residual displacements can be costly.

As a result, researchers have sought out methods for improving structural performance under intense cyclic loading and reducing residual displacements. One such method is the use of unbonded pre-stressing tendons (e.g., Cohagen et al., 2008). In this method, strands are stressed so that they provide a restoring force that re-centers the column after loading is removed (Figure 1.4b). For this strategy to be effective, however, the strands themselves must remain elastic throughout the loading. To achieve this, the stressed strands must be debonded so that the elongation caused by rocking can be distributed over a sufficient length to keep the stress in the strands below their yield stress.

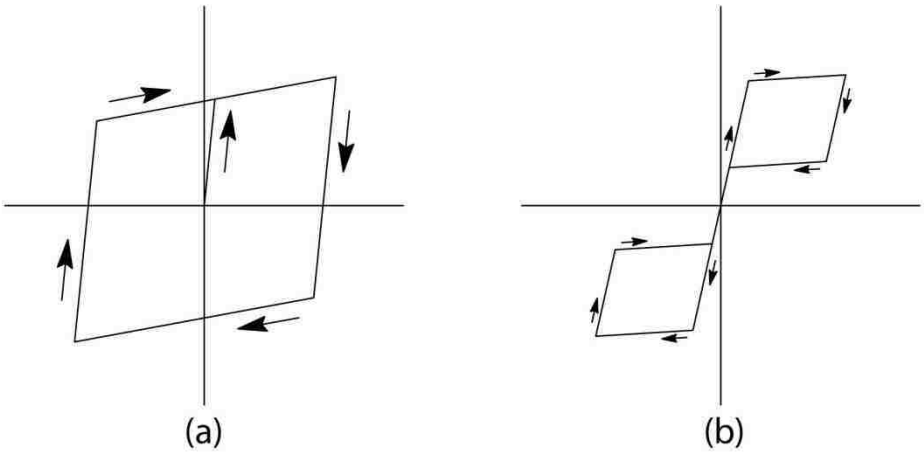

Figure 1.4 **Theoretical cyclic load-deflection curves for both traditional reinforced concrete system (a) and unbonded prestressed concrete system (b) (adapted from Stanton et al., 1997).**

The strands can be stressed either before or after casting the concrete. In pre-tensioned systems, the strands are stressed prior to concrete casting and transfer their load to the concrete through bond alone. Conversely, in post-tensioned systems, the strands are stressed after concrete casting and transfer their load via mechanical anchors, rendering concrete bond unnecessary.

University of Washington researchers have experimented with both methods: Cohagen et al. (2008) tested a post-tensioned system, and Davis et al. (2011) tested a pre-tensioned one. In Cohagen's system, the reinforced concrete column contained a single, unbonded, post-tensioned bar in its middle with a mechanical anchor at each end. The column was connected to a cap-beam using the large-bar-to-duct connection prescribed in Pang et al. (2008). Cohagen's system re-centered better than a conventional reinforced concrete system (Figure 1.5). Similarly, Davis' pre-tensioned system also improved the re-centering performance (Figure 1.6). In fact, Davis' system re-centered even better than Cohagen's system. Aside from the increased re-centering, pre-tensioning enables the stressing process to take place in a precast plant, which reduces on-site construction time. Furthermore, since pre-tensioned columns do not have mechanical anchors, they are viewed as more resistant to corrosion. Pre-tensioned bridge girders have been used since the 1950s and have shown almost no corrosion problems.

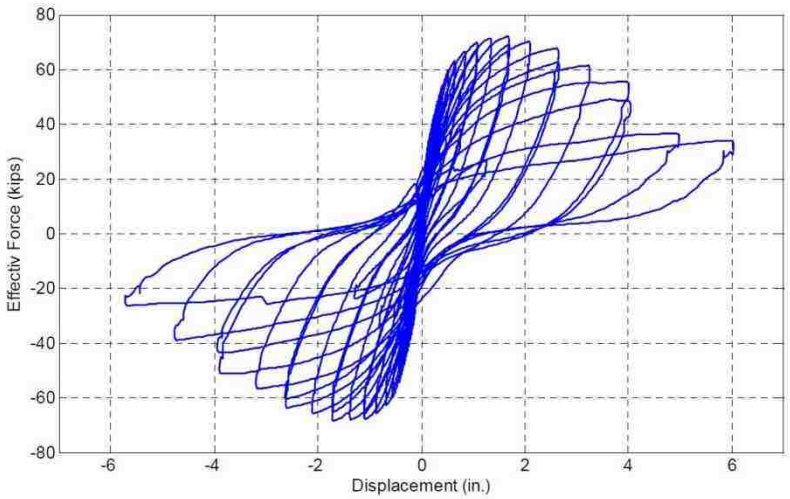

Figure 1.5 Effective lateral force versus lateral displacement, Cohagen et al. (2008).

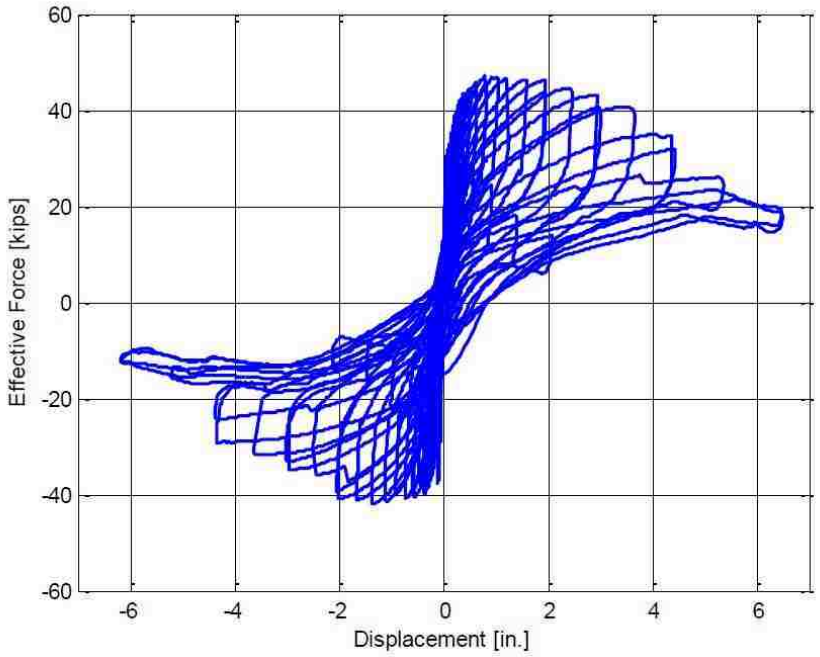

Figure 1.6 Effective lateral force versus lateral displacement, Davis et al. (2011).

1.4 STEEL SHOE ROCKING COLUMN

Confinement can increase the compressive strength of concrete. Concrete, having a comparatively high compressive strength (compared to its tensile strength), generally fails along a shear plane, even when subjected to pure compression. When confined, concrete will not slip along this shear plane unless higher than normal compressive loads are applied. This material property is exploited in structural systems such as concrete filled tubes (CFTs), in which a steel

shell confines the concrete, preventing it from failing in shear, while the concrete provides stability to the steel shell, preventing it from buckling (Fam et al. 2004, Roeder et al. 2010).

In the system developed here, the concept of confinement is used to improve upon the performance and constructability of the columns developed in Davis et al. (2011) and Finnsson et al. (2013). In this study, the columns have a steel shoe (consisting of a thin-walled tube welded to an annular plate) that encases the potential plastic hinge region (Figures 1.7 and 1.8). The confinement provided by the steel shoe was added to prevent the concrete at the column-footing interface from spalling.

Two sets of longitudinal bars are used. The first set, here called “through-bars”, extend over the entire length of the column. They act in much the same way as bars in a conventional column, and they yield alternately in tension and compression to provide both strength and energy dissipation. They pass through holes in the annular plate and are debonded locally near the footing-column interface to reduce the strain concentration there. Additional, shorter, reinforcing bars are also welded to the shoe. They extend upwards into the column, resulting in an increased moment capacity in the region immediately above the interface, which forces the crack to occur at the interface. The confined region therefore acts rigidly, causing the column to rock rather than to deform inelastically. As a result, the total energy dissipation is concentrated in the plastic deformation of the reinforcing through-bars.

One potential problem with this design is the shear strength at the column-footing interface. To investigate whether the column needs additional resistance to sliding shear, one column in this study (the one containing HyFRC) contained a dowel bar at its center, extending 8 inches above and 3 inches below the column-footing interface (Figures 1.7 and 1.8). The dowel bar was short in length so that it would not bend and deform during loading, which would counteract the re-centering ability of the prestressing strands. To prevent deformation due to bending further, the dowel was placed inside a cup socket that inhibits translation but allows rotation. The other column, which contained the dowel bar, acquired its shear capacity from friction and longitudinal reinforcing bars alone.

Figure 1.7 Plan view of Steel Shoe feature and Dowel Bar.

Figure 1.8 Elevation view of Steel Shoe feature and Dowel Bar.

1.5 HYBRID FIBER REINFORCED CONCRETE

One potential disadvantage of pre-tensioned and post-tensioned systems is that the column typically experiences damage states (column spalling, bar buckling and bar fracture) at lower drifts than is the case in non-stressed systems. In Davis' columns, the concrete in the plastic hinge region experienced spalling earlier than predicted by conventional concrete models (Berry et al., 2004).

To reduce this premature spalling, Finnsson et al. (2013) added hybrid fiber reinforced concrete (HyFRC) to the regions in his column where the greatest moment was expected to occur: the column-footing interface and the column-cap beam interface.

HyFRC is a fiber-reinforced concrete that has a higher tensile strength and more ductile compressive behavior than conventional concretes. Developed by Ostertag et al (2012), HyFRC achieves its increased performance through the inclusion of large quantities of both steel and polymer fibers

Finnsson's columns demonstrated that the addition of HyFRC to the plastic hinge and surrounding region did delay concrete spalling, but the column eventually suffered major damage. Furthermore, this addition did not significantly delay bar buckling or bar fracture. Figure 1.9 shows the effective lateral force versus drift of his specimen containing HyFRC.

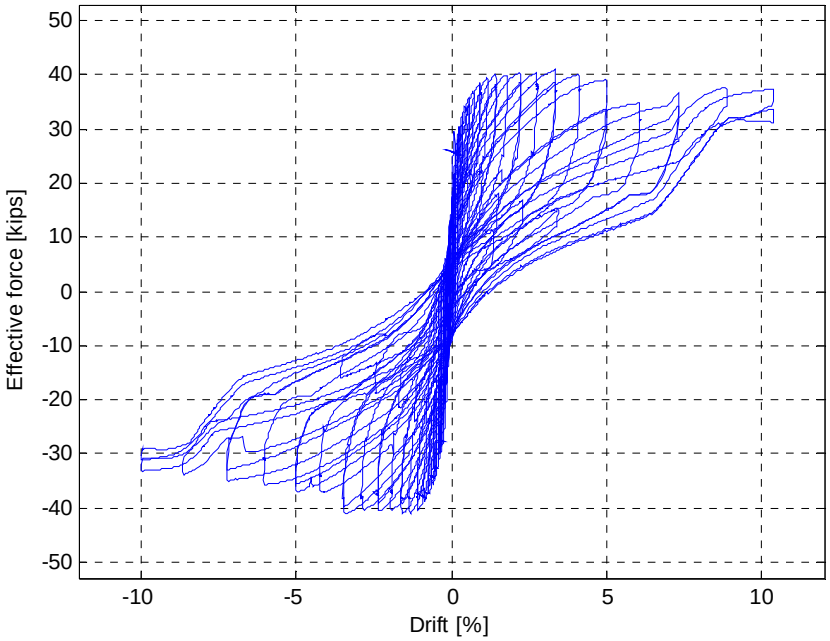

Figure 1.9 Effective lateral force versus drift, column with HyFRC, Finnsson et al. (2013).

The addition of HyFRC also complicated the construction process because the two concretes (HyFRC and conventional concrete) had to be cast separately (Figure 1.10). Since the columns were cast horizontally, a practical constraint of the pre-tensioning process, gravity could not provide the necessary separation. As a result, Finnsson first cast a HyFRC "shell" in a separate form, and then inserted it into the outer formwork. In practice, the two-stage casting process would increase labor costs.

Since the steel shoe was designed to delay concrete spalling, the same function the HyFRC served in Finnsson's columns, the inclusion of the steel shoe and HyFRC was thought to be redundant. To determine whether the tube alone would provide sufficient confinement, the two columns tested here were identical except that one contained HyFRC in the plastic hinge region and the other used conventional concrete throughout.

The column in this study that included HyFRC had a different method of construction from that of Finnsson's columns (Figure 1.10). Rather than having two separate forms, researchers poured the HyFRC and conventional concrete into one single form, separating the two pours with a wire mesh dam. While this method appeared less time-consuming and allowed for greater tolerances than the method employed by Finnsson, it still added complexity and increased the time of construction.

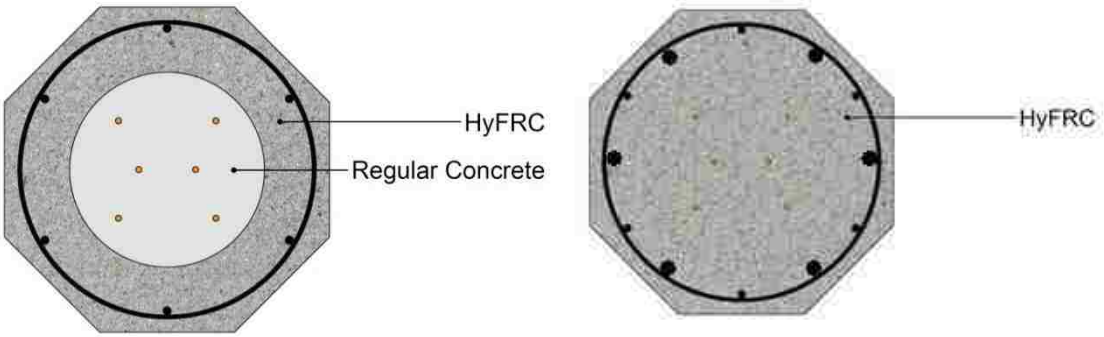

Figure 1.10 Plan view of HyFRC section for Finnsson et al. 2013 (Left) and this thesis (Right).

1.6 RESEARCH MOTIVATION, OBJECTIVES AND SCOPE

As discussed in the previous sections, laboratory tests have shown that the non-prestressed versions of the column-footing socket connection (Haraldsson et al. 2011) and the column-crossbeam grouted connection (Pang et al., 2012) provide good resistance to cyclic loading and are easy to construct. The State of Washington has used these two connections in the field, validating their constructability in practice (Khaleghi et al., 2012).

Experimental tests by Cohagen (2008) and Davis et al. (2011) demonstrated that the prestressed version of the column achieves the desired re-centering effect. However, the tests also revealed that the prestressing leads to spalling and bar buckling in the plastic hinge region that occur at lower drifts than in a comparable non-prestressed column (Davis et al., 2011). To increase the ductility of the prestressed column, Finnsson et al. (2013) introduced high-performance materials (fiber reinforced concrete and stainless steel bars) in the plastic-hinge region. Tests on these columns yielded mixed results; the fiber reinforced concrete (HyFRC) delayed spalling and, to a lesser extent, bar buckling, while the stainless steel had minimal effect on performance. Bar fracture still occured earlier than desired.

The two tests described in this report were conducted to:

- determine whether the inclusion of a steel shoe at the plastic-hinge region would improve column performance compared to that of the specimens created by Davis el at. (2011), PreT-SF-CONC, and Finnsson et al. (2013), PreT-SF-HyFRC. Specifically, the steel shoe feature was designed to delay bar buckling and bar fracture while maintaining low residual displacements and ease of construction.
- determine whether the use of HyFRC and a dowel would improve the performance over that of a rocking shoe specimen constructed with conventional concrete and without a dowel, and
- help guide the development of design procedures for this new system.

The two specimens discussed in this thesis had the same geometry as both preceeding specimens. Specimen PreT-SF-ROCK was identical to PreT-SF-CONC except that it included a steel shoe with additional welded reinforcement at its plastic-hinge region. Similarly, Specimen PreT-SF-ROCK-HyFRC was identical to PreT-SF-ROCK except for two differences. PreT-SF-

ROCK-HyFRC contained HyFRC in its plastic-hinge region while PreT-SF-ROCK contained only conventional concrete. Also, PreT-SF-ROCK-HyFRC featured a steel dowel bar that extended from its plastic-hinge region into the footing whereas PreT-SF-ROCK did not.

Chapter 2 discusses the design of the two experimental specimens, and Chapter 3 describes the experimental set up. Chapter 4 discusses the observed damage, and Chapter 5 presents the measured data. Chapter 6 contains the data analysis. Finally, Chapter 7 summarizes the research findings, and provides recommendations for practice and further research.

2 Design of Test Specimens

The research described in this report is part of a larger University of Washington program to develop bridge bent systems for seismically active regions. The primary goal of this program is to develop systems that allows for accelerated construction, lower residual displacements, reduced damage, and easy implementation into practice.

The specimens described in this chapter were developed based on the results of previous tests of column-to-footing and column-to-cap beam connections. Haraldsson et al. (2011) developed a column-to-footing connection to achieve the first goal (rapid construction). They showed that a socket connection could be constructed quickly and perform similarly as a conventional cast-in-place connection. This connection was implemented in a bridge in Washington State (Khaleghi et al. 2012).

Davis et al. (2011) developed a system to achieve the second goal (lower residual displacements) by adding unbonded pre-tensioned strands to the column. Although Davis' column reduced the residual displacements, the column experienced spalling, bar buckling and bar fracture at lower drifts than similar, conventional columns (e.g., Pang et al. 2009). To address this issue, Finnsson et al. (2013) included Hybrid Fiber-Reinforced Concrete (HyFRC) in his pre-tensioned columns in the plastic hinge region. This system also had low residual displacements. Furthermore, the HyFRC, being a more ductile material than conventional concrete, delayed concrete spalling, but the system did not delay bar buckling or bar fracture. Additionally, the incorporation of HyFRC in the column poses practical constructability issues.

The system in this thesis was developed to address all performance issues simultaneously. Like Davis et al. (2011) and Finnsson et al. (2013), the new system combines (1) precast columns and cap beams, (2) unbonded pre-tensioned columns combined with concrete, and (3) a socket connection at the base. In addition, the new system was developed to reduce damage by incorporating a steel shoe at the top and bottom connections where the maximum moment is expected to occur. The purpose of the steel shoe is to confine the concrete sufficiently so that (rather than forming a plastic hinge) the column acts as a rigid body rocking about the shoe's base. The reinforcing bars passing through the shoe are bonded over most of the height of the column and only unbonded near the column-footing (or column-cap-beam) interface. This unbonded region is included in the design to delay bar fracture. Figure 1.1 shows this system schematically.

The seismic performance of the concept described above was investigated experimentally. This chapter discusses the detailed design of two specimens representing column-to-footing connections. Specimen PreT-SF-ROCK was constructed with conventional concrete and did not include any special measures to prevent sliding along the rocking interface while specimen PreT-SF-ROCK-HyFRC included HyFRC to increase ductility and a dowel system to prevent sliding.

2.1 GEOMETRY OF TEST SPECIMENS

The specimens in this study simulated the performance of a 48" (4-ft) diameter column prototype. Due to the size limitations at the University of Washington's structures lab, the

specimens were reduced to 41.7% scale, with a diameter of 20” and a cantilever height of 60” (measured from column-footing interface to actuator mid-height). All specimen dimensions were reduced in size to meet this scale factor as close as possible.

The columns were cast horizontally, a requirement of the prestressing operation. This requirement made it difficult to cast a column with the typical circular cross-section because the top face needed to be finished with hand tools, which are not curved. As a result, an octagonal cross-section, which consisted of flat faces, was selected instead. Unlike a square cross-section, octagonal cross-sections still allow for the use of spiral transverse reinforcement, which provides a more effective distribution of confinement stresses than are provided by rectangular ties. The rationale for selecting this geometry would also apply to the full-scale prototype.

The top portion the column had a reduced section (Figure 2.1). This geometric change was a necessity because the MTS actuator that would laterally load the column needed a flat surface to attach to the column. As a result, rather than having an octagonal cross-section, the upper two feet were rectangular. This section also had four 2” diameter holes, allowing for the easy passing of threaded rod.

Figure 2.1 Reduced geometry section to accommodate actuator connection.

2.2 REINFORCEMENT

The longitudinal reinforcement consisted of conventional reinforcing steel bonded to the concrete and prestressed tendons that were unbonded over the clear height of the column. The bonded reinforcement was placed as near the outside edge of the column as possible to maximize its contribution to the column’s moment capacity. In contrast, the unbonded prestressing tendons were placed near the column’s center; a decision made due to address geometric constraints at

the column-cap beam connection to be discussed later (Sec. 2.7). Figure 2.2 shows the strand and rebar pattern used. The pattern of the strands used in the columns was the same used by Finnsson et al. (2013) and was a result of the prestressing bed geometry.

The resources available at the University of Washington's structures lab required a specialized standoff to be used in order to stress individual strands. This piece of equipment, in turn, required that the strands be spaced a distance of roughly 3". The strand pattern used accommodates this constraint while minimizing the strand pattern area.

Figure 2.2 Strand and rebar pattern used in the specimens.

The deformed bar reinforcing steel was intended to yield and dissipate energy, whereas the unbonded prestressing tendons were intended to remain elastic and re-center the column after loading was removed. To ensure the prestressing tendons remained elastic within the target level of deformation, they were encased in plastic sleeves in an unbonded region that extended from the column-footing connection to 48" up into the column. Figure 2.3 shows an elevation view of the column, which depicts this unbonded region. The unbonded region served to distribute the elongations in the tendons over a greater region, hence reducing the strain to a level below the tendon's yield strain. The re-centering force provided by the strands is a result of two design parameters: the strand's cross-sectional area and the strand's initial stress achieved through prestressing. The total energy dissipation capacity of the system is largely a factor of the deformed reinforcement bar's cross-sectional area.

The column was designed such that the prestressing strand would contribute approximately 60% of the column flexural strength, and the deformed reinforcing bar would contribute the remaining 40%. Due to this design decision, a smaller cross-sectional area of deformed bars was required in the pretensioned columns than in a conventional column with a similar flexural strength. Consequently, in the scaled test specimens, six No. 4 bars (corresponding to six No. 10 bars at full-scale) provided the necessary longitudinal

reinforcement, resulting in a reinforcement ratio of only 0.36%. Additionally, each column contained six epoxy-coated 3/8" diameter strands. This reinforcement was the same as that in columns tested by Davis et al. (2011) and Finnsson et al. (2013).

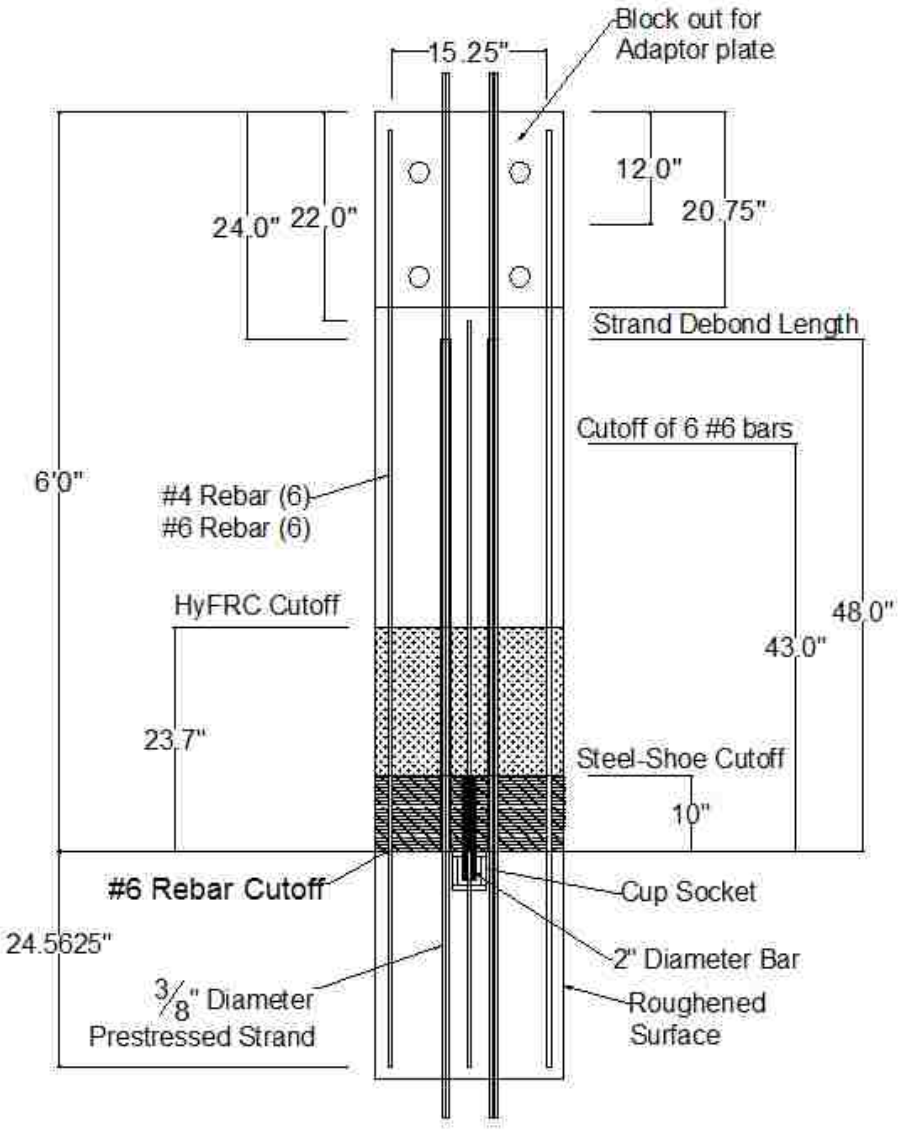

Figure 2.3 Elevation view of the specimen PreT-SF-ROCK-HyFRC.

The specimens tested in this thesis represented only the bottom connection (Figure 2.4). This modification is acceptable because the columns in the field would have an inflection point at roughly mid-height, so the columns in the field and in the lab would be expected to perform the same structurally. Furthermore, symmetry dictates that at mid-height of the column the strands in the field would not undergo strand slip relative to the concrete. As a result, the strands could be bonded in the test specimen without changing the strand behavior in the field columns.

However, since the strands require a finite bond length at the top of the column, the bond cutoff cannot be located at the point of inflection but rather 12” below it. This decreased unbonded length caused the strands in the test specimen to yield at lower drifts than they would in the corresponding field columns.

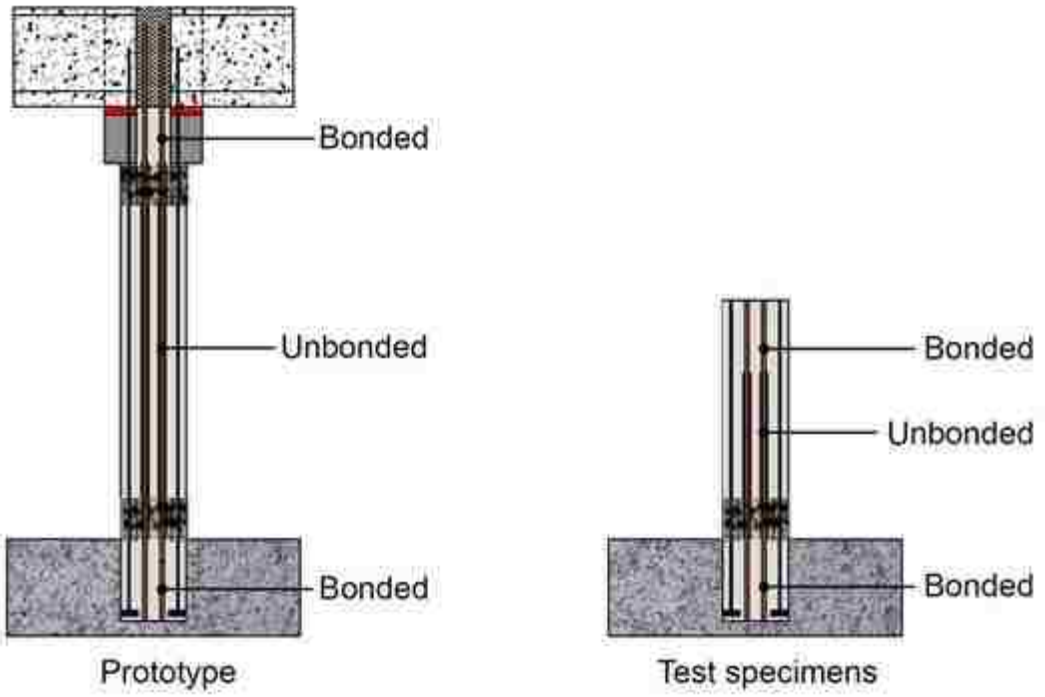

Figure 2.4 Comparison of the unbonded regions in a column in the field and the test specimens (adapted from Davis et al., 2011).

For the system to maintain its restoring force, the prestressing strands need to be anchored fully at their ends. Otherwise, the strands would slip, which would reduce their initial strain and stress, and consequently lower the potential re-centering force of the column. In order to reduce this risk, the strands were bonded 24” at the top and 24 9/16” at the bottom of the column (Figure 2.3).

For strands with an effective stress of 150 ksi, ACI 318-11 requires a development length equal to 150 times the strand’s diameter. In a cap beam with a depth of 42” (which is common), this requirement would limit the strand diameter to a maximum of 42”/150= 0.28”. But the smallest commercially available epoxy-coated strand has a diameter of 3/8” And even if they were available, such small strands would not be practical because the full-scale column would require roughly 30 strands to provide the desired re-centering force. This many strands would not fit into the reduced section of the column that extends into the cap beam. Therefore, to satisfy constructability requirements, the full-scale column needed a strand diameter of at least ½”.

A prototype strand diameter of ½” scales to 0.209” for the test specimens. As previously mentioned, 3/8” is the smallest epoxy-coated strand size available. As a result, researchers used 3/8” strand realizing that an oversized strand meant that the bond stresses would be higher in the test specimens than expected in the full-scale column. These higher stresses caused the potential for bond failure to occur.

To anchor the strands during the tests, each strand was fitted with a prestressing chuck at each end. Each strand had a load cell at its top end, in between the chuck and the column face (Figure 2.5). Using 7/8" diameter ASTM A490 bolts and a plate with welded nuts of complimentary size (STD Plate), each end of the strand was stressed to four kips by turning the bolts against the resisting chucks (Figure 2.4). During the tests, the load cell would detect any slip in the strand, while the chuck would guarantee continued anchorage. Load cells were only placed at the top of the column, because the bond length was shorter at the top end. Any slip that would occur in the footing portion of the column would occur in the actuator end, and the load cell would detect it.

Figure 2.5 Photograph (Left) and schematic (Right) views of the system to detect and prevent the strands from slipping.

2.3 ROCKING CONNECTION

The column had a special connection ("steel shoe") at the location of the column-footing interface to encourage rocking and to minimize damage. The rocking connection consisted of a shoe annular plate, a shoe wall, discontinuous welded bars, and through bars.

Shoe Annular Plate

The rocking was designed to occur on the annular plate of the shoe. The steel shoe had drilled holes in a circular pattern to allow the deformed reinforcing bars to pass through it. On a similar circular pattern (rotated by 30 degrees), No. 6 bars were welded to the interior side of the shoe's annular plate. These bars extended upwards into the column and provided extra reinforcement (both tensile and compressive) at the top of the shoe, reducing the chance of a crack plane forming at this region where the column's stiffness dramatically decreases.

Shoe Wall

To confine the concrete above the annular plate, a ¼" thick shoe wall extended one half column diameter (10") above the column-footing interface. This height was selected based off finite-element modeling conducted by Dr. Tieyi Zhong. The height corresponded to the height at which the unconfined concrete above the shoe was predicted to experience a strain below 0.003 in./in., at a drift ratio of 5%.

Discontinuous Welded-Bars

No. 6 bars were welded to the annular plate and extended 43" above the column-footing interface (Figure 2.2). This dimension was determined after considering the more stringent of two criteria: the location where the yield moment of the column after bar cutoff first exceeded the expected observed moment, and the location beyond the HyFRC cutoff in specimen PreT-SF-ROCK-HyFRC where the No. 6 bars would be fully developed. The development length criterion proved to control the cutoff point. For consistency purposes, both columns used the same cutoff length for the No. 6 bars.

Through-Bars

No. 4 bars extended the full height of the column and through the rocking connection. To delay bar fracture, the No. 4 reinforcing bars were encased in 8-in. long plastic sleeves, which extended 4" above and 4" below the interface. This unbonded region delayed bar fracture by distributing the bar elongation over the debonded length.

Figure 2.6 Steel shoe. On left is an elevation view of the shoe while on right is a bottom view of the shoe.

Dowel and Cup Socket

In specimen PreT-SF-ROCK, frictional resistance and the deformed bars alone transferred the shear forces across the column-footing interface. In specimen PreT-SF-ROCK-HyFRC, a 2" diameter steel dowel bar was designed to contribute to the shear transfer (Figure 2.7). The dowel bar was located at the center of the column's cross-section to reduce any

deformation it might experience from bending. To reduce its deformation further, the dowel bar was encased in a welded cup that allowed the bar to rotate but not slide.

Figure 2.7 Dowel bar and cup that provide shear reinforcement across the column-footing interface in specimen PreT-SF-ROCK-HyFRC.

2.4 DUCTILITY THROUGH FIBER REINFORCED CONCRETE

It was expected that the strain demands on the column concrete could met by conventional concrete. In case this capacity was inadequate, one specimen, PreT-SF-ROCK-HyFRC, did contain HyFRC. In specimen PreT-SF-ROCK-HyFRC, the HyFRC extended 24" above the column-footing interface, the location where the column's yield moment (including 6 No. 4 bars and 6 No. 6 bars) first exceeded the expected observed moment during testing. The HyFRC region used in the columns of this study was similar to that used in Finnsson's columns with a few exceptions, shown in Figure 2.9. First, the upper bound of the HyFRC region, 24" above column-footing interface, was 1" shorter than that of Finnsson's columns. Second, the lower bound of the HyFRC was at the column-footing interface whereas in Finnsson's columns, HyFRC extended into the footing 4". The HyFRC region was shortened in this study because the region used in Finnsson's columns was deemed larger than necessary. Inclusion of HyFRC in the footing provided little benefit because the level of confinement was so high that conventional concrete would be sufficient given the

anticipated footing stresses. Since HyFRC is a more expensive, less workable mix, it was replaced with conventional concrete where possible.

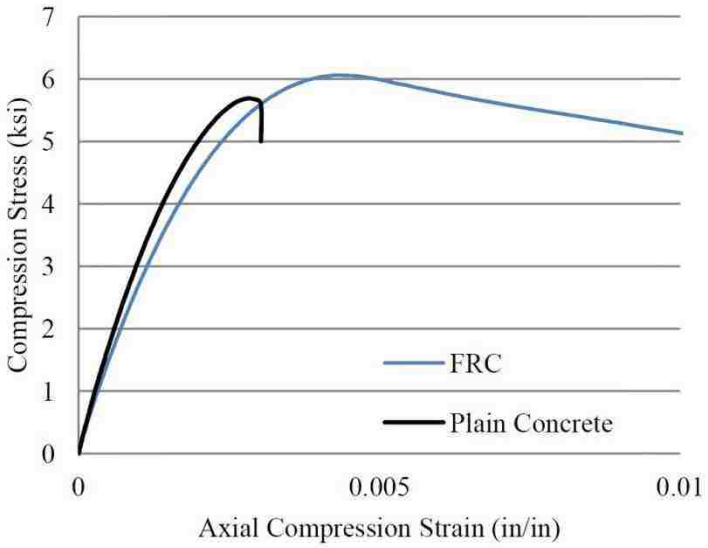

Figure 2.8 Typical axial compression stress vs. strain for HyFRC compared to conventional concrete, Ostertag et al. (2013).

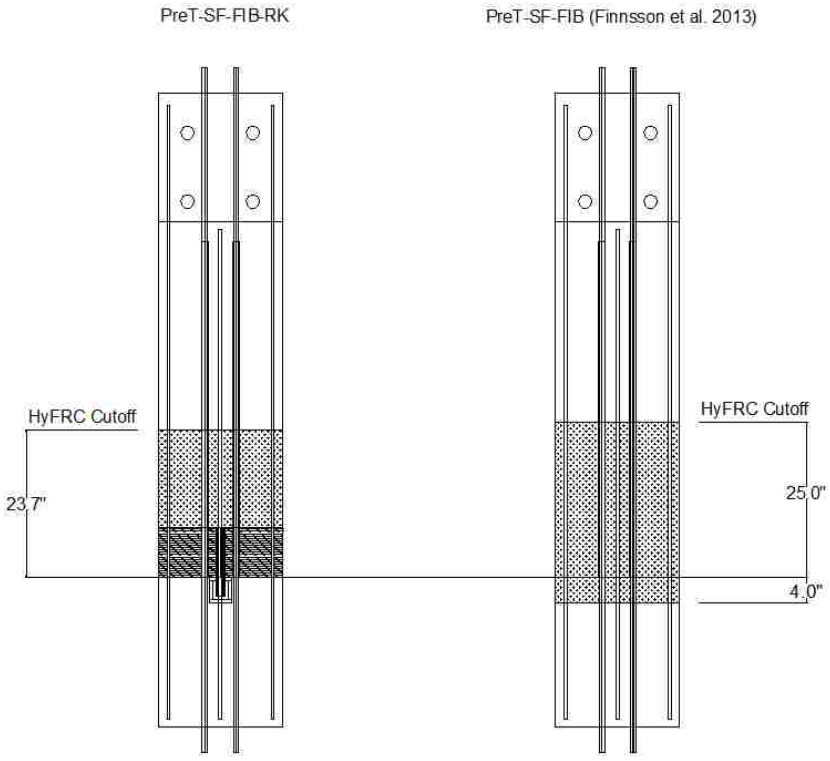

Figure 2.9 Comparison of HyFRC regions between specimen PreT-SF-ROCK-HyFRC and PreT-SF-HyFRC (Finnsson et al. 2013).

2.5 DESIGN OF SOCKET CONNECTION

Haraldsson et al. (2011) developed the socket connection so that it is possible to precast the columns of bridge bent systems in a fabrication plant and then easily transport them to a jobsite, reducing the time required onsite. Once onsite, the column is erected and a footing cast around it. Since no reinforcing bars are exposed from the column, the only means of load transfer between the column and footing is friction. To enhance the friction at this interface, the portion of the columns that extended into the footing were roughened using a saw-tooth pattern (figures 2.10 and 2.11).

Mechanical anchors were added to the bottom ends of the columns' longitudinal rebar. Normally, longitudinal rebar is anchored into the footing through bends, but that is not possible in this case where the rebar does not protrude out of the column. A strut and tie model shows that the terminator heads help transfer the diagonal strut force in the column to the vertical tension force in the rebar. This results in a CCC node, which is stronger and would likely result in improved structural performacne. Haraldsson et al. (2011) showed that this connection could be built easily and performed at least as well as a comparable conventional cast-in-place connection.

Figure 2.10 Roughened surface of the portion of the column that extends into the spread footing.

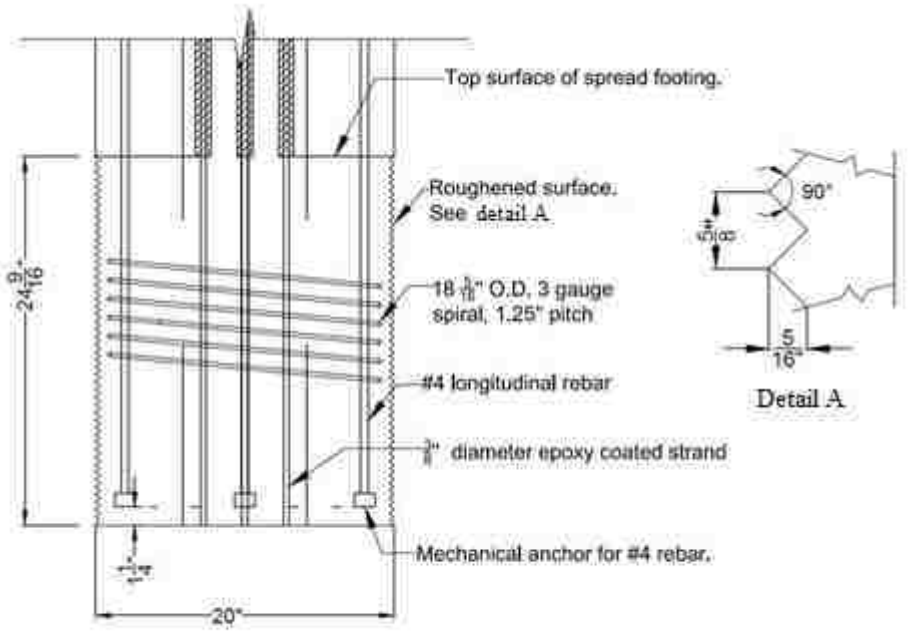

Figure 2.11 Details of the socket connection.

2.6 DESIGN OF THE SPREAD FOOTING

The design of the spread footing in this study was the same as used by Finnsson et al. (2013) with a few minor exceptions. This footing was designed according to the AASHTO Load and Resistance Factor Design Specification (2009), the AASHTO Guide Specifications for LRFD Seismic Design (2009), the WSDOT Bridge Design Manual (2008) and the Caltrans Seismic Design Criteria (2006) (Haraldsson et al. 2011). The reinforcing layout of the bottom mat is shown in Figure 2.12, and the detailed drawings of the footing can be found in Appendix B.

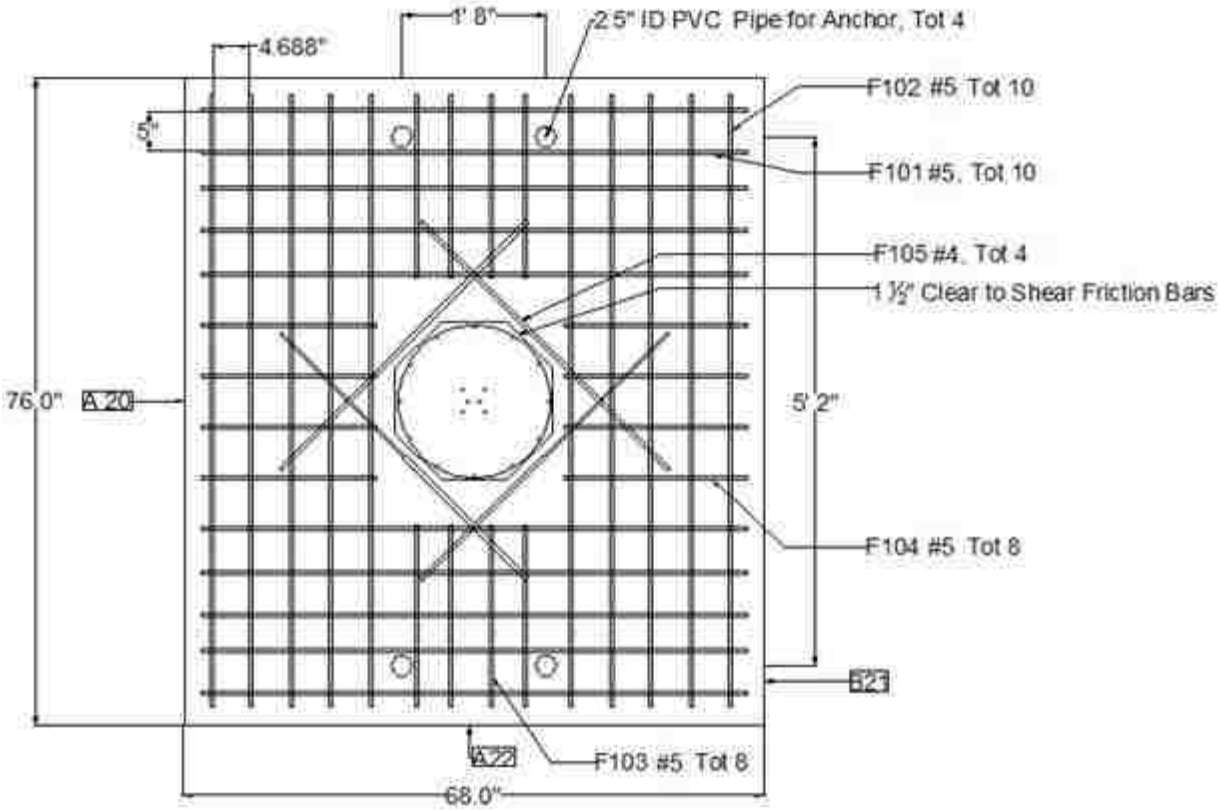

Figure 2.12 Detailed drawing of the bottom steel of the footing.

A void was needed underneath the footing for two reasons. First, it provided space for the chucks and prestressing strands beneath the column. Second, it permitted the column to fail in punching fear should this mode of failure be critical, although no columns using the socket connection have shown a failure of this type. The footing used in Finnsson's specimen contained a larger void area underneath the column than the footings in this thesis' specimens. Researchers chose to reduce the void area to improve constructability. The void height, the main parameter, was unchanged.

Unlike previous tests, the footings in these specimens did not contain any stirrups. Past results showed that the stirrups experienced very low strains and were therefore unnecessary. They were removed to simplify construction.

2.7 DESIGN OF CAP BEAM CONNECTION

The top portion of the column used the grouted connection developed in Davis et al. (2011). This thesis does not explore the structural performance of the rocking system with this connection. In his study, Davis had found the top connection to perform as well as the bottom connection. Additionally, current research at the University of Washington is investigating the performance on the top, rocking connection.

While this thesis does not investigate the performance of the cap beam connection, it is still of interest because the cap beam connection dictates the pattern of the prestressing strands. Since the cap beam is precast, the cast-in-place socket method used in the column-footing connection is unviable. Additionally bond must occur across the depth of the cap beam to maximize the unbonded length of the prestressing strands. This requires that a section of the column to extend into the cap beam. If the whole column were to extend into the cap beam, the void would be so great that either wider girders would be needed or the cap beam would experience excessive joint shear stress. Instead, a reduced section was used so that the opening in the cap beam could be small. To accommodate the reduced section, the prestressing strands were placed tightly in the center of the column.

To ensure adequate moment capacity, the deformed reinforcing bars extend into the cap beam, fitting into correctly sized ducts (Figure 2.13). Despite not meeting ACI development length requirements, Pang et al. (2008) showed that confinement provided by the ducts improves the bond so that reliable anchorage is still achieved. The ducts for the deformed reinforcing bars and the reduced concrete section are grouted once the cap beam is situated.

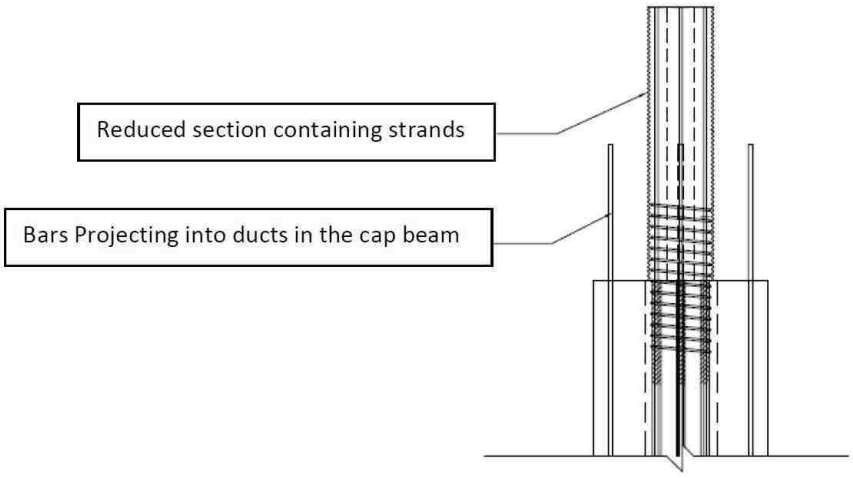

Figure 2.13 Hybrid grouted socket connection, Davis et al. (2011).

3 Experimental Setup

The columns were subjected to a series of cycles of increasing lateral displacement and a constant axial load. This chapter describes the test setup (Sec. 3.1), instrumentation (Sec. 3.2) and test protocol (Sec. 3.3)

3.1 TEST SETUP

The laboratory's 2.4-million-kip capacity Baldwin test machine applied a constant vertical load while a 220-kip capacity MTS Actuator applied a cyclic horizontal displacements as shown in Figure 3.1. The Baldwin was self-reacting whereas the MTS Actuator was bolted to a W14x90 beam, which in turn was attached to a self-reacting frame. The MTS actuator had a peak-to-peak stroke of two feet.

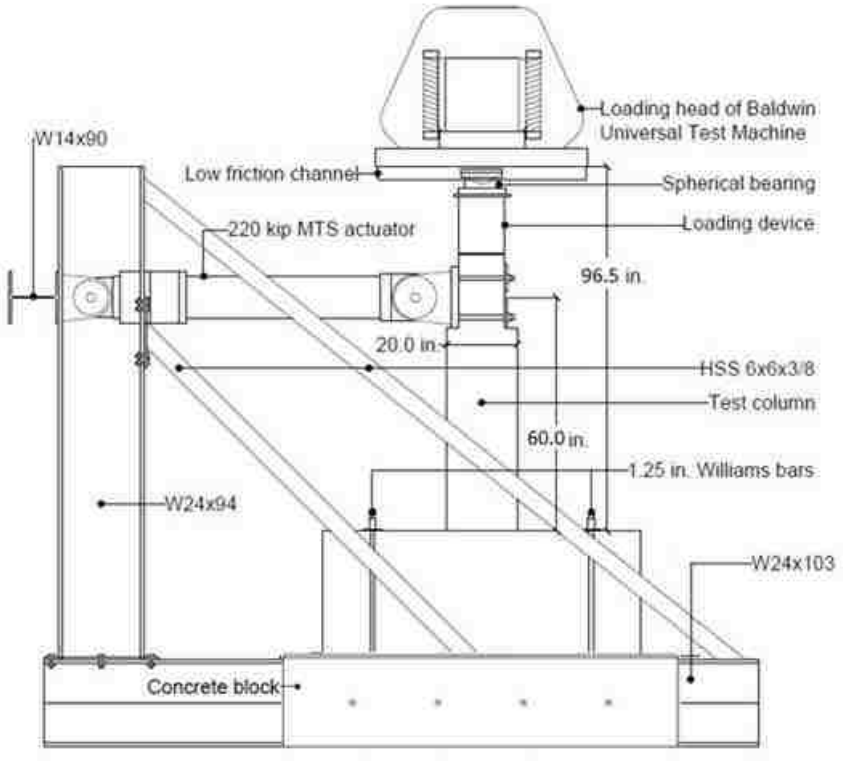

Figure 3.1 Testing rig.

Prior to testing, the specimens were placed on the concrete reaction block. Once centered, researchers poured a high-strength gypsum plaster (Hydro-stone) between the specimen footing and the reaction block so that the entire specimen was in contact with the block. Next, the columns were anchored using four 1.25"-diameter Williams bars stressed to 100 kips each.

Lastly, the columns were painted with white-wash so that cracks would be more visible during testing.

A system was needed to keep the column aligned in the correct vertical plane as it underwent cyclic loading. The system consisted of a steel encasing tube, spherical bearing head, greased PTFE plate and stainless steel channel, arranged in accordance with Figure 3.2. This steel encasing tube was necessary because space was required above the column for the chucks that anchored the prestressing strands and the load cells that detected potential slip. The steel tube had an inside diameter of 12" and wall thickness of 0.5". The square steel plate welded atop the tube had length of 16" and thickness of 7/8". Above the steel plate was a spherical bearing on which rested a greased PTFE pad. When the column rotated during the test, the PTFE plate slid against a stainless steel channel fixed to the head of the Baldwin and the spherical bearing adjusted for the relative rotation.

Figure 3.2 Actual (Left) and Schematic (Right) views for the system that transfers load from the Baldwin to the specimen while safely covering prestressing load cells and chucks.

The MTS actuator was fixed to the reduced section of the column using four 1" diameter threaded rods (Figure 2.1). The rods were stressed to 15 kips each so that the column was firmly fixed to the actuator.

3.2 INSTRUMENTATION

Both specimens were instrumented in the same fashion as outlined in this chapter. For comparison purposes, the instrumentation was kept as similar to that in Finnsson's thesis as possible. Table 3.1 provides the instrumentation manifest used in each column.

Table 3.1 Instrumentation manifest for one column.

Instrument	Measured response	Quantity used
Strand load cell	Detect slip in strands	6
MTS load cell	Horizontal load	1
Baldwin load cell	Axial load	1
Linear potentiometer	Horizontal and vertical movement	13
String potentiometer	Horizontal displacements	6
Linear variable differential transformer (LVDT)	Deflection of testing rig	1
Inclinometer	Rotation	4
3-wire strain gauge	Strain in reinforcement steel	24
2-wire strain gauge	Strain in pre-stressing stands	12

Figure 3.3 details the location of the exterior instruments on the column for all instruments, except for strain gauges.

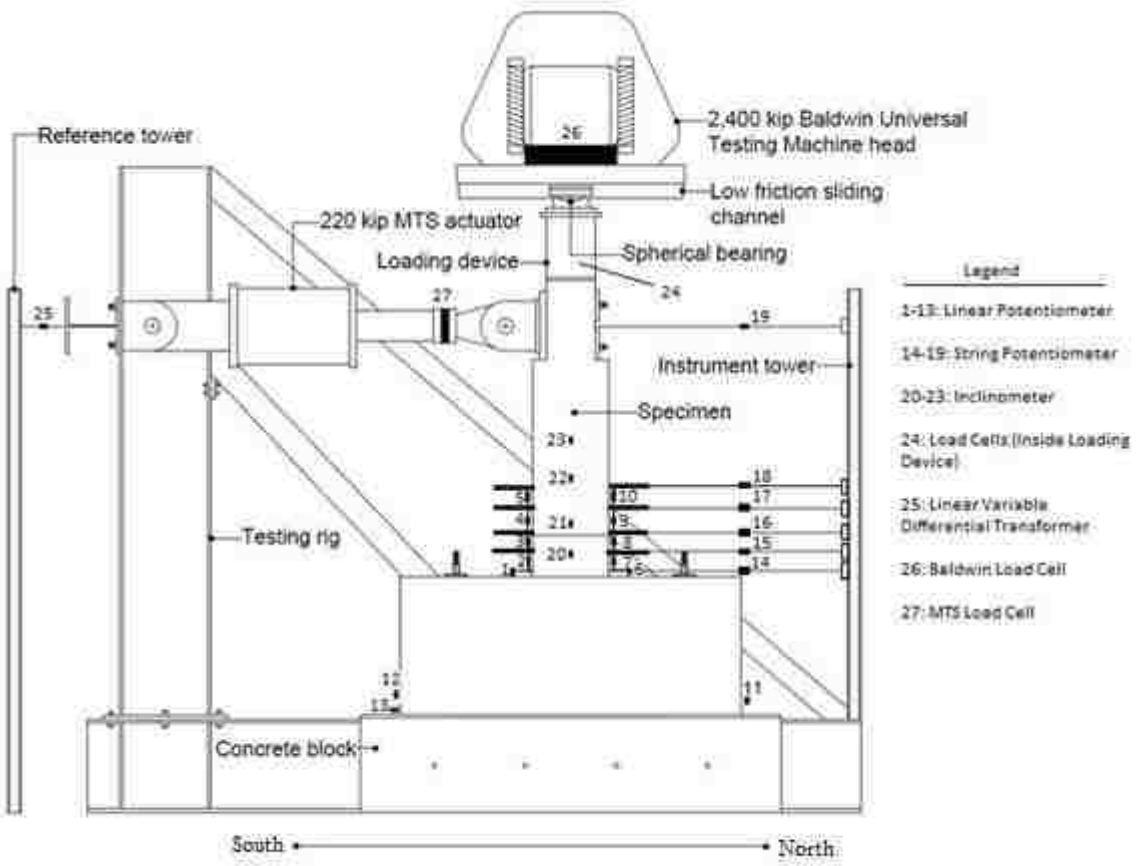

Figure 3.3 Instrumentation setup.

3.2.1 APPLIED LOADS

Internal load cells in both the MTS actuator and Baldwin testing machine measured the respective horizontal and axial loads applied during testing.

3.2.2 STRAIN GAUGES

Two-wire and three-wire strain gauges measured the strains in the longitudinal and transverse reinforcement as well as in the prestressing strands. Three-wire gauges were used as often as possible because they have the ability to compensate the measured readings for temperature effects. As a result, all of the longitudinal and transverse reinforcement strain gauges were 3-wire. Figures 3.4 and 3.5 illustrate the placement of these 3-wire strain gauges. Researchers could not use 3-wire gauges on the prestressing strands because the strand diameter was not wide enough for their insertion. Therefore, the prestressing strands were instrumented with 2-wire gauges.

The strain gauge pattern used was the same as that in Finnsson's specimens with one exception. For this research, the specimens included No. 6 bars welded to the rocking shoe. It was of interest to discover the level of strains those bars experienced under loading. As a result, two pairs of strain gauges, one at the shoe's base and one 7" above the shoe's base, were placed on the Northwest and Southwest bars. These strain gauge locations made it possible to compare these strains with those of the No. 4 bars, which had strain gauges at the column-footing interface, 7" above the interface and 7" below the interface. Two pairs of strain gauges were installed on the transverse reinforcement, one on the north end and one on the south, both 3" above the column-footing interface.

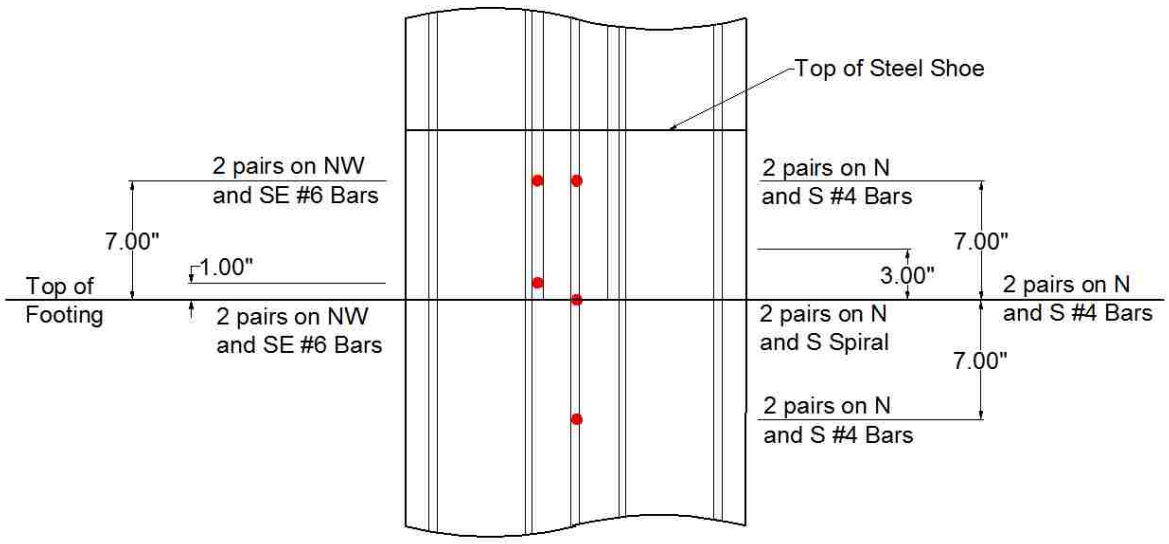

Figure 3.4 Column elevation view of 3-wire strain gauge placements.

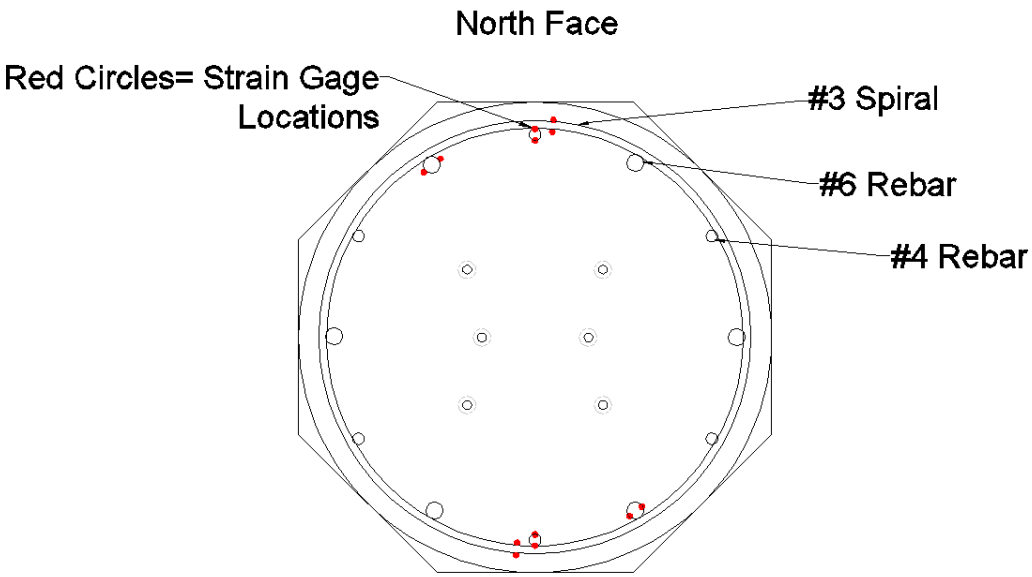

Figure 3.5 Column cross-section view of 3-wire strain gauge placements.

A single pair of 2-wire gauges was placed on each of the six prestressing strands of each column. These strain gauges were located in the strands' unbonded region and not only measured the strain in the strands during the test but also facilitated reaching the target stress during the prestressing operation. The strain across the unbonded region was assumed to be constant.

3.2.3 CURVATURE ROD SYSTEM

The "curvature rod" system depicted in Figure 3.6 was used to measure relative rotations between column cross-sections. As the column rotated, the linear potentiometers measured the change in distance between the threaded rods and, therefore, could be used to compute the relative rotation of each segment. If the column behaved as a rigid body, then the relative rotations would be zero.

The system consisted of a series of linear potentiometers attached to metal plates. These metal plates, in turn, were connected to a set of threaded rods that protruded from the column. The threaded rods were located on both the north and south face at 2.5", 9", 12", 18" and 24.5" above the column-to-footing interface. The lowest linear potentiometer measured the change in height between the footing and the lowest threaded rod.

Figure 3.6 Photograph (Left) and schematic (Right) views of the curvature rod system used on the north face.

At the column-footing interface, the column was predicted to rock as a rigid body. The lowest potentiometer, therefore, was expected to record the largest change in displacement. The next two potentiometers detected the relative column rotation due to any deformation, including cracking, between the concrete confined by the steel shoe and the unconfined concrete immediately above the shoe. Similarly, the highest two potentiometers recorded the relative column rotations at the HyFRC-conventional concrete interface.

3.2.4 MOTION CAPTURE SYSTEM

In both tests, an motion-capture system (Optotrac) measured the three-dimensional motion of targets attached to the column. Figure 3.7 shows the LED configuration on the column. From these measurements, column displacement, rotation and curvature could be calculated. The system consisted of two fixed cameras that monitored a series of LED sensors placed on the column. The arrangement of LED sensors on the column was similar to that in Finnsson's study with one exception. One row each was placed on the north, west and south column faces whereas in Finnsson's study there were three rows on the west face and one row on the north and south faces. Due to a limit on the amount of LEDs available, the additional two rows on the west face were not possible. The LEDs in each row were spaced every 2" for the first 24" above the column-footing interface and 4" after that until a height of 34". The LEDs were concentrated more heavily at the lower region of the column in order to best capture the change in rotation, which was expected to be greatest at the column's base.

Figure 3.7 **Optotrac sensor configuration on the test specimen. On left is a view of north and west sensors. On right is a view of south sensors.**

3.2.5 INCLINOMETERS

Four inclinometers were placed on the east face of the column at 4", 12", 24" and 34" above the column-footing interface. These instruments measured the column's absolute rotation directly. The placement of the inclinometers was the same as that in Finnsson's study. Figure 3.8 shows an inclinometer installed on the column.

Figure 3.8 **Typical inclinometer attached to the column's east face.**

3.2.6 STRAND LOAD CELLS

Six load cells atop each column measured any slip experienced by the prestressing strands (Figure 2.5). No load cells were placed at the bottom of the columns because the strand bond length was longer in the footing than it was at the top of the column. As a result, if the strands slipped in the footing they would also slip at the top of the column. The instruments were seated on the prestressing strands and anchored with a chuck. After release, the strands were reloaded using the method described in Section 2.2 so that each load cell measured approximately five kips. If a load cell registered a reduction in this measured force, then researchers could conclude that the monitored strand had slipped.

3.2.7 HORIZONTAL DEFLECTION OF THE SYSTEM

During the test, six string potentiometers measured the horizontal deflection of the column while one linear potentiometer measured the horizontal translation (slip) of the footing. Figure 3.3 shows the string potentiometer setup. The string potentiometers were clamped to an instrumentation tower and were spaced at the following intervals: 2.5”, 9”, 12”, 18”, 24.5” and 60” above the column-footing interface. Figure 3.9 shows a typical string potentiometer attached to the instrument tower. To ensure that the instrumentation tower did not move during the test, researchers wrench-tightened the tower to the concrete reaction block using Williams Bars. Since the string potentiometers had a finite stroke, piano wire was used to extend the instrument from the tower to the threaded rods.

Figure 3.9 A string potentiometer attached to the instrumentation tower.

The single linear potentiometer was placed on the southeast side of the concrete reaction block on a metal plate. By placing the instrument in this manner, it was out of the way during the test so that researchers would have a lowered chance of stepping on it as they mounted the column for observation. A small metal sheet was also glued to the footing to create an even surface for the instrument to bear against.

In addition, A single linear variable differential transformer (LVDT) measured the distance between the actuator beam and fixed reference tower. From this measurement, researchers could detect any deflection in the actuator beam. Its placement is shown in Figure 3.3.

An LVDT was chosen as opposed to a simple linear potentiometer because the LVDT is more capable of capturing small deflections. Since the flanges of the actuator beam were reinforced with stiffeners, the deflections in the beam were expected to be small; hence, the LVDT seemed an attractive option. Figure 3.10 illustrates the LVDT placement on the actuator beam. Ideally, the combination of the actuator displacement and beam deflection would sum to the displacement of the column measured relative to the reference tower.

3.2.8 ROCKING OF THE FOOTING

Two linear potentiometers, one on the northeast end and one on the southeast end, were placed at the base of the footing facing downwards so that they came into contact with the concrete reaction block. Thin metal sheets were placed underneath the instrument heads so that they rested against a flat surface. The combination of the two potentiometers allowed for detection of any rocking that the footing might experience.

Figure 3.10 The LVDT used to measure the actuator beam deflection during testing.

3.3 TESTING PROTOCOL

During the test, both specimens were subjected to horizontal (lateral) and vertical (axial) loading. The axial load, 159 kips, represented the un-factored dead load of a prototype bridge according to the AASHTO LFRD 2009 Specification scaled down to 42% (AASHTO, 2009). This load was applied first. The lateral displacement history was a modified version of the NEHRP recommendations for precast structural walls and was drift controlled (Building Seismic Safety Council, 2004). This same loading protocol was used by Finnsson et al. (2013), Davis et al. (2011), and Haraldsson et al. (2011).

The lateral displacement history consisted of ten 4-cycle sets. The lateral displacement history is shown numerically in Table 3.2 and graphically in Figure 3.11. Each set had target peak values of 1.2X, 1.44X, 1.44X and 0.48X, where X is the maximum target drift from the previous set. Researchers manually selected the maximum target drift of the first set so that the column would remain elastic throughout the duration of the first four cycles. The last cycle in every set was purposely reduced in order to obtain the column's residual stiffness after greater loading.

During the test, the lateral load was applied in the North-South direction. In each cycle, the actuator first pulled the column to the South and then pushed the column to the North before finally returning the column to its initial position. As a result, this thesis refers to loading in the South as positive and loading in the North as negative. Additionally, this thesis refers to maximum loading in the southern direction as the peak and maximum loading in the northern direction as the valley. In each set, the column was loaded both continuously and intermittently. During the first two cycles, researchers held the lateral load at both the peaks and valleys so that they could mark cracks and document the column's damage progression. During the third and fourth cycles, the loading was applied continuously without stopping at the peaks or valleys.

Additionally, the load rate was kept as constant as possible. To achieve this, the earlier sets, having lower maximum target drifts, reached their maximum displacement in a shorter interval than the later sets. For example, the actuator reached the maximum displacement in twenty seconds during sets one through six, thirty seconds during sets seven through nine, and sixty seconds during set ten.

The day before the test, researchers conducted a test cycle to verify that all of the instruments were operating properly. In this test cycle, the axial load applied was reduced to 90 kips and the target drift was only 0.05%. The reduced loading ensured that the column suffered no damage prior to the actual test yet the instruments were engaged sufficiently enough to verify that they were working.

Table 3.2 Target displacement history.

Set	Cycle	Drift [%]	Displacement [in.]
1	1	± 0.33	± 0.20
	2	± 0.40	± 0.24
	3	± 0.40	± 0.24
	4	± 0.13	± 0.08
2	1	± 0.48	± 0.29
	2	± 0.58	± 0.35
	3	± 0.58	± 0.35
	4	± 0.19	± 0.11
3	1	± 0.69	± 0.41
	2	± 0.83	± 0.50
	3	± 0.83	± 0.50
	4	± 0.28	± 0.17
4	1	± 1.00	± 0.60
	2	± 1.19	± 0.71
	3	± 1.19	± 0.71
	4	± 0.40	± 0.24
5	1	± 1.43	± 0.86
	2	± 1.72	± 1.03
	3	± 1.72	± 1.03
	4	± 0.57	± 0.34
6	1	± 2.06	± 1.24
	2	± 2.48	± 1.49
	3	± 2.48	± 1.49
	4	± 0.83	± 0.50
7	1	± 2.97	± 1.78
	2	± 3.57	± 2.14
	3	± 3.57	± 2.14
	4	± 1.19	± 0.71
8	1	± 4.28	± 2.57
	2	± 5.14	± 3.08
	3	± 5.14	± 3.08
	4	± 1.71	± 1.03
9	1	± 6.16	± 3.70
	2	± 7.40	± 4.44
	3	± 7.40	± 4.44
	4	± 2.47	± 1.48
10	1	± 8.87	± 5.32
	2	± 10.65	± 6.39
	3	± 10.65	± 6.39
	4	± 3.55	± 2.13

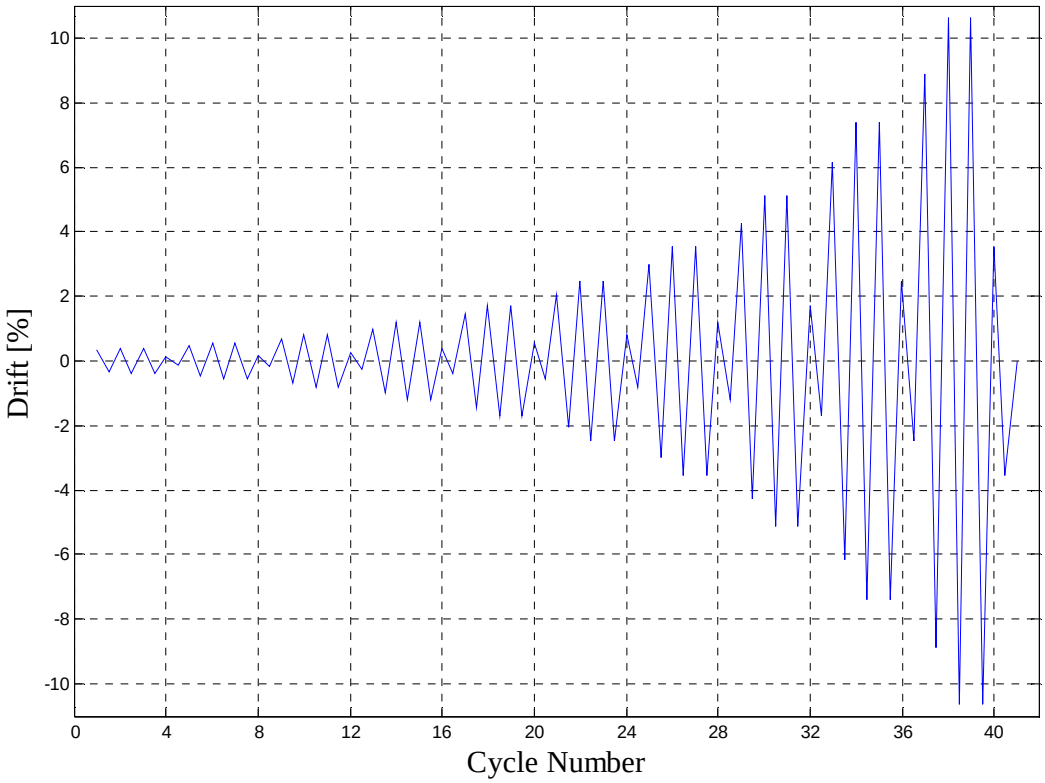

Figure 3.11 Graphical representation of the target displacement history.

4 Observed Damage Progression

During both tests, researchers documented the columns' damage progression by taking photographs, marking crack formation and propagation, and measuring crack widths. One goal of this design was to reduce the amount of damage done to the column. This chapter analyzes how proficiently the columns met this design goal. This chapter contains selected images of the columns in a damaged state; the majority of damage progression photos are located in Appendix C.

4.1 DAMAGE STATES DEFINITIONS

In each test, researchers monitored the columns closely to identify key damage states defined by the UW/PEER Structural Performance Database (Barry and Eberhard 2004). Previous experiments at the University of Washington used the same damage state milestones making it easier to compare damage observations in this thesis with those in previous studies. Table 4.1 outlines the used damage states.

Table 4.1 Damage states used to characterize damage progression in the columns.

Damage state	Description/observation
First significant horizontal crack	Crack width ≥ 0.5 mm
First significant diagonal crack	Crack width ≥ 0.5 mm and crack extends 1/4 of column diameter
First open residual crack	Residual crack width ≥ 0.25 mm
First yield of longitudinal rebar	First strain gauge that reaches yield strain
First yield of transverse reinforcement	First strain gauge that reached yield strain
First spalling in footing	Observed spalling on surface
First spalling in column	Observed flaking, minor spalling
Significant spalling in column	Spalled height ≥ 1/4 of column diameter
Fully spalled	Spalling height no longer increases with increasing deformation
Exposure of longitudinal reinforcement	First observation of column longitudinal reinforcement
Buckling of longitudinal reinforcement	First observation of buckling of longitudinal reinforcement bars
Large cracks in concrete core	Crack width ≥ 2.0 mm
Fracture of transverse reinforcement	Observation or sound
Fracture of longitudinal reinforcement	Observation or sound
Loss of axial capacity	Instability of member (column)

4.2 DAMAGE PROGRESSION

The day prior to each test, researchers applied a small loading cycle (0.05% drift) to the instrumented column as previously described in Section 3.3. The small loading cycle allowed the researchers to confirm that all instruments were working properly. The deformation was not large enough to cause any visible cracking in the column.

In the actual test, researchers recorded the set and cycle number as well as the drift ratio at which each of the aforementioned damage states occurred. The only damage states that were not visibly apparent were first yield of longitudinal rebar and first yield of transverse reinforcement. These damage states were determined later from the strain gauge measurements in. Table 4.2 summarizes these results. Items listed as N/A indicate a damage state that was never observed. As can be seen, most of the states associated with concrete damage never occurred.

Figure 4.1 graphically compares the drift levels at which each column reached key damage states. Furthermore, Figure 4.2 graphically compares the damage progression of the columns in this thesis with those of Finnsson et al (2013), PreT-SF-HyFRC, and Davis et al (2011), PreT-SF-CONC. This comparison illustrates that the rocking columns in this thesis

suffered much less cracking and spalling than their predecessors. Damage states that never occurred are left blank in these plots.

Table 4.2 Summary of damage state progression for both specimens.

Damage state	PreT-SF-ROCK-HyFRC			PreT-SF-ROCK		
	Set	Cycle	Drift [%]	Set	Cycle	Drift [%]
First significant horizontal crack	n/a	n/a	n/a	n/a	n/a	n/a
First significant diagonal crack	n/a	n/a	n/a	n/a	n/a	n/a
First open residual crack	n/a	n/a	n/a	n/a	n/a	n/a
First yield of longitudinal rebar	2	2	0.41/-0.35	1	2	0.26/-0.30
First yield of transverse reinforcement	n/a	n/a	n/a	n/a	n/a	n/a
First spalling in footing	n/a	n/a	n/a	n/a	n/a	n/a
First spalling in column	n/a	n/a	n/a	8	4	1.58/-1.54
Significant spalling in column	n/a	n/a	n/a	8	4	1.58/-1.54
Fully spalled	n/a	n/a	n/a	n/a	n/a	n/a
Exposure of longitudinal reinforcement	6	2	2.25/-2.30	6	1	1.86/-1.84
Buckling of longitudinal reinforcement	n/a	n/a	n/a	n/a	n/a	n/a
Large cracks in concrete core	n/a	n/a	n/a	n/a	n/a	n/a
Fracture of transverse reinforcement	n/a	n/a	n/a	n/a	n/a	n/a
Fracture of longitudinal reinforcement	9	1	5.96/-5.83	9	1	5.94/-5.76
Loss of axial capacity	n/a	n/a	n/a	n/a	n/a	n/a

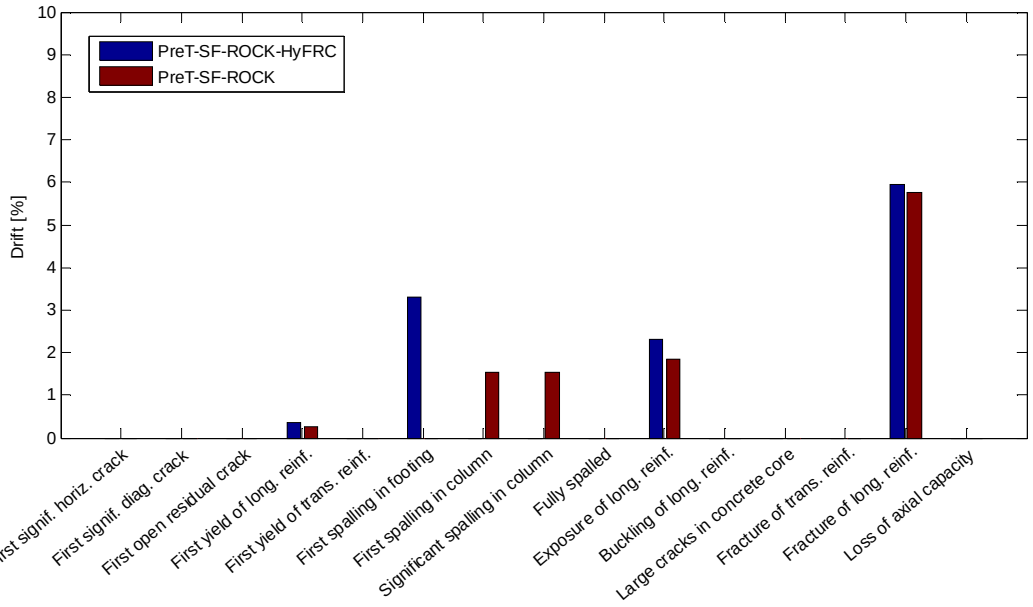

Figure 4.1 **Comparison of drift levels at which both columns reached the defined damage states.**

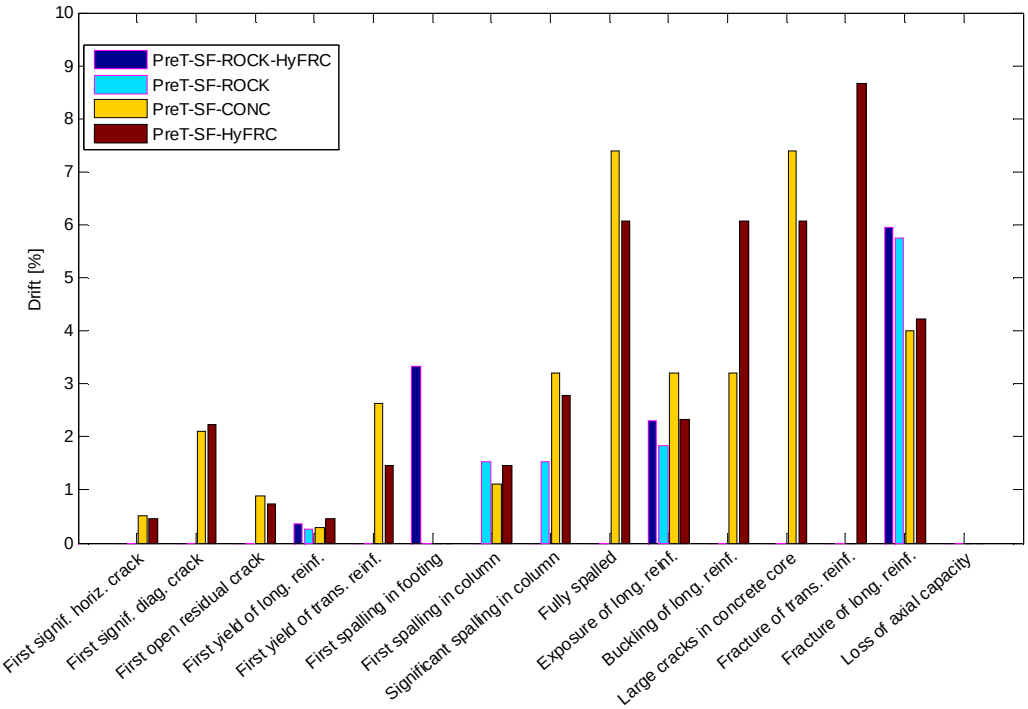

Figure 4.2 Comparison of damage states vs. drift levels occurred between the specimens in this thesis and those of Finnsson et al (2013).

4.2.1 Concrete Cracking

Both columns experienced very little cracking, even at high drift levels. As the columns were loaded horizontally, they rocked on the bottom plate of the steel shoe as opposed to developing a plastic hinge in the concrete region above the steel shoe. Throughout the test, neither column developed cracks in the concrete that exceeded a hairline width. Researchers did not treat the separation of the footing concrete with the bottom face of the steel shoe as a conventional crack, so this separation was not considered in determining the drift ratio at which the damage states were reached. Figure 4.3 and Figure 4.4 illustrate the limited amount of cracking observed in both PreT-SF-ROCK-HyFRC and PreT-SF-ROCK at a drift ratio of 6.0% drift. In these images, blue lines drawn on the column indicate the formed cracks. Both columns had little cracking. The HyFRC in PreT-SF-ROCK-HyFRC appeared to reduce the amount of hairline cracking as compared with its solely conventional concrete column counterpart.

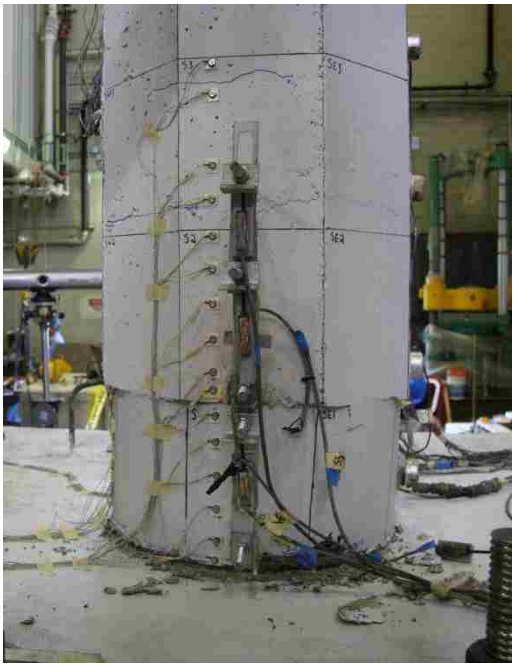

Figure 4.3 South view of PreT-SF-ROCK-HyFRC after cycle 9-1 (6% max drift) showing hairline cracking in the column.

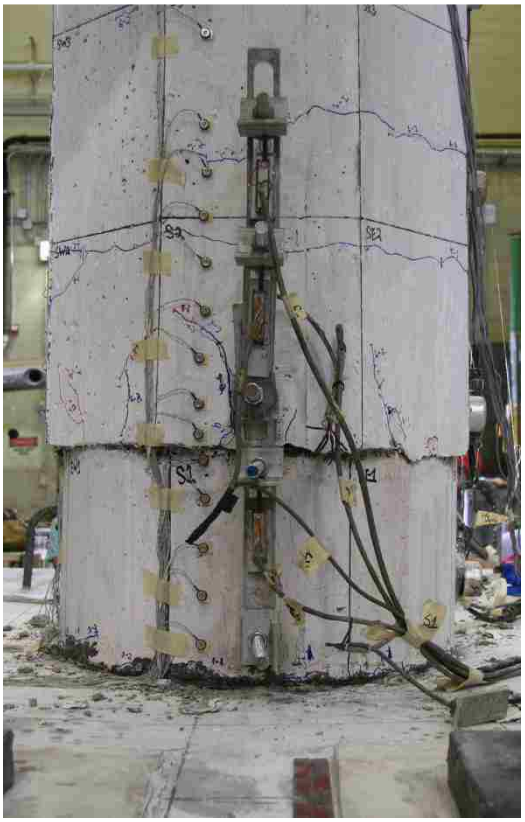

Figure 4.4 South view of PreT-SF-ROCK after cycle 9-1 (6% max drift) showing hairline cracking in the column.

4.2.2 Initial Yielding

Strain gauges on the longitudinal and transverse reinforcement allowed researchers to determine the point at which those bars first yielded. The longitudinal reinforcement in PreT-SF-ROCK-HyFRC first yielded at -0.35% drift, whereas the longitudinal reinforcement in PreT-SF-ROCK first yielded at 0.26% drift. The drifts at initial yield observed in this thesis were lower than those reported by Finnsson et al. (2013) and the same levels as those in Davis et al. (2011), which experienced initial yielding at 0.54% and -0.28% drift respectively.

As expected, initial first yield occurred at the column-footing interface where the moment was highest. The longitudinal reinforcement was unbonded 8" with PVC sleeves, 4" above and 4" below interface. This debonded region distributed the bar elongation over an extended length, reducing the strain for a given drift. Considering the drift level at first yield, researchers concluded that the 8" debonded region is essential. Table 4.3 shows the extent to which the initial yield in this thesis compares to that of previous experiments.

Table 4.3 Comparison of drift levels at initial yield

	Drift at Initial Yield	Percent change from PreT-SF-HyFRC (Finnsson et al 2013)	Percent change from PreT-SF-CONC (Davis et al 2011)
PreT-SF-ROCK-HyFRC	-0.35%	-35%	25%
PreT-SF-ROCK	0.26%	-52%	-7.1%

In both columns, the transverse reinforcement remained elastic throughout the duration of the test. The absence of yielding was likely attributable to the heavy confinement provided by the footing and the steel shoe. The concrete in both these regions was so heavily confined that the transverse reinforcement engaged only to a limited extent.

4.2.3 Concrete Spalling

The columns described in this thesis underwent significantly less spalling than those in previous experiments. In fact, PreT-SF-ROCK-HyFRC experienced no spalling in the column while PreT-SF-ROCK arguably experienced only architectural spalling. Spalling did not occur in PreT-SF-ROCK until after a drift ratio of 5.1% (Cycle 8-4) of the test. The spalling was located on the south face immediately above the top of the steel shoe. Figure 4.5 depicts this architectural spalling in PreT-SF-ROCK.

There are two reasons why one could dismiss this spalling as architectural damage as opposed to structural damage. First, the cross-section of the column in the steel shoe region is circular whereas it is octagonal immediately above. This change in geometry causes the interface between the steel shoe and concrete above to be imperfect. The concrete above the steel shoe protrudes over the steel edge much like a cantilever. This makes it highly prone to breaking off under loading because at the cantilever edge the concrete must have zero stress whereas a short

distance higher the concrete will experience compressive stress. The inverted V-shaped cracks at the top of the steel shoe shown in Figure 4.4 reflect the shear stresses that must act between these two locations. These cracks resulted in the observed spalling. They could be eliminated in the future with the use of a tapered finish, if desired. Once the cantilevered portion of concrete spalled away, the spalling ceased to progress. Secondly, the spalling initiated at an insert of a curvature rod, an instrument that would not be present in the column in practice. The curvature rod, which was cast into the column, creates a discontinuity in the concrete, making this location more susceptible to spalling.

The higher tensile strength of HyFRC prevented this architectural spalling from occurring in PreT-SF-ROCK-HyFRC.

Figure 4.5 South view of PreT-SF-ROCK after cycle 8-4 showing spalling damage above the steel shoe.

Minor spalling also occurred in the footing concrete immediately surrounding the steel shoe. Despite the laborers best efforts, concrete rose roughly half an inch above of the steel shoe during the footing casting. This created a fillet at the base of the shoe, which was prone to spalling when the steel shoe underwent rocking action during loading. Researchers observed this spalling in both PreT-SF-ROCK and PreT-SF-ROCK-HyFRC. Figures 4.6 and 4.7 depict this occurrence. In both specimens, the spalling ceased to extend once the fillet portion of concrete spalled off leaving a flush surface. This behavior was purely cosmetic and had no effect on the columns' structural response.

As expected, no conventional spalling was observed in the footing. This observation was consistent with previous tests by Finnsson et al. (2013), Davis et al. (2011) and Haraldsson et al.

(2011), in which no footing spalling occurred either. The footings were capacity-designed, forcing all damage to occur in the columns.

Figure 4.6 **South view of PreT-SF-ROCK showing the fillet spalling of the footing induced by the rocking action of the steel shoe.**

Figure 4.7 **South view of PreT-SF-ROCK-HyFRC showing the fillet spalling of the footing induced by the rocking action of the steel shoe.**

Crushing also occurred in the concrete beneath the steel shoe as it rocked about its base. The rubble created by the rocking prevented the column from closing perfectly when it returned to its initial position. Researchers witnessed this behavior only in specimen PreT-SF-ROCK-HyFRC. In specimen PreT-SF-ROCK, the interface between the bottom of the shoe and the top of the footing portion of the column was very smooth. The likely cause of this difference stems from the method used to pour the HyFRC. During casting, a steel-wire mesh was placed to prevent the HyFRC from flowing into the footing portion of the column. However, the steel mesh was not

perfectly rigid or impermeable. As a result, a small amount of HyFRC seeped underneath the bottom of the steel shoe, forming a jagged surface. During the test, this portion of HyFRC was crushed between the base of the steel shoe above and the conventional concrete beneath it. After both tests were complete, researchers detached the column from the footing in specimen PreT-SF-ROCK-HyFRC for closer observation of the column-footing interface (Figure 4.8).

Figure 4.8 **Jagged portion of HyFRC that seeped through steel-wire mesh (Left). Column-footing interface after top portion of column was removed (Right).**

4.2.4 Damage to Longitudinal Reinforcement

Table 4.1 (Section 4.2.2) outlines three damage states pertaining to the longitudinal reinforcement other than yielding: exposure, buckling and fracture. Both reinforcement exposure and fracture occurred at later cycles in the test, whereas reinforcement buckling was not observed at all. Longitudinal reinforcement exposure happened first in cycles 6-1 (PreT-SF-ROCK) and 6-2 (PreT-SF-ROCK-HyFRC). Due to the nature of the rocking column, the reinforcement became completely exposed without any action on behalf of the researchers whereas in previous tests, complete exposure of the reinforcement only happened after researchers pulled away spalled portions of the column. In fact, not only did the longitudinal rebar become fully exposed but also the prestressing strands were also visible, an observation that did not happen in previous tests. Researchers originally conceived this particular damage state as a measure of how much concrete area was lost; however, in these two tests, the bars became visible through a different mechanism, rendering this damage state irrelevant.

The longitudinal reinforcement fractured at drift ratio of approximately 6.0% (Cycle 9-1) in both PreT-SF-ROCK-HyFRC and PreT-SF-ROCK. The fracture is depicted in Figures 4.9-4.11. This drift level at fracture was only slightly lower than the drift level observed in Finnsson's PreT-SF-HyFRC-SS column, which fractured at 7.2% drift. The fact that the difference is small was not surprising, because Finnsson's PreT-SF-HyFRC-SS column contained stainless steel, which is more ductile than the conventional "black steel" used in both PreT-SF-ROCK and PreT-SF-ROCK-HyFRC. Finnsson's PreT-SF-HyFRC column, which also contained black steel, fractured at a drift ratio of 4.1%, indicating that the rocking behavior of the steel shoe paired with the 8" debonding of the longitudinal reinforcement provided added

ductility to the columns in this thesis. Table 4.4 shows the extent to which bar fracture in this thesis compares to that of two previous experiments.

Table 4.4 Comparison of drift levels at bar fracture

	Drift at Bar Fracture	Percent increase from PreT-SF-HyFRC (Finnsson et al 2013)	Percent increase from PreT-SF-CONC (Davis et al 2011)
PreT-SF-ROCK-HyFRC	5.96%	31%	33%
PreT-SF-ROCK	5.94%	30%	33%

One unexpected occurrence was the fracture of prestressing strands in specimen PreT-SF-ROCK-HyFRC. During testing, specimen PreT-SF-ROCK-HyFRC lost three of its prestressing strands while specimen PreT-SF-ROCK lost none. Researchers visibly observed the first fractured strand in Cycle 10-1 (Figure 4.12); however, the strand may have fractured as early as Cycle 9-2 when researchers heard a loud noise. The noise was likely caused by the fracture of a prestressing strand as opposed to a longitudinal rebar, because the noise appeared to come from the top of the column. Additionally, the load cell attached to the southeast strand lost all load at 7.27% drift which is roughly the drift level associated with Cycle 9-2. The dowel bar placed at the column-footing interface may have caused this strand fracture as it was one of only two differing factors between specimens PreT-SF-ROCK-HyFRC and PreT-SF-ROCK. As the column rotated, the cup feature in the footing allowed the dowel bar to rotate while the strands resisted rotation. Furthermore, only the east facing strands fractured. It is possible that a misaligned dowel bar pressed against the east strands, causing them to kink and subsequently fracture.

Researchers did not observe any buckling in the longitudinal reinforcement in either test although the steel shoe largely concealed the longitudinal reinforcement for the majority of the test making observation of buckling difficult. However, if the longitudinal reinforcement did buckle, it would likely have failed shortly thereafter. In both tests, the longitudinal reinforcement did not fracture until approximately 6% drift. This high drift level indicates that the reinforcement roughly reached its maximum tensile capacity, supporting the observation that the reinforcement did not buckle.

In earlier tests (Finnsson et al. 2013, Davis et al. 2011 and Haraldsson et al. 2011), the base of the column was not confined externally by a steel shoe. As the cover spalled, the bars lost lateral support and consequently buckled. Conversely, no bars ever buckled in the footing due to the large quantity of concrete that provided significant lateral support. Thus, the steel shoe appears to offer an effective means of lateral support that consequently prevented bar buckling.

Figure 4.9 **Exposed north bar of PreT-SF-ROCK.**

Figure 4.10 **Fractured northwest bar of PreT-SF-ROCK-HyFRC (fractured in footing).**

Figure 4.11 Fractured north bar of PreT-SF-ROCK.

Figure 4.12 Northwest view of PreT-SF-ROCK-HyFRC showing location of missing strand (fractured).

4.2.5 Loss of Axial-Load Capacity

Neither column ever lost its axial capacity. This was expected because, in previous tests by Finnsson et al. (2013), Davis et al. (2011) and Haraldsson et al. (2011), the axial capacity was never lost either. In fact, Haraldsson showed that the true axial capacity of the columns

significantly greatly exceeded their factored design load. After completing the 40 cycles of lateral loading, Haraldsson increased the applied axial load until failure. At that time, the longitudinal bars had buckled, the spiral had fractured, and the concrete core was partially crushed. Nonetheless, the columns did not explode until the applied axial load was three and a half times the factored design load. This result should not be surprising considering the design axial load for a bridge column is typically in the range of $0.03f'_cA_g$ to $0.10f'_cA_g$.

5 Measured Response

5.1 MATERIAL PROPERTIES

Researchers constructed the columns and footings in the Structural Engineering Laboratory at the University of Washington. The casting and curing of both the columns and footings also took place in the university's structures lab. A local ready mix company (CalPortland) provided the conventional concrete, whereas researchers mixed the HyFRC themselves using the lab's facilities. Concrete cylinders were taken from each batch of concrete, using 4 in. by 8 in. cylinders for the HyFRC and 6 in. by 12 in. cylinders for the conventional concrete. Researchers stored the cylinders in a fog room at the University of Washington where they kept the relative humidity at 100% and the temperature at 70°F. For both specimens, researchers performed material tests on the conventional concrete and HyFRC, as well as on the longitudinal and transverse reinforcement.

5.1.1 Conventional Concrete

To build the two specimens, researchers used only two batches of conventional concrete, one for both columns and another for both footings. The cylinders of each batch were tested at 7 days, 14 days, 28 days and on both specimen test days. The cylinders were also tested on the day that the prestressing strands were released. Table 5.1 lists the compressive strengths of the concrete batches on the two specimen test days; Appendix A gives the batches' complete compressive strength histories. The measured column concrete compressive strength decreased by 3.7% as it aged from 79 days to 90 days. This decrease is likely attributable to random variations among the strengths of individual cylinders.

Table 5.1 Conventional concrete compressive strengths on test days

Specimen	Column		Footing	
	Compressive Strength [psi]	Age [days]	Compressive Strength [psi]	Age [days]
PreT-SF-ROCK	10,273	79	9022	35
PreT-SF-ROCK-HyFRC	9894	90	9326	46

Modulus of elasticity tests were also performed for both the column and footing concrete at 28 days and the two specimen test days. An additional column concrete test was done on the day of release. Table 5.2 lists the measured modulus of elasticity for the concrete batches on the two specimen test days; Appendix A documents the variation in modulus of elasticity over time.

Table 5.2 Conventional concrete elastic modulus on test days

Specimen	Elastic Modulus [ksi]	Age [days]
PreT-SF-ROCK	3747	79
PreT-SF-ROCK-HyFRC	3881	90

Split-cylinder tests were performed to measure the concretes' tensile strengths on the day Specimen PreT-SF-ROCK-HyFRC was tested. Researchers would have gathered more data points for this strength parameter, but the number of concrete cylinders available limited this ability. The PreT-SF-ROCK-HyFRC test day was deemed the most important date to measure this parameter, because PreT-SF-ROCK-HyFRC contained HyFRC, and a major difference between HyFRC and conventional concrete is their difference in tensile strengths. The tensile strength was computed as:

$$f_{ct} = \frac{2P}{\pi l d} \tag{5.1}$$

where P is the maximum load applied in the test, l is the length of the specimen (12 in. for 6x12 in. cylinders) and d the diameter of the specimen (6 in. for 6x12 in. cylinders). Table 5.3 lists the measured tensile strengths for both the column and footing concretes on the PreT-SF-ROCK-HyFRC test day.

Table 5.3 Conventional concrete tensile strength on PreT-SF-ROCK-HyFRC test day

Column			Footing		
Age [days]	Tensile Strength [psi]	Tensile Strength/f'_c	Age [days]	Tensile Strength [psi]	Tensile Strength/f'_c
90	673	6.8%	46	646	6.9%

5.1.2 HyFRC

The HyFRC were mixed in four equal-sized batches. Researchers then combined and vibrated the batches together to achieve uniformity. The same process was followed to make the HyFRC for the cylinders. Researchers conducted compressive strengths on the HyFRC cylinders at 7 days, 14 days, 28 days, release and the PreT-SF-ROCK-HyFRC test day. No tests were done on PreT-SF-ROCK test day, because that specimen did not contain any HyFRC. Additionally, researchers tested the elastic modulus of the HyFRC at 28 days and the PreT-SF-ROCK-HyFRC test day. Lastly, split-cylinder tests were done on PreT-SF-ROCK-HyFRC test day. Table 5.4 shows the HyFRC material properties at PreT-SF-ROCK-HyFRC test day while the Appendix A lists the complete strength progression of the HyFRC.

Table 5.4 HyFRC material properties on PreT-SF-ROCK-HyFRC test day

Specimen	Age [days]	Compressive Strength [psi]	Elastic Modulus [ksi]	Tensile Strength [psi]	Tensile Strength/f'_c
PreT-SF-ROCK-HyFRC	92	10,203	4496	1452	14.2%

5.1.3 Steel Reinforcement

Both columns had four types of steel reinforcement: 3-gauge smooth wire spiral, No. 4 and No. 6 deformed reinforcing bars, and the welded steel shoe. Researchers conducted tension tests on two samples of each the No. 4 and No. 6 bar sizes. Table 5.5 lists the key properties of the reinforcing steel used in the two columns.

The 3-gauge smooth wire used was from the same batch used by Finnsson et al. (2013). As a result, this thesis repeats the tension results obtained by Finnsson. Prior to this material test, Finnsson had to straighten the wire since it was supplied in coils. This measure induced reverse plastic bending and likely caused the absence of a yield plateau in the resulting stress-strain curve. Researchers did not conduct any tests on the welded steel shoe. Researchers did not test any samples of the footing steel either because previous tests on similar footings had shown that the footing steel did not yield. Appendix A documents the full stress-strain curves.

Table 5.5 Measured properties of reinforcing steel

Type	Yield Stress f_y [ksi]	Tensile Strength f_u [ksi]	Elastic Modulus E-mod [ksi]
#4	67.5	89.9	29100
#6	67.0	89.6	26300
3-gauge spiral	86.3	96.0	30500

5.2 MOMENT-DRIFT RESPONSE

The moment at the base of the each column, including P-delta effects, was calculated using Equation 5.2

$$M = H \cdot h_1 + P \cdot \frac{h_2}{h_1} \cdot \Delta_1 - F \cdot \Delta_2 \quad (5.2)$$

where M is the base moment, H is the lateral load applied by the MTS Actuator, h_1 is the distance from the column-footing interface to the center of the MTS actuator (60”), P is the axial load applied by the Baldwin, h_2 is the distance from the column-footing interface to the spherical bearing (96.5”), Δ_1 is the measured lateral displacement of the column at elevation h_1, F is the estimated friction force between the stainless steel sheet and the greased PTFE pad, and Δ_2 is the lateral displacement at h_2 estimated as $(h_2/h_1) \cdot \Delta_1$. Figure 5.1 graphically depicts these variables in reference to the test setup.

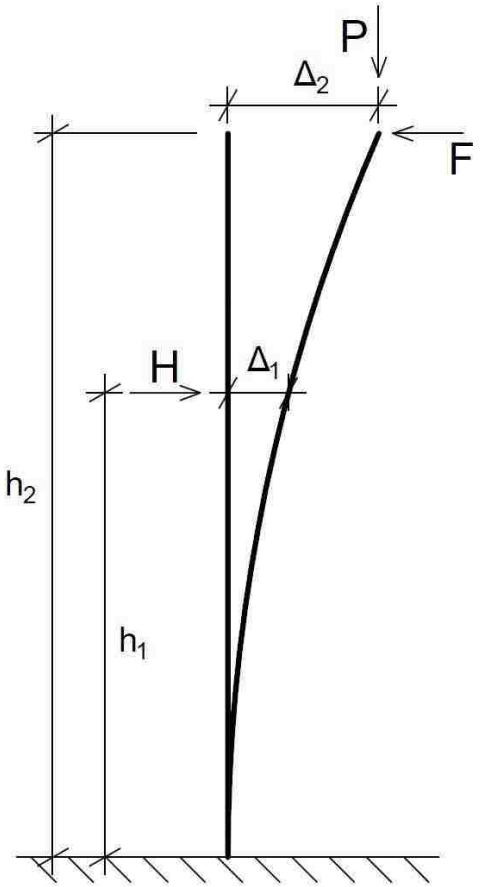

Figure 5.1 Definitions of variables for Equation 5.2.

Although researchers greased the PTFE pad and stainless steel sheet to minimize resistance, the two components nonetheless generated a small friction force as they slipped against each other throughout the test. The friction force (F) was calculated using the model developed by Brown et al. (2008), illustrated in Figure 5.2.

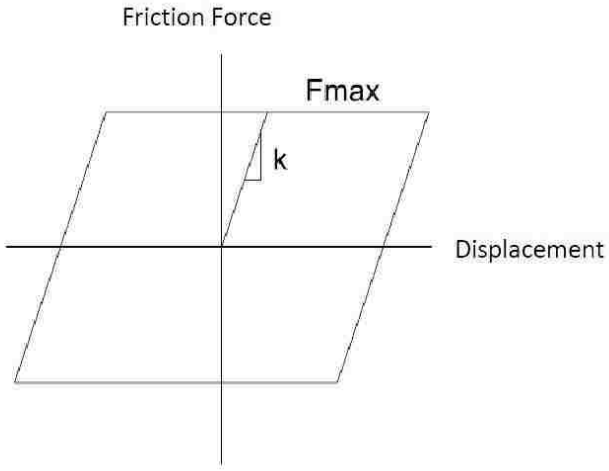

Figure 5.2 Friction correction model, Brown et al. (2008).

The approximated friction had two components: one derived from the sliding in the channel and the other derived from the rotation of the spherical bearing. The effective coefficient of friction was determined using Equation 5.3:

$$\mu_{eff} = \mu_{flat} + \mu_{curv}\frac{R}{L_{total}} \tag{5.3}$$

In this model, μ_{flat} represents the sliding within the channel, whereas μ_{curv} represents the rotation of the spherical bearing. R is the radius of the spherical bearing. and L_{total} is the total height from the top of the footing to the top of the spherical bearing. The maximum friction force was calculated as $\mu_{eff} \cdot P$ where P is the applied axial load (159 kips). Brown et al. (2008) determined μ_{eff} to be 1.6%, resulting in a maximum friction force of 2.54 kips or 4.2% of the maximum expected lateral load from the MTS Actuator. Figure 5.3 illustrates the friction coefficients associated with the sliding channel.

Figure 5.3 Schematic drawing of the sliding channel and its friction components.

Researchers used a spring stiffness, k, of 5 kips/in when correcting the moment and effective force plots for friction. This value is different from the 60 kips/in. Brown used in his study; however, both previous tests, Finnsson et al. (2013) and Davis et al. (2011), discovered that a spring stiffness of 60 kips/in. is too stiff and causes unlikely force-deformation relationships. Figures 5.4 and 5.5 depict the uncorrected moment-drift responses, whereas figures 5.6 and 5.7 depict the corrected moment-drift responses of PreT-SF-ROCK-HyFRC and PreT-SF-ROCK respectively.

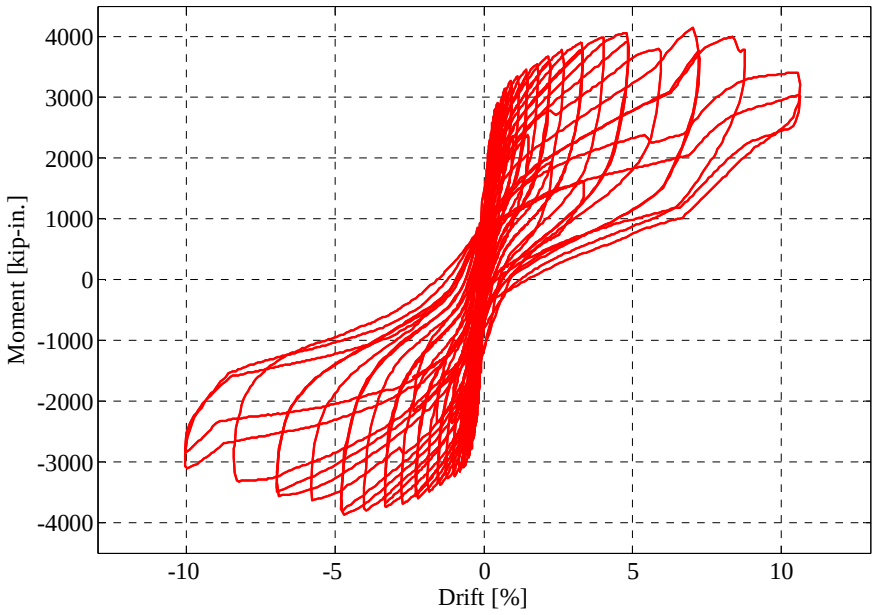

Figure 5.4 Uncorrected moment-drift plot for Specimen PreT-SF-ROCK-HyFRC.

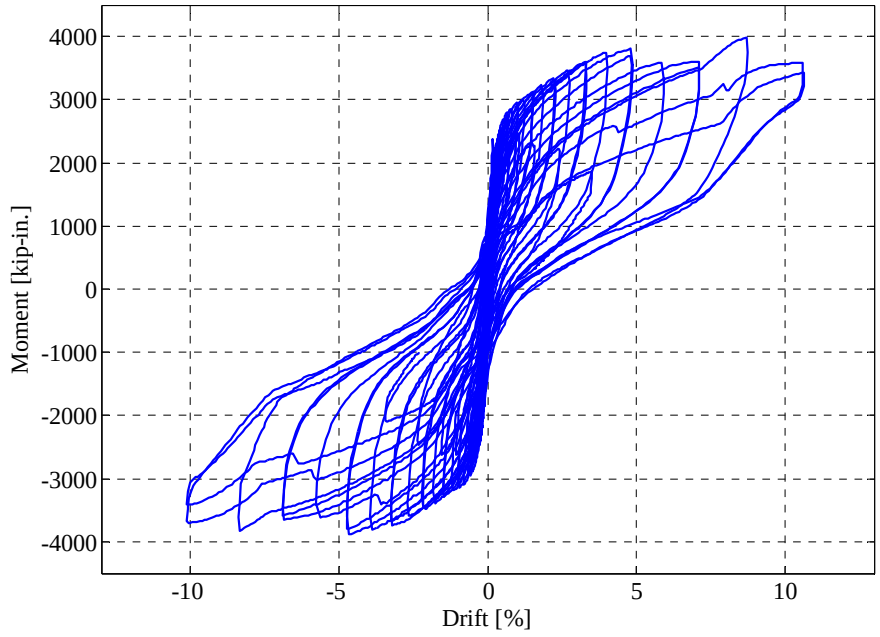

Figure 5.5 Uncorrected moment-drift plot for Specimen PreT-SF-ROCK.

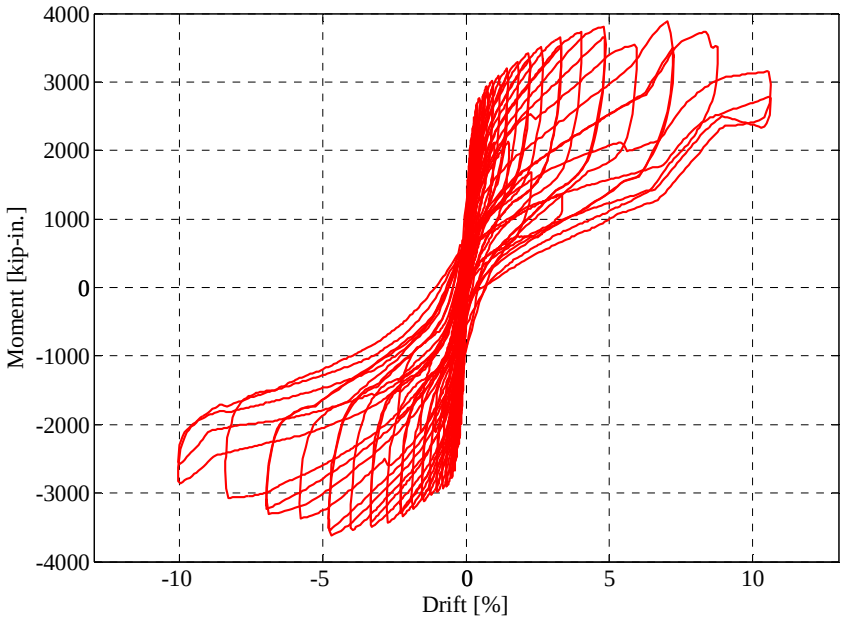

Figure 5.6 Corrected moment-drift plot for Specimen PreT-SF-ROCK-HyFRC.

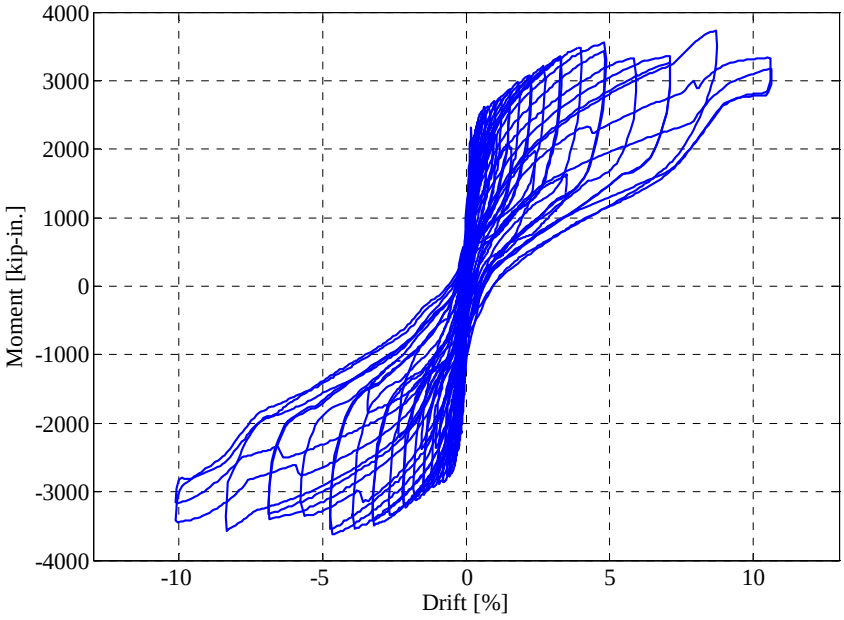

Figure 5.7 Corrected moment-drift plot for Specimen PreT-SF-ROCK.

The main differences between the uncorrected and corrected moment-drift plots are a slight reduction in maximum moment and an increase in the amount of pinching of the hysteresis loops. The overall shape of the two plots, however, is the same. Force and moment data presented in the rest of this thesis correspond to friction-corrected values. Table 5.6 summarizes the maximum corrected moments and the corresponding drift levels.

The moment-drift responses of the two specimens were similar to each other. The flexural strength of PreT-SF-ROCK-HyFRC was only 4% higher than that of PreT-SF-ROCK. Additionally, both specimens continued to gain strength even after the first bar fractured at approximately 6% drift (Table 4.2). The maximum moment in PreT-SF-ROCK-HyFRC and PreT-SF-ROCK did not occur until 6.8% drift and 8.5% drift respectively.

Another measure of performance is strength degradation. One common definition of "failure" is the point at which moment resistance decreases to 80% of its maximum value. Similar to the specimens in Finnsson et al. (2013), PreT-SF-ROCK-HyFRC and PreT-SF-ROCK maintained this level of moment resistance to drift levels beyond 10% with the exception of PreT-SF-ROCK-HyFRC in the north direction. This observation suggests that the inclusion of HyFRC in the rocking shoe column is not needed to obtain highly ductile behavior.

Table 5.6 Summary of moment-drift response.

Point of Interest	PreT-SF-ROCK-HyFRC		PreT-SF-ROCK	
	North Direction	South Direction	North Direction	South Direction
Maximum Moment [kip-in.]	-3617	3885	-3619	3731
Drift Ratio at Maximum Moment [%]	-4.55	6.78	-4.52	8.53
80% of Maximum Moment [kip-in.]	-2931	3150	-2955	3169
Drift Ratio of 80% of Maximum Moment [%]	-8.24	N/A	N/A	N/A

5.3 EFFECTIVE FORCE ACTING ON SPECIMENS

The effective force acting on the column was calculated by dividing the base moment, M, by h_1, the distance from the column-footing interface to the mid-point of the MTS actuator.

$$F_{eff} = \frac{M}{h_1} \tag{5.4}$$

Figures 5-8 and 5-9 illustrate the effective force versus displacement plots, whereas Table 5.7 lists the maximum effective forces observed and the corresponding drift levels.

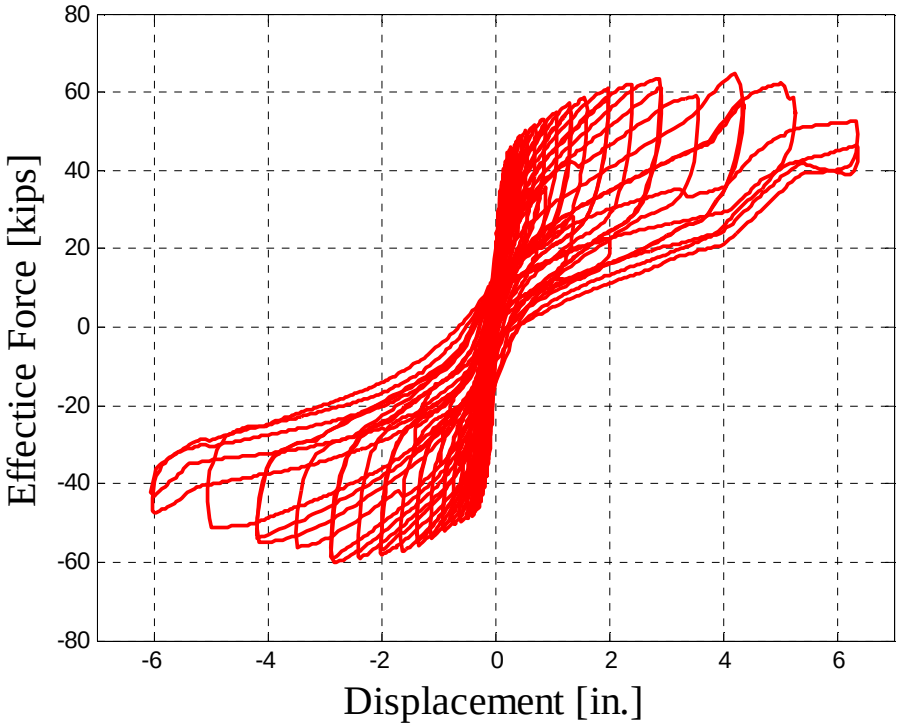

Figure 5.8 **Effective force-displacement response for Specimen PreT-SF-ROCK-HyFRC.**

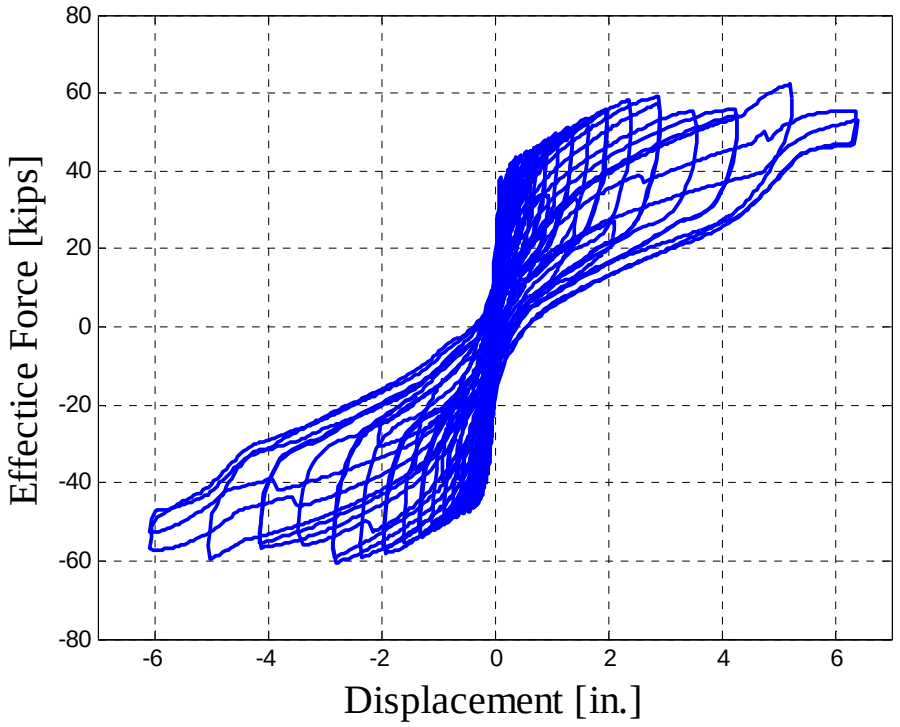

Figure 5.9 **Effective force-displacement response for Specimen PreT-SF-ROCK.**

Table 5.7 Summary of effective forces.

Point of Interest	PreT-SF-ROCK-HyFRC		PreT-SF-ROCK	
	North Direction	South Direction	North Direction	South Direction
Maximum Effective Force [kips]	-60.3	64.7	-60.3	62.2
Drift Ratio at Maximum Effective Force [%]	-4.55	6.78	-4.52	8.53
80% of Maximum Effective Force [kips]	-48.9	52.5	-49.3	52.8
Drift Ratio of 80% of Maximum Effective Force [%]	-8.24	N/A	N/A	N/A

5.4 COLUMN ROTATIONS

Researchers measured column rotations using three methods: the "curvature rod" system, inclinometers and the Optotrac LED tracking system (Section 3.1.2.4). The relative rotation between two adjacent cross-sections was calculated using Equation 5.5:

$$\theta_i = \frac{\delta_{i,N} - \delta_{i,S}}{L_i} \tag{5.5}$$

where θ_i is the rotation at a specified column height, $\delta_{i,N}$ is the displacement measured by the north potentiometer, $\delta_{i,S}$ is the displacement measured by the south potentiometer and L_i is the horizontal distance between the north and south potentiometers. The absolute rotation at each cross-section was determined by summing the relative rotations beneath the height of interest.

Figures 5.10 and 5.11 show the absolute column rotations derived from the curvature rod measurements at the following drift levels: ±0.3%, ±0.7%, ±1.2%, ±2.0%, ±3.0% and ±4.0%. These drift levels are the same that levels for which Finnsson et al. (2013) reported rotations, which allows for easy comparison of performance.

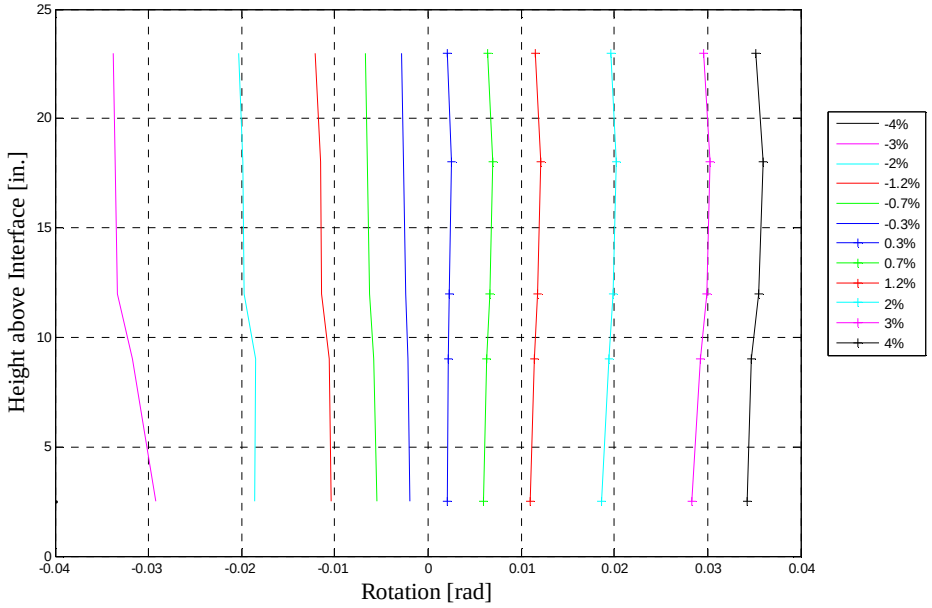

Figure 5.10 Rotations of PreT-SF-ROCK-HyFRC as measured with curvature rod system.

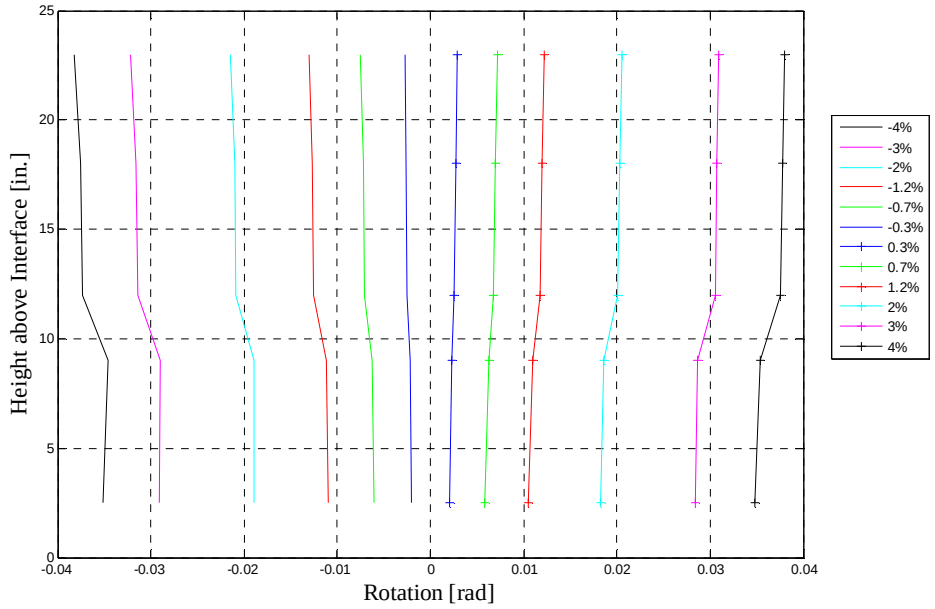

Figure 5.11 Rotations of PreT-SF-ROCK as measured with curvature rod system.

One of the potentiometers reached the end of its stroke as the column transitioned from +4% drift to -4% drift in test PreT-SF-ROCK-HyFRC. As a result, it provided erroneous measurements for the rotations at -4% drift, so rotations at this drift level are not shown.

Inclinometers were the second method used to measure column rotation. Figures 5.12 and 5.13 show the absolute column rotations measured with these instruments.

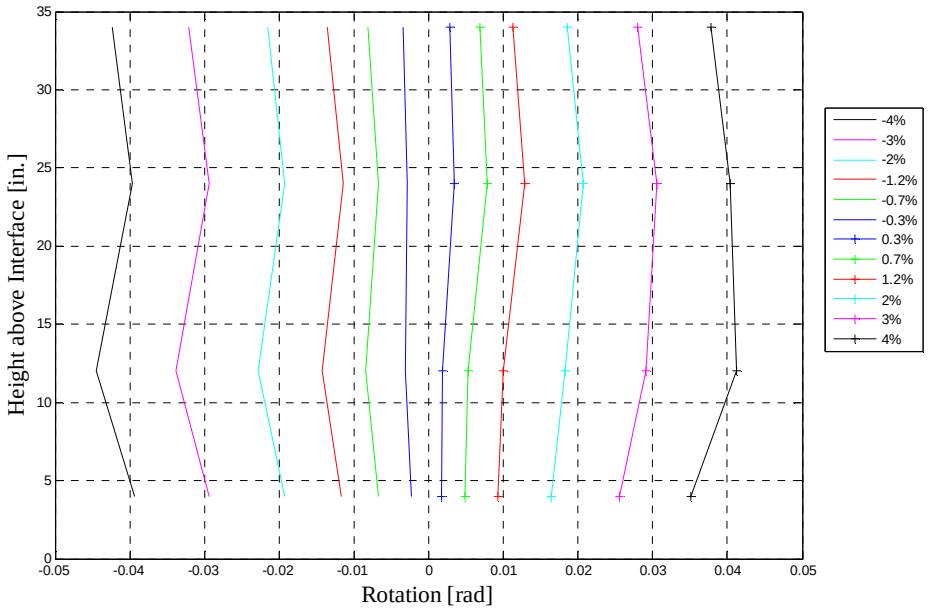

Figure 5.12 Rotations of PreT-SF-ROCK-HyFRC as measured from Inclinometers.

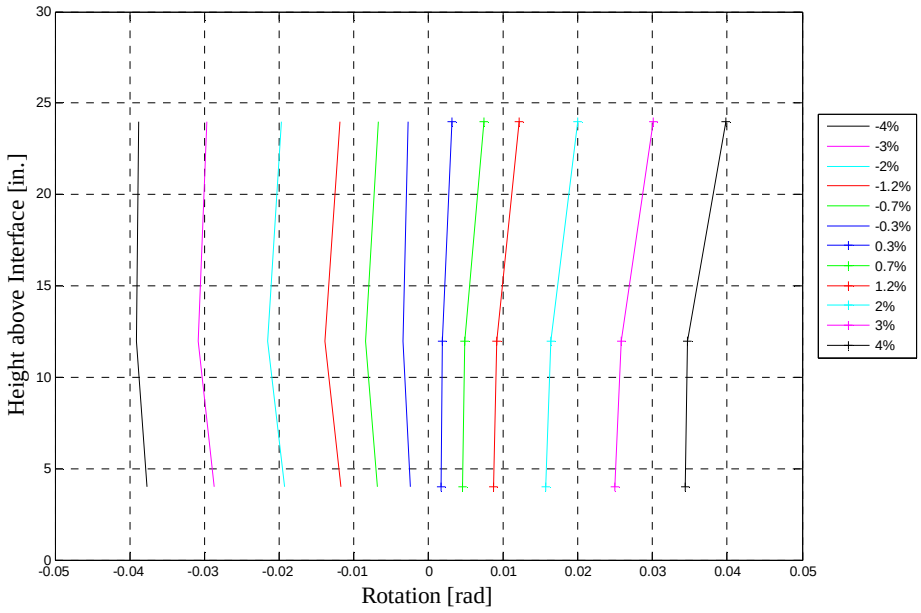

Figure 5.13 Rotations of PreT-SF-ROCK as measured from Inclinometers.

The detailed rotation pattern in PreT-SF-ROCK-HyFRC seems implausible, because it indicates that the column straightened between the second and third inclinometers (12”

and 24”). Researchers did not observe such straightening behavior. Researchers attributed this effect to the instruments’ tolerances. Additionally, the top inclinometer (34”) did not take any measurements throughout the entire PreT-SF-ROCK test.

An LED motion capture system (Optotrac System) was the third method used to measure column rotation. Figures 5.14 and 5.15 show the absolute column rotations measured with this system.

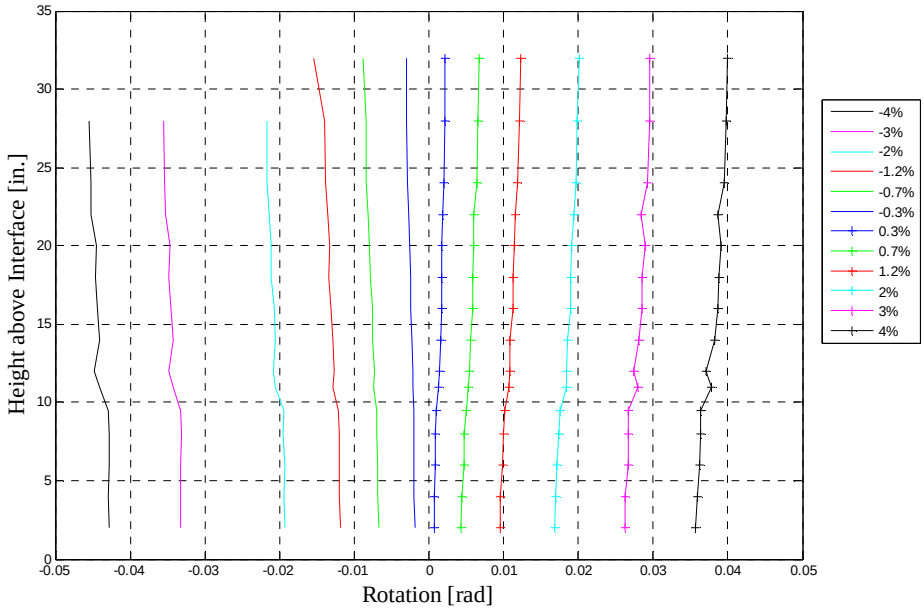

Figure 5.14 Rotations of PreT-SF-ROCK-HyFRC as measured with Optotrac system.

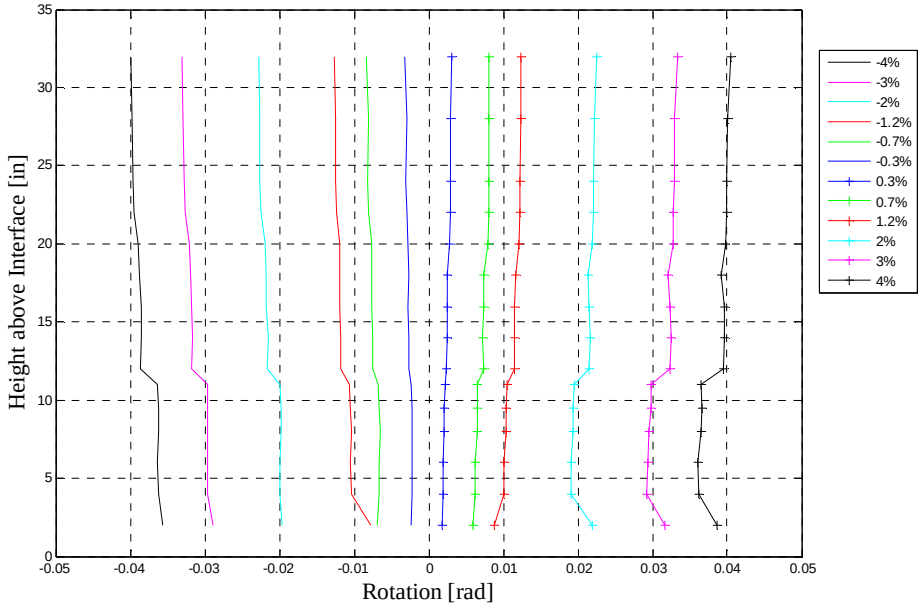

Figure 5.15 Rotations of PreT-SF-ROCK as measured with Optotrac system.

Of the three methods, the Optotrac data wais the most consistent. It also showed a slight jump in rotation at the top of the steel shoe, which wais consistent with observation of hairline cracks there. Both of these facets imply that the Opototrac data is the most reliable.

The Optotrac data, however, does show one peculiarity. In specimen PreT-SF-ROCK-HyFRC, the Optotrac data indicates that at drift ratios ±3.0% and ±4.0% the rotations were not symmetric. This asymmetry is inconsistent with researchers' expectations. Additionally, this asymmetry does not occur in the Optotrac data for specimen PreT-SF-ROCK. The asymmetry in Optotrac rotations for specimen PreT-SF-ROCK-HyFRC could be a result of column sliding; however, if this were the case, the Optotrac data should report rotations in the positive direction lower than what would be expected nominally, which it does not. As a result, researchers are unsure what caused this asymmetry.

The three methods used to determine column rotation are compared at ±2% drift in figures 5.16 and 5.17 below.

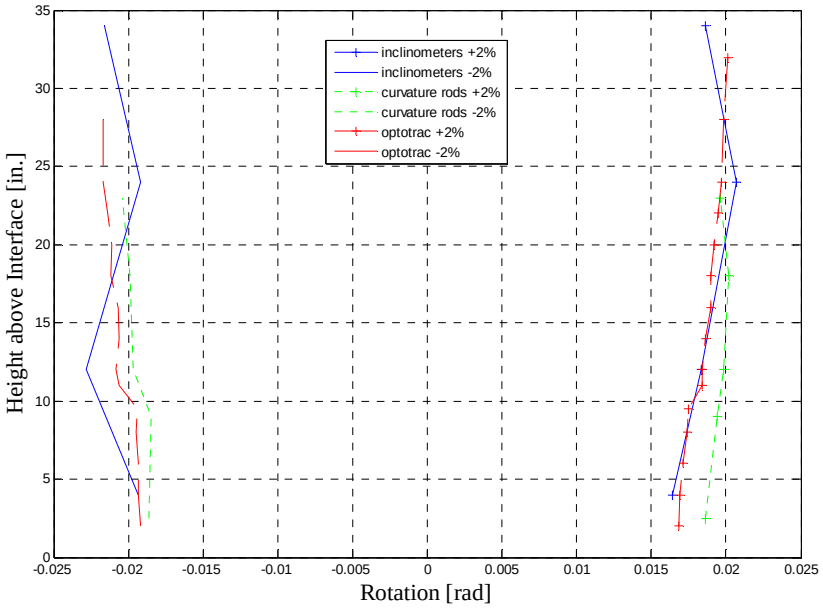

Figure 5.16 Comparison of measured rotations for PreT-SF-ROCK-HyFRC.

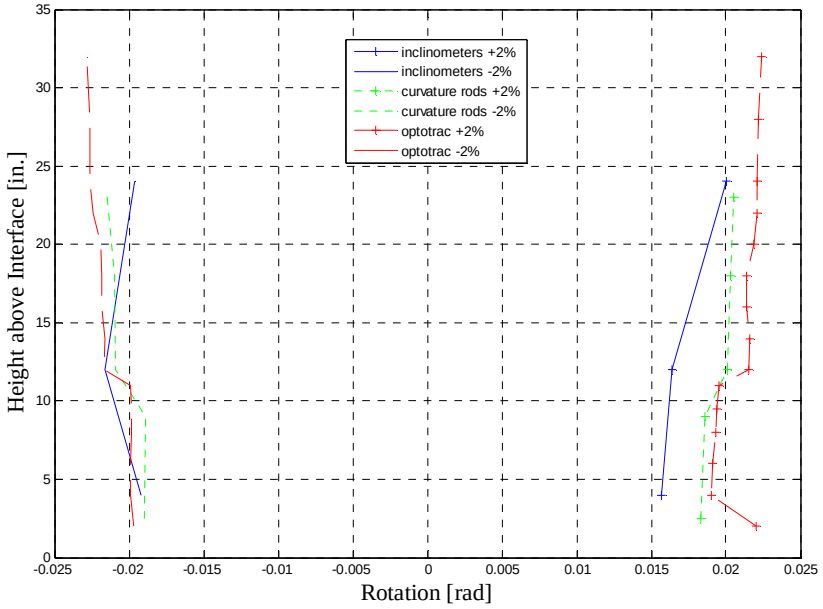

Figure 5.17 Comparison of measured rotations for PreT-SF-ROCK.

The plots above show that the three rotation methods are mainly consistent, especially in the PreT-SF-ROCK-HyFRC test, for which the values fall within 5% of each other for positive drifts and 16% for negative drifts. The three methods agree less in the PreT-SF-ROCK test where the values fall within 24% of each other for positive drifts and 13% for negative drifts. Once again, the Optotrac data seems the most reliable followed by the curvature rod system. The inclinometer manufacturer (Spectron) reports an accuracy of ±0.5° for the instrument. This is 13% of the peak rotation, suggesting that the instrument's accuracy could inhibit its performance relative to the other two methods.

Regardless of small discrepancies, all of the data appears to suggest the same thing; the columns acted as nearly rigid bodies with the majority of rotation occuring at the column-footing interface. These results are consistent with what researchers observed during both tests. This behavior was expected due to the steel shoe rocking feature. A smaller portion of rotation also formed at a column height of 10", the interface between the top of the steel shoe and the remainder of the column. This slight relative rotation was also expected since the column stiffness in the region above the steel shoe is much lower than that within the steel shoe. PreT-SF-ROCK experienced slightly more rotation gain at the 10" elevation than did PreT-SF-ROCK-HyFRC, best illustrated in figures 5.13 and 5.14. This result is consistent with the observations that PreT-SF-ROCK suffered more hairline cracking than did PreT-SF-ROCK-HyFRC.

5.5 COLUMN CURVATURES

Researchers calculated column curvatures using data from the curvature rod system and the Optotrac LED tracking system. The inclinometer rotation data was not converted to curvatures,

because it appeared to be insufficiently accurate. Average curvatures were calculated using the previously found rotations and Equation 5.6:

$$\varphi_i = \frac{\delta_{i,N} - \delta_{i,S}}{L_i} / H_i \tag{5.6}$$

where φ_i is the average curvature over the monitored height, δ_i,N and δ_i,S are the measured displacements on the column's respective north and south faces, L_i is the horizontal distance between the north and south potentiometers, and H_i is the initial vertical distance between adjacent curvature rods.

Figures 5.18 and 5.19 show the average curvature of the two columns as measured by the curvature-rod system at the same drift levels reported for rotations: ±0.3%, ±0.7%, ±1.2%, ±2.0%, ±3.0% and ±4.0%.

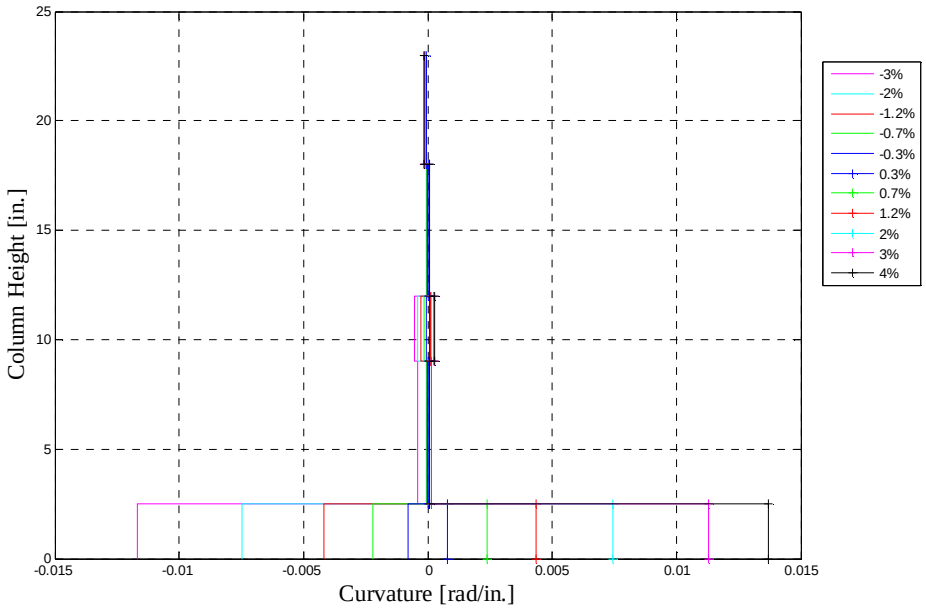

Figure 5.18 Average curvatures of PreT-SF-ROCK-HyFRC, calculated from curvature rod system.

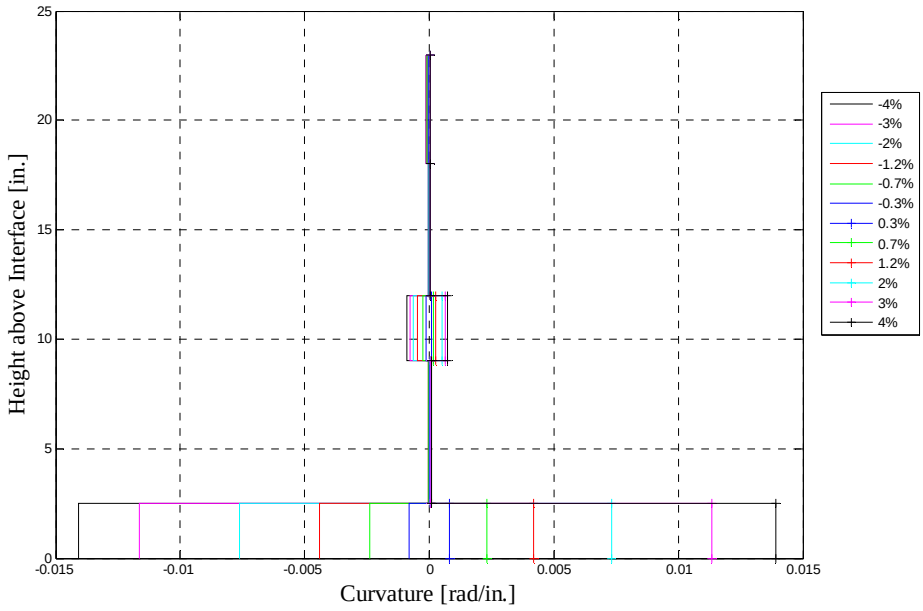

Figure 5.19 Average curvatures of PreT-SF-ROCK, calculated from curvature rod system.

The two plots above that the majority of average curvature occurred at the base of the column with a secondary region of curvature occurring at the top of the steel shoe. The average curvature of PreT-SF-ROCK was nearly identical to that of PreT-SF-ROCK-HyFRC at the column's base; however, it was larger near the top of the steel shoe. Researchers expected this result because PreT-SF-ROCK experienced more hairline cracking in this region than did PreT-SF-ROCK-HyFRC.

Figures 5.20 and 5.21 document the average curvature distribution of the two columns as measured by the Optotrac LED tracking system.

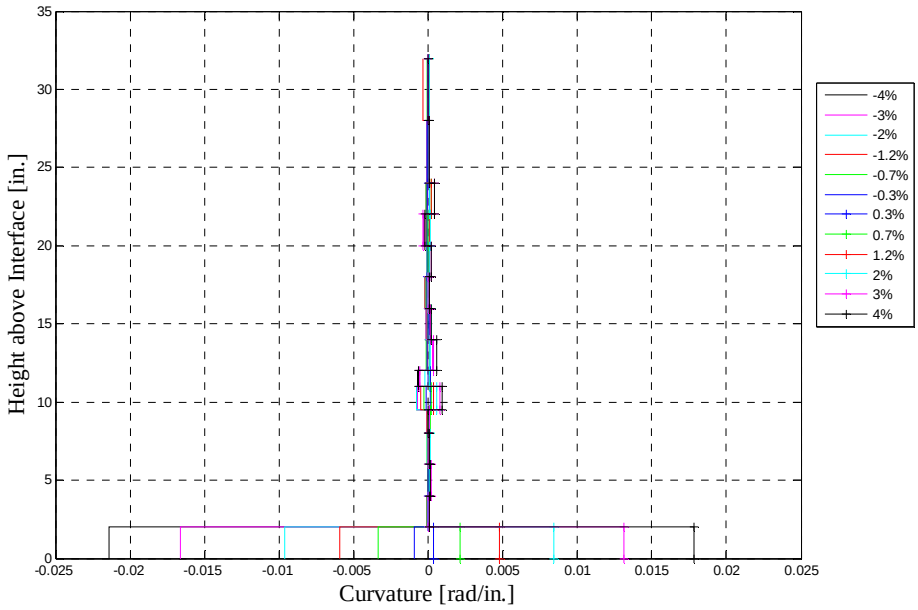

Figure 5.20 Average curvatures of PreT-SF-ROCK-HyFRC, calculated from Optotrac System.

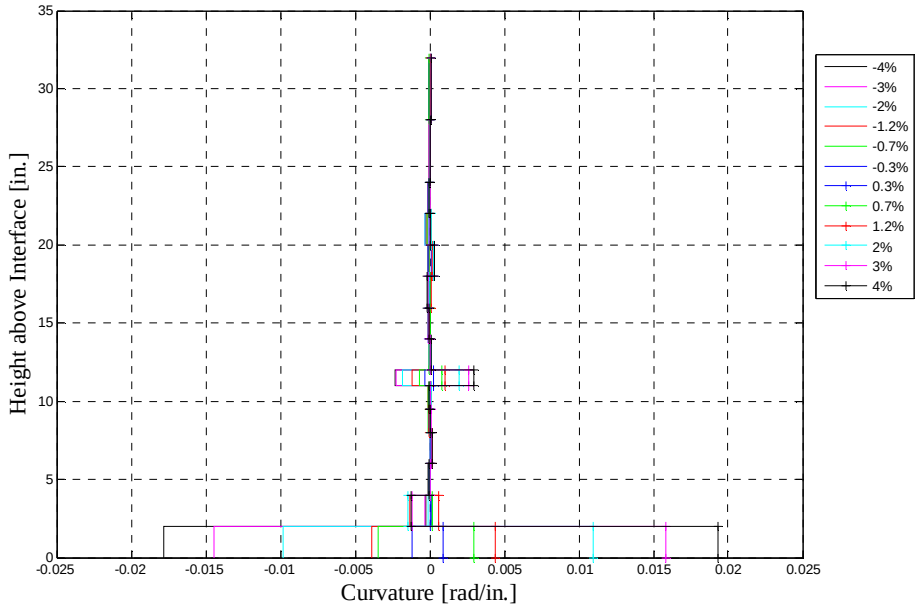

Figure 5.21 Average curvatures of PreT-SF-ROCK, calculated from Optotrac system.

The curvatures derived from the Optotrac data are similar to those from the curvature-rod system. Again, the two plots show that the columns experienced high curvatures at the column-footing interface and little curvature elsewhere, except for immediately above the steel shoe where the column undergoes a change in stiffness. As

expected, specimen PreT-SF-ROCK had a higher curvature above the steel shoe region than did PreT-SF-ROCK-HyFRC.

5.6 STRAIN IN LONGITUDINAL REINFORCEMENT

5.6.1 No. 4 Bars

Figures 5.22-5.24 show the strain profiles of the No.4 reinforcing bars for both tests. The strains are plotted at the three measured locations: 7" below the interface, at the interface and 7" above the interface. In these plots, the origin for elevation is taken at the column-footing interface; therefore, positive elevations refer to locations above the interface whereas negative elevations refer to locations below the interface. During the test, the majority of strain gauges ceased to work at large drifts. For this reason, the plots show the strain profiles at only three drift levels: ±0.3%, ±0.7%, and ±1.2%. Only one strain gauge at the interface functioned during the PreT-SF-ROCK-HyFRC test. Consequently, only one plot is shown for that test (south bar).

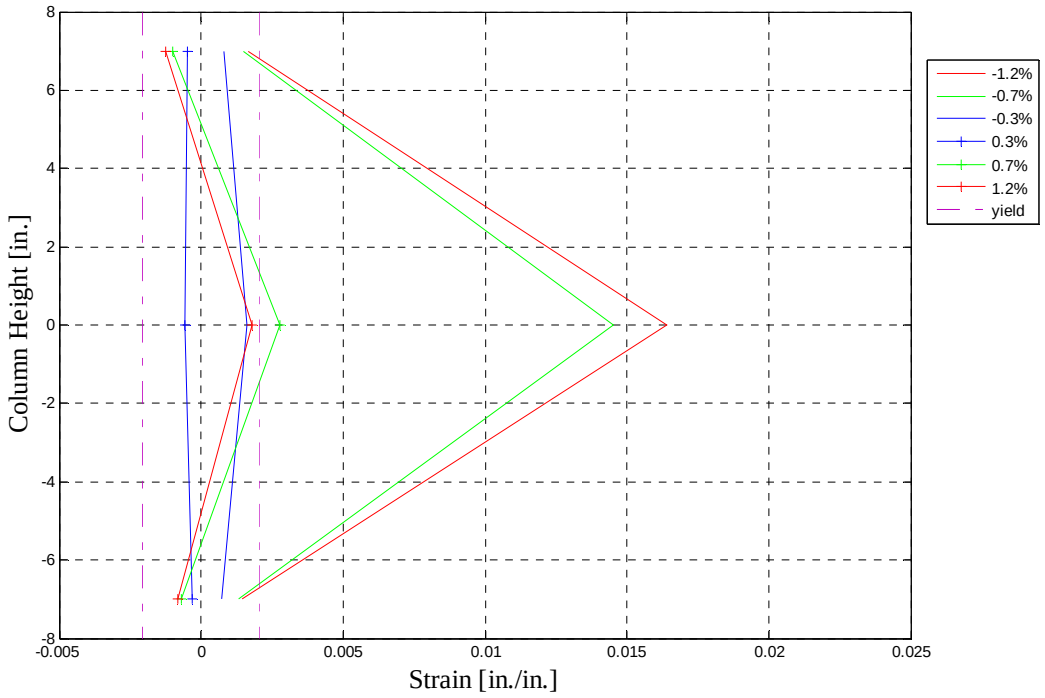

Figure 5.22 Strain profiles for South No 4 Bar, PreT-SF-ROCK-HyFRC.

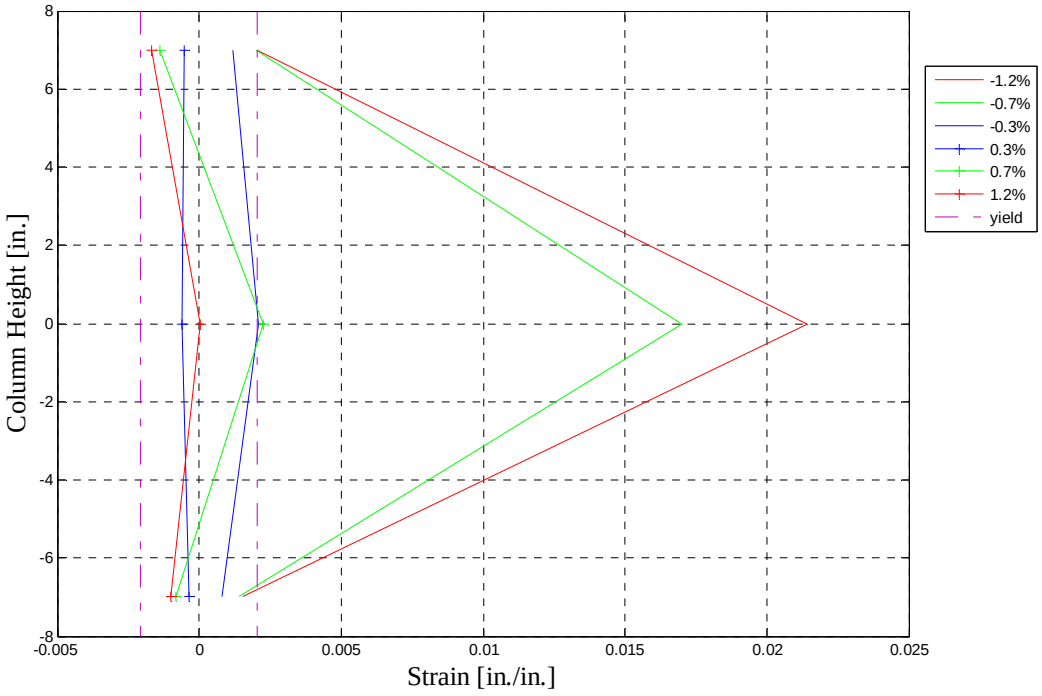

Figure 5.23 Strain profiles for South No 4 Bar, PreT-SF-ROCK.

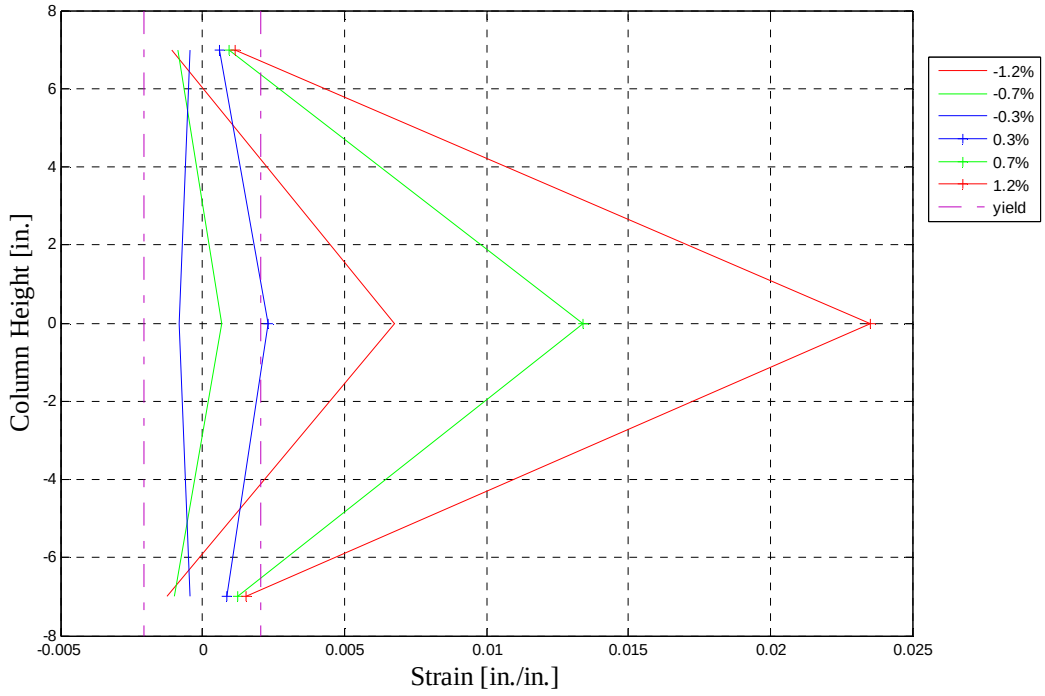

Figure 5.24 Strain profiles for North No 4 Bar, PreT-SF-ROCK.

For all three plots, the measured compressive and tensile strains are approximately symmetric (about the zero strain axis) at 7" above and 7" below the interface. In contrast, this is not the case for the strains measured at the interface, where the tensile strains greatly exceed any compressive strains.. One feature of both columns was the steel shoe. During the test, researchers noticed that the column rocked about the shoe's outer edges as the column was laterally loaded. This rocking behavior would cause tension in both the North and South bars at the same drift level if the column's neutral axis was located the column edge. If this were the case, then the bar opposite the direction of loading would experience high tensile strains while the bar in the direction of loading would experience small tensile strains. The above plots show such a pattern. Additionally, at low drift levels (e.g., ±0.3%) the bars in the direction of loading show compressive strains. This occurrence could correspond to the steel shoe not yet lifting off and rocking about its outer edge. In such a case, the neutral axis would not bet at the outer edge, and therefore, the bar in the direction of loading should be in compression.

To understand the bars' strain behavior better, researchers created strain vs. drift histories for each pair of working strain gauges located on the No. 4 longitudinal bars. Figures 5.25-5.28 show these results. Since most of the strain gauges broke at some point during the test, each plot only contains data until the respective gauge's point of breaking. Note that the plots for the strain gauge pairs above and below the interface have a different scale than the plots for the strain gauge pairs at interface. The scales are different because the strains measured at the interface were an order of magnitude higher than the strains measured above and below the interface.

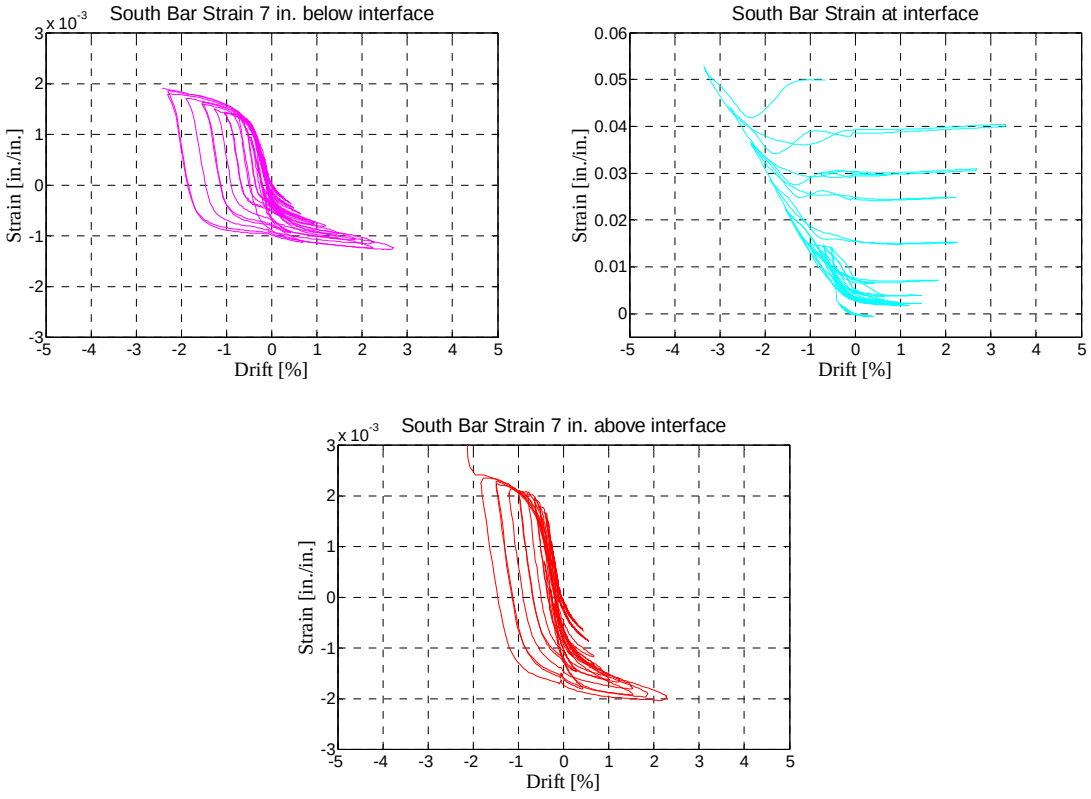

Figure 5.25 Strain vs. drift in South No 4 Bar, PreT-SF-ROCK-HyFRC.

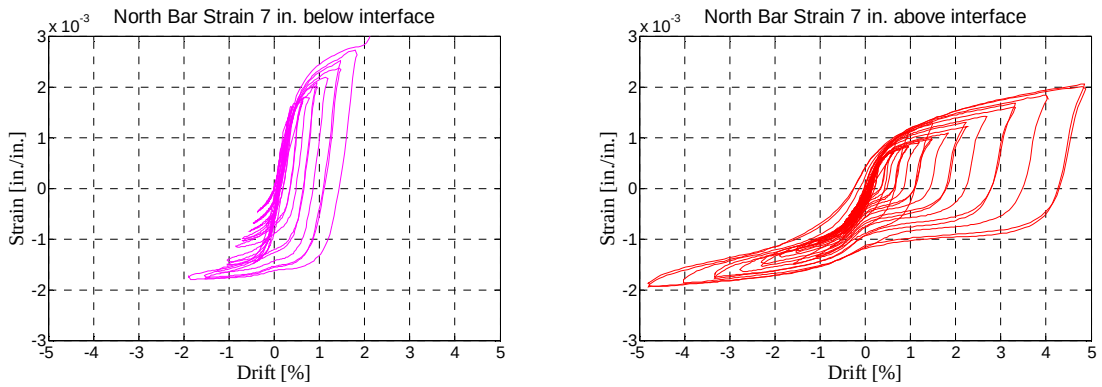

Figure 5.26 Strain vs. drift in North No 4 Bar, PreT-SF-ROCK-HyFRC.

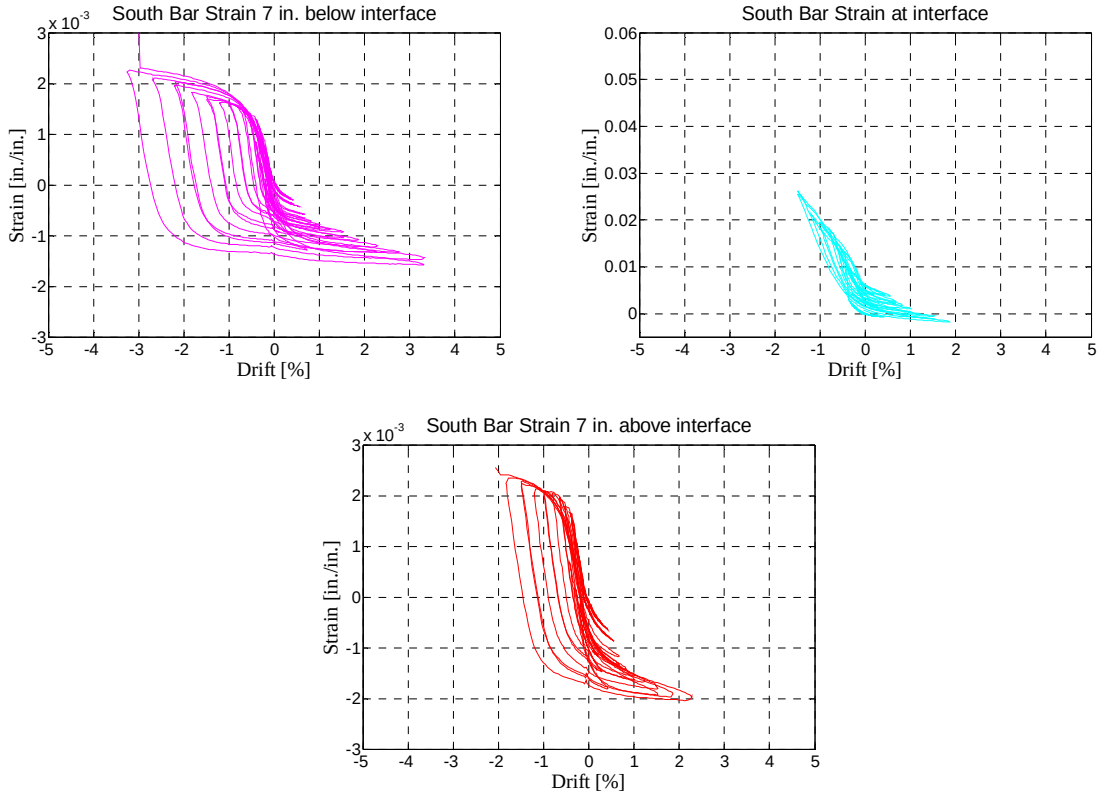

Figure 5.27 Strain vs. drift in South No 4 Bar, PreT-SF-ROCK.

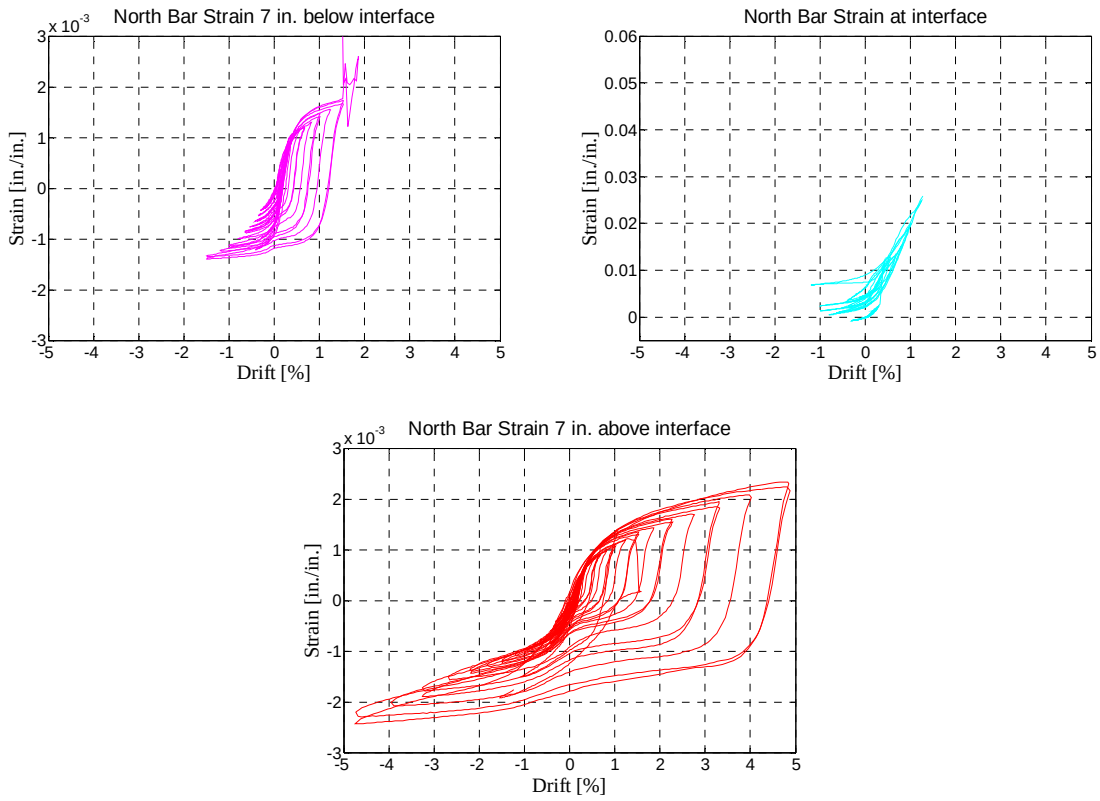

Figure 5.28 Strain vs. drift in North No 4 Bar, PreT-SF-ROCK.

The strain histories are consistent between the two specimens and between the north and south bars. The strains are generally slightly larger when the bar is in tension as opposed to compression, which is consistent with previous results from Finnsson et al. (2013). This difference is also consistent with the observed vertical displacements (Sec. 5.20). When the bar was in tension, the crack at the base was wide. Conversely, when the bar was in compression, no visible downward movement of the steel plate at its base was apparent. Additionally, the strains measured 7" below the interface are comparable to those measured 7" above the interface.

5.6.2 No. 6 Bars

Figures 5.29-5.32 show the strain profiles of the No. 6 reinforcing bars for both column tests. The strains are plotted at the two monitored locations, 1" and 7" above the interface. In addition to the three drift levels considered in the plots for the No. 4 bar strain profiles: ±0.3%, ±0.7%, and ±1.2%, the profiles for the No. 6 bars are also reported for a drift ratio of 2.0%.

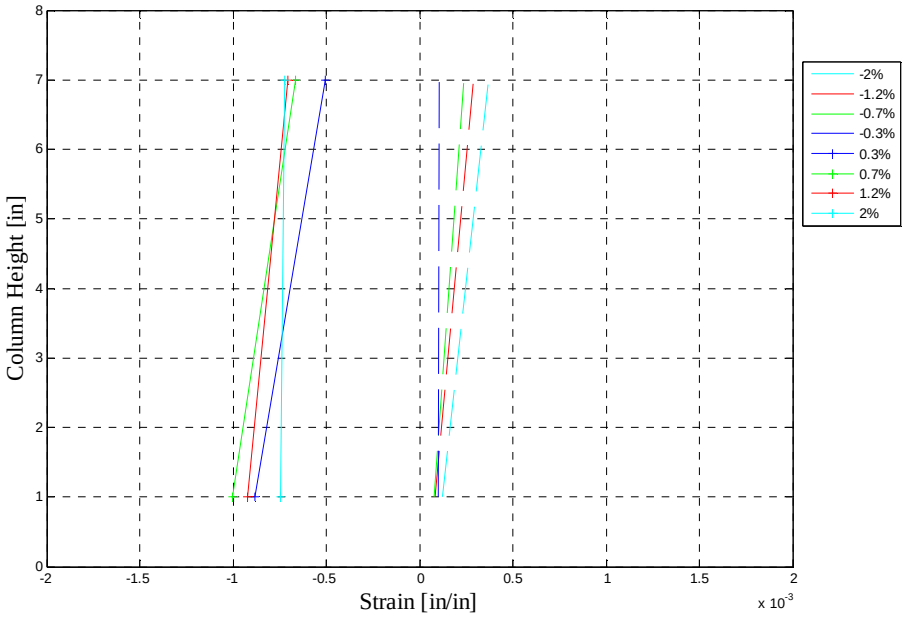

Figure 5.29 Strain profiles for Southeast No 6 Bar, PreT-SF-ROCK-HyFRC.

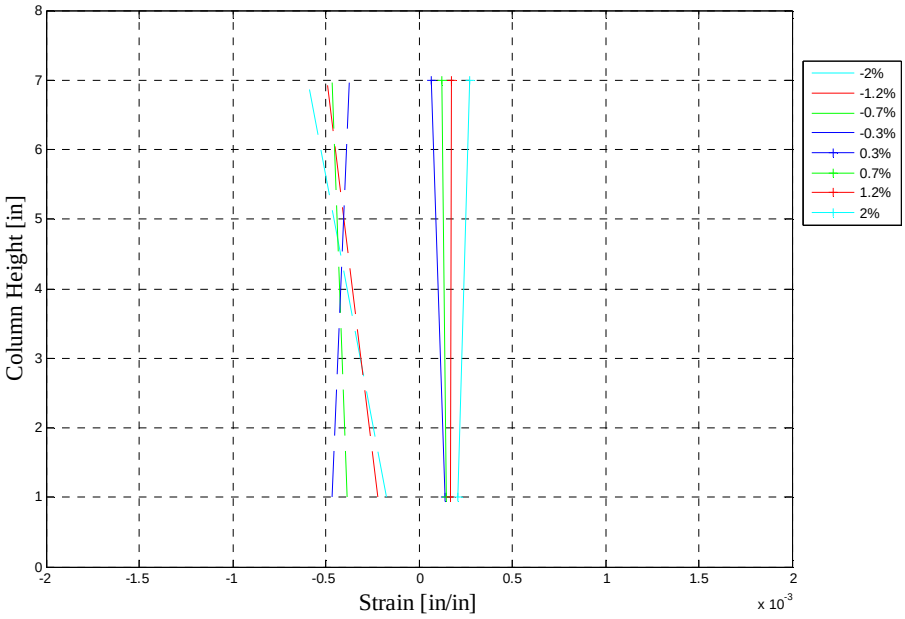

Figure 5.30 Strain profiles for Northwest No 6 Bar, PreT-SF-ROCK-HyFRC.

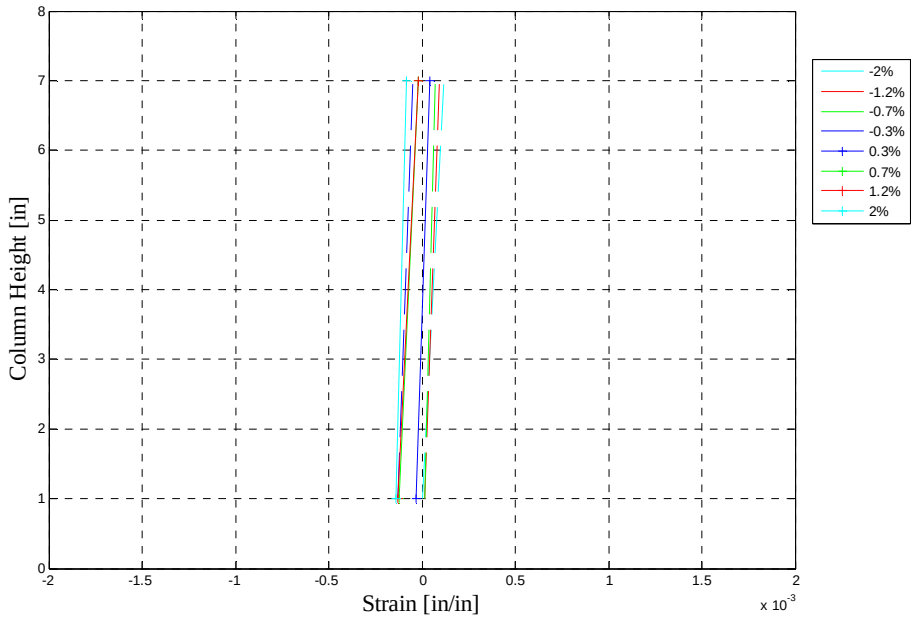

Figure 5.31 Strain profiles for Southeast No 6 Bar, PreT-SF-ROCK.

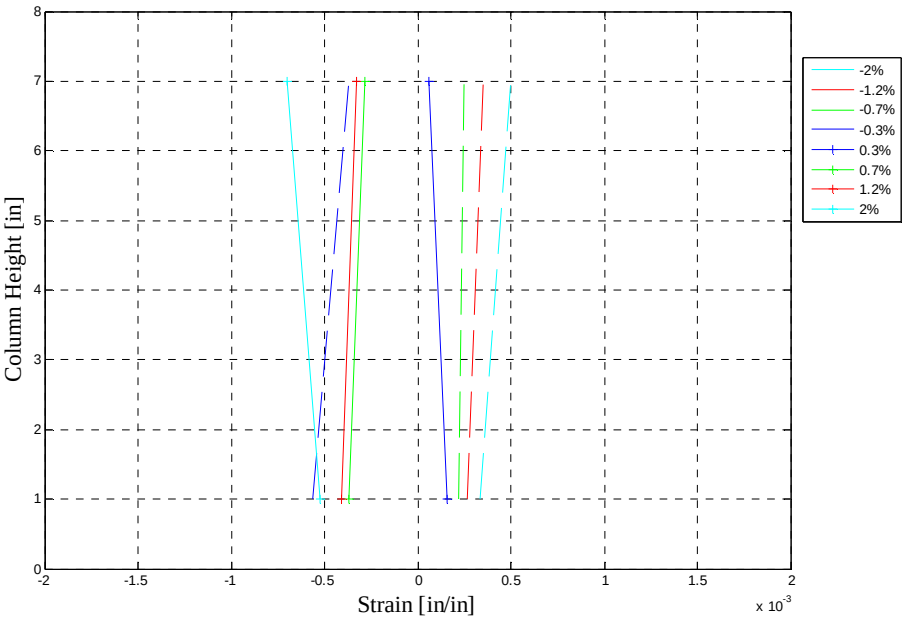

Figure 5.32 Strain profiles for Northwest No 6 Bar, PreT-SF-ROCK.

Additionally, the measured tensile strains were larger 7” above interface while the compressive strain appears larger at 1” above interface. This difference was expected. The compressive stress is more concentrated at lower elevations, hence requiring the No. 6 bars to distribute that stress to the surrounding concrete. Conversely, cracking near the top of the

steel shoe would cause a loss of tensile capacity in the concrete, hence requiring the No. 6 bars to compensate this loss by carrying additional tensile stress. The strain profile for the Northwest bar in specimen PreT-SF-ROCK appears unrealistic. At +0.3% drift the bar exhibits tensile strain while at +0.7%, +1.2% and 2.0% drift the bar exhibits compressive strain. In the similar directions of loading, the bar should experience the same type of stress, either compressive or tensile. This could be the result of faulty strain gauge installation.

Figures 5.33-5.36 show the strain vs. drift plots for the No. 6 bars. Unlike the No. 4 bars, the No. 6 bars did not yield in either test. As a result, all working strain gauges functioned throughout the entire duration of both tests. Consequently, the plots were able to depict the bars' strain levels at extreme drift levels.

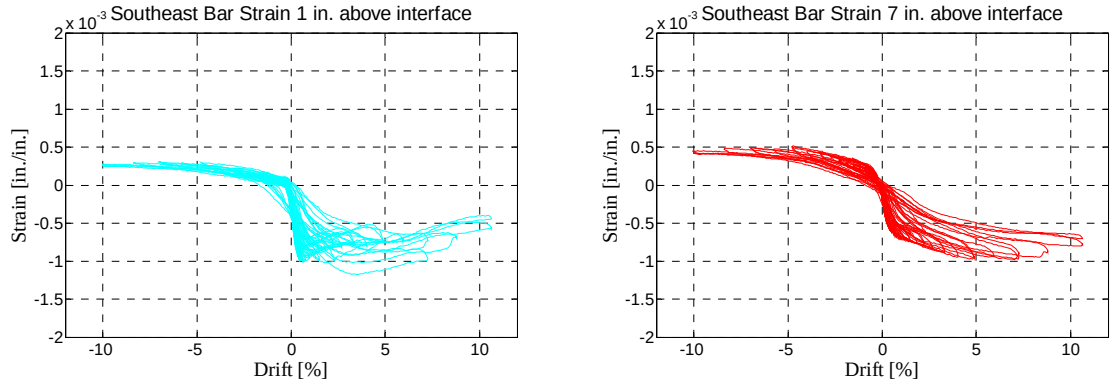

Figure 5.33 Strain vs. drift in Southeast No 6 Bar, PreT-SF-ROCK-HyFRC.

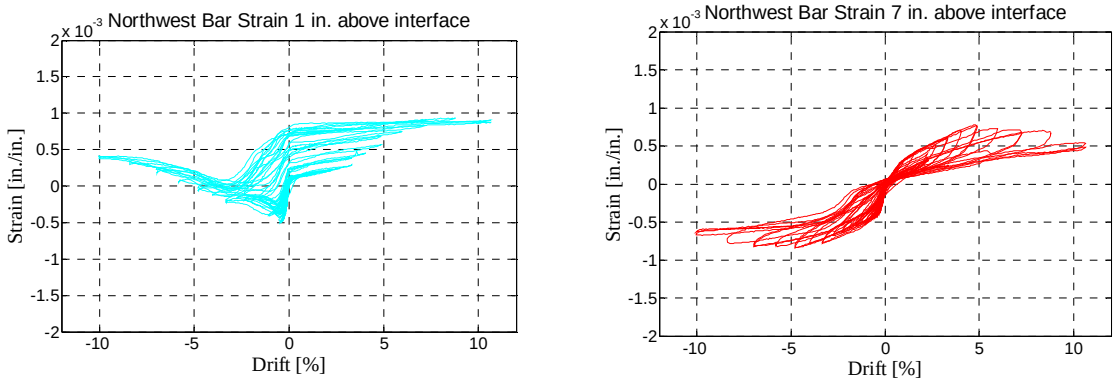

Figure 5.34 Strain vs. drift in Northwest No 6 Bar, PreT-SF-ROCK-HyFRC.

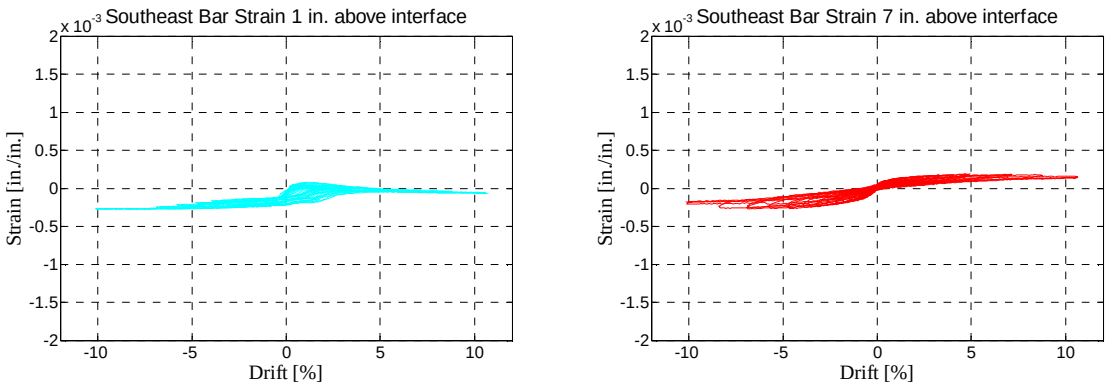

Figure 5.35 Strain vs. drift in Southeast No 6 Bar, PreT-SF-ROCK.

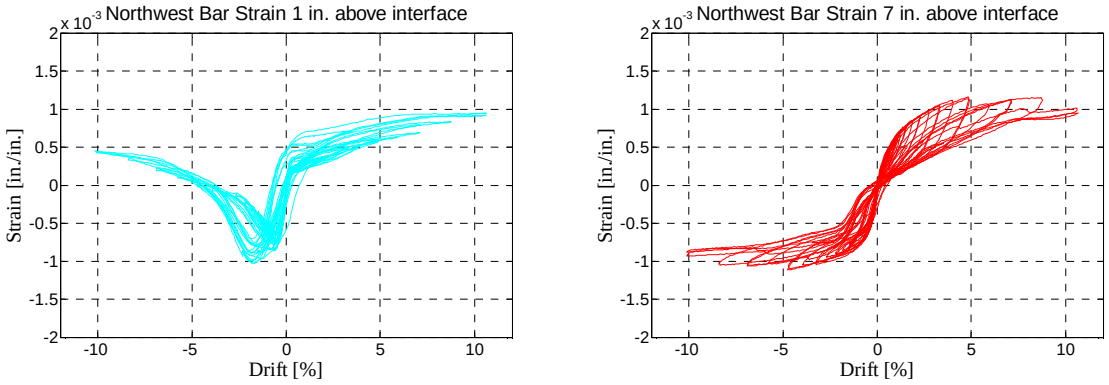

Figure 5.36 Strain vs. drift in Northwest No 6 Bar, PreT-SF-ROCK.

The above plots provide interesting results. First, the relatively low strain values in Figure 5.34 compared to the other three plots suggest that the strain gauge malfunctioned. If the results from Figure 5.34 are omitted, the behavior of the No. 6 bars in PreT-SF-ROCK-HyFRC and PreT-SF-ROCK are nearly identical. The northwest bar in PreT-SF-ROCK appears to have experienced slightly higher strains than the No. 6 bars in PreT-SF-ROCK-HyFRC, but the shapes are similar.

The bars' hysteretic behavior 7" above the column-footing interface is symmetric, reaching strains approximately a quarter to half of the yield strain. The bars hysteretic behavior 1" above the interface, on the other hand, is not symmetric. In the expected tensile direction, the plots' shapes resemble typical hysteretic behavior; in the expected compressive direction, however, the bars gain compressive strain until approximately 2% drift where they experience decreasing compressive strain and eventually (in two of four plots) tension. This measured behavior is consistent with the measured behavior of No. 4 bars (previous section). The North and South bars appeared to be in tension simultaneously.

5.7 STRAIN IN TRANSVERSE REINFORCEMENT

Figures 5.37 and 5.38 illustrate the transverse reinforcement strain vs. drift in both columns at the single measured location: 3" above the column-footing interface. The transverse

reinforcement did not yield during either test. As a result, the plots include data at high drift levels.

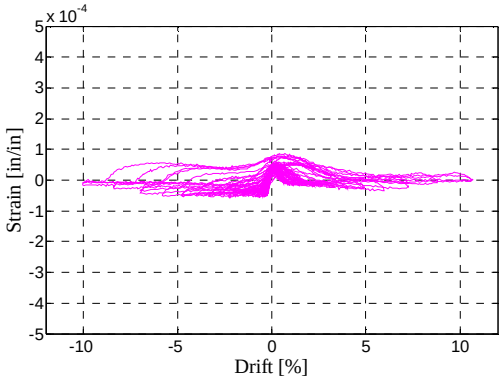

Figure 5.37 Strain vs. drift of transverse reinforcement in PreT-SF-ROCK-HyFRC.

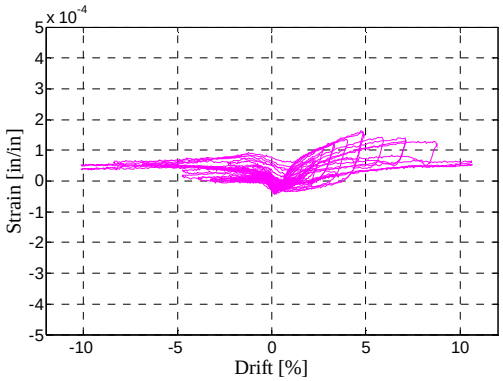

Figure 5.38 Strain vs. drift of transverse reinforcement in PreT-SF-ROCK.

The plots above show that the transverse reinforcement in specimen PreT-SF-ROCK experienced similar strains as the transverse reinforcement in specimen PreT-SF-ROCK-HyFRC. The maximum measured strain in both specimens was only 10% of the yield strain. These results indicate that the transverse reinforcement inside the steel shoe provides little benefit.

To evaluate this conclusion, researchers converted the spiral volumetric ratio to an equivalent steel tube, which resulted in an equivalent tube wall thickness of $\frac{A_{sp}}{s} = \mathbf{0.0328}$". This thickness is roughly one seventh that of the 0.25" wall thickness use in the specimen. Therefore, researchers expect the real tube to provide the majority of the confinement, especially near the base, where the welded circular plate stiffens it. The data above is consistent with this expectation.

5.8 STRAIN IN PRESTRESSING STRANDS

Strain gauges, placed in pairs in the strands' unbonded region, measured the strain history of the prestressing strands during both tests. Figures 3.39 and 3.40 show the strand strain vs. drift histories. These plots also include a horizontal line that denotes the nominal yield strain

of the strand, 0.0087 in./in. (based on a yield stress f_{py}=250 ksi and an elastic modulus, E_p=28600 ksi). In specimen PreT-SF-ROCK-HyFRC, none of the strain gauges on the Northeast strand functioned during the test. As a result, the strains for that strand are not reported.

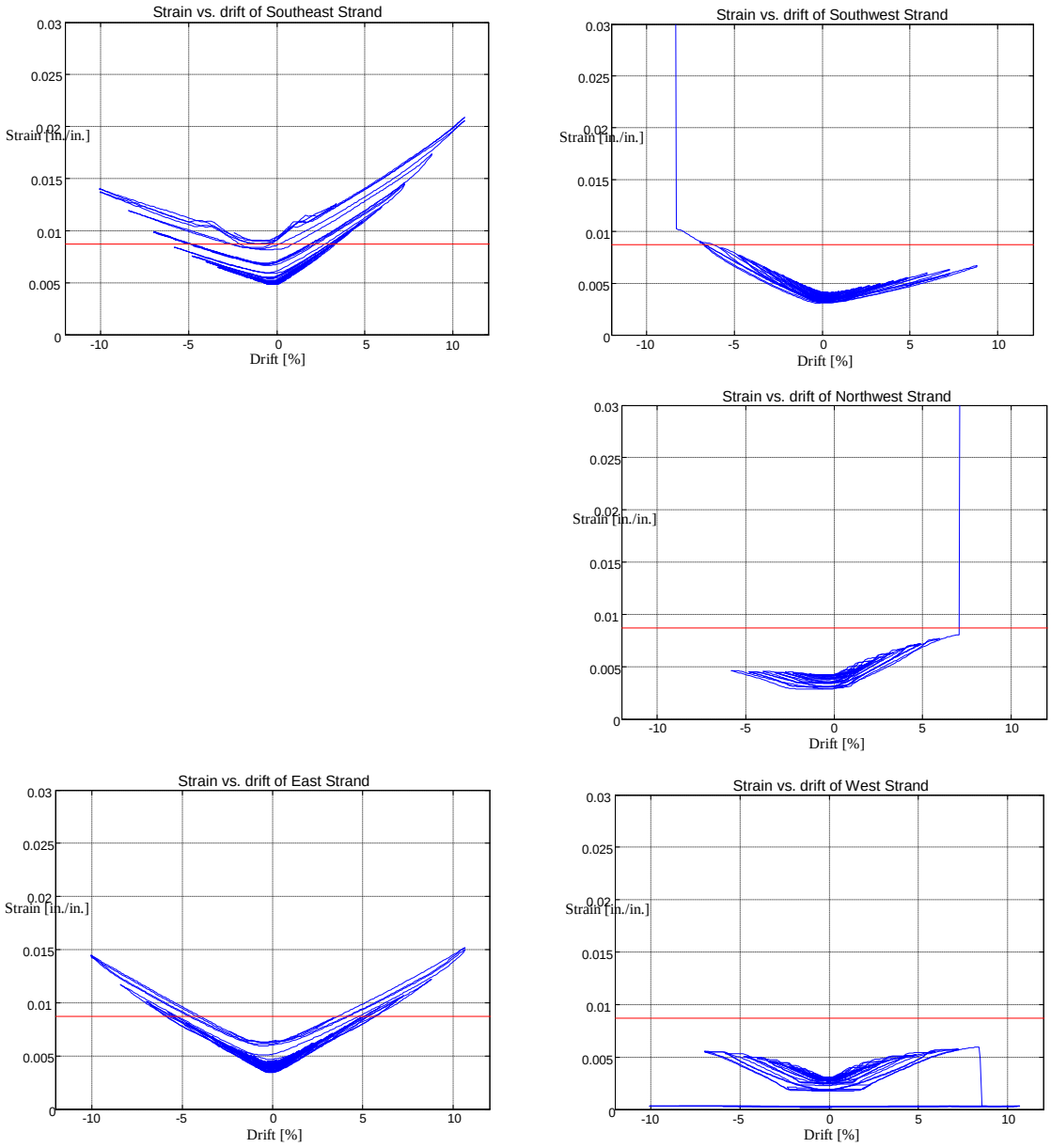

Figure 5.39 Strand strain gauge data versus drift (blue) and estimated yield strain (red) for PreT-SF-ROCK-HyFRC.

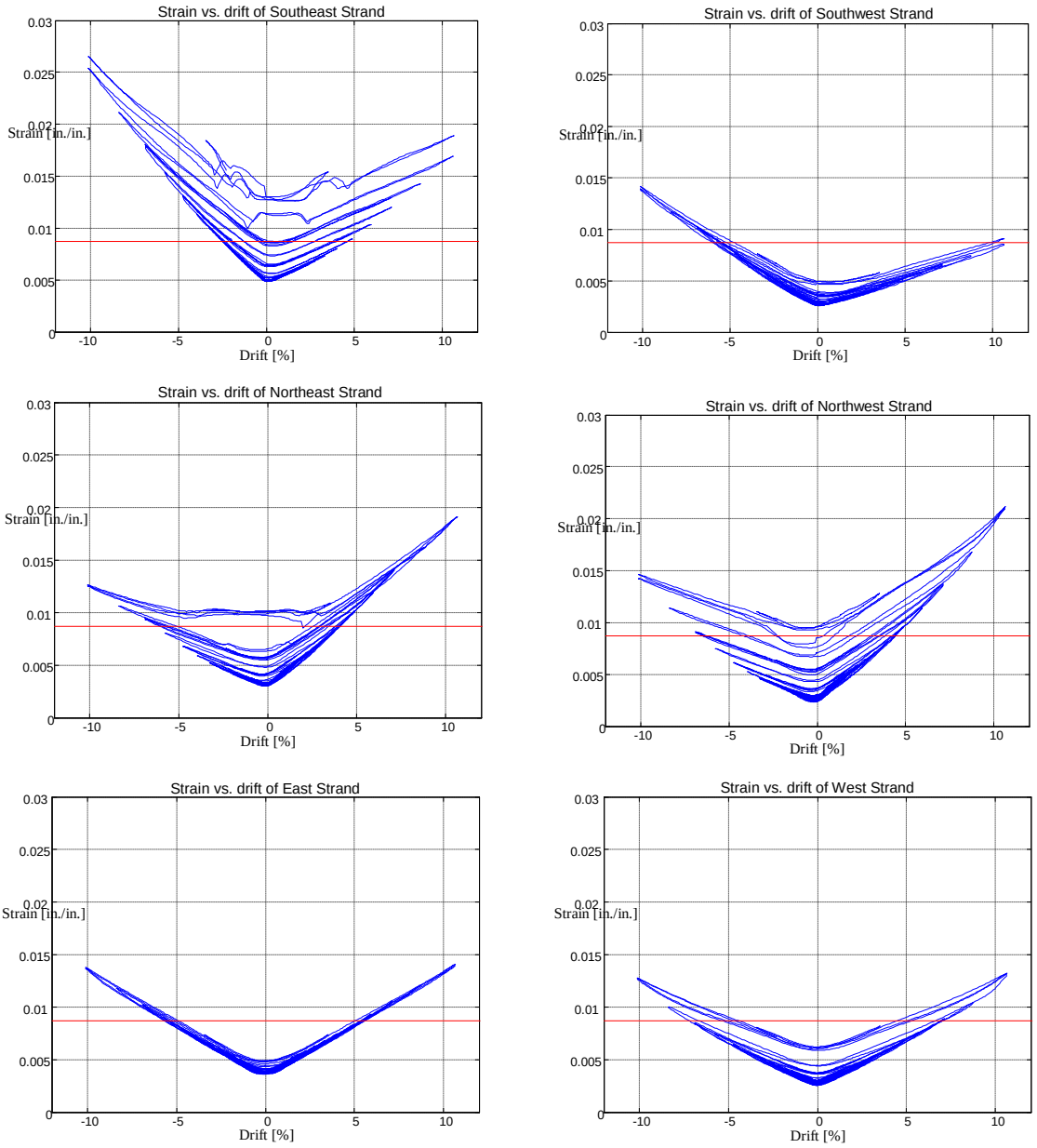

Figure 5.40 Strand strain gauge data versus drift (blue) and estimated yield strain (red) for PreT-SF-ROCK.

In all cases, the strand-drift histories form a V-shape. As the drift increases in the positive or negative direction, the tension strain increases. For the strands about the east-west axis (near the center of the column), the V-shape is symmetric. This is not the case for the off-centered strands, which exhibit asymmetric behavior. In particular, the northwest and northeast strands experience higher tensile strains at positive drifts, whereas the southwest and southeast strands experience higher tensile strain at negative drifts. This behavior is consistent with the strands' locations with respect to edge of the column, about which point it rocks.

The northwest and southwest strands in specimen PreT-SF-ROCK-HyFRC fractured at a drift ratio above 6% drift, whereas none fractured in specimen PreT-SF-ROCK. The fracture was not ductile as depicted by the sharp gain in strain in Figure 5.39. Additionally, the brittle failure occurred before any of the strands yielded. This observed failure is consistent with the theory that the dowel bar may have been misaligned and caused the strands to kink. Since a perfectly aligned dowel bar would be difficult to ensure in the field, future columns of this design should not include the dowel bar.

Aside from the three strands that fractured, the remaining strands in both columns all exceeded their yield strain. The strands offset to the north and south yielded much earlier (3-4% drift) than those along the east-west axis (5% drift), as expected. Additionally, the north and south strands reached strains up to 2.4 times the yield strain, whereas the east and west strands only reached strains equal to 1.6 times their nominal yield strain. These results suggest that the outer strands contributed more to the column re-centering, since they were subjected to higher strains at lower drift levels.

Lastly, as the strands cycled back and forth, the tensile strain at 0% drift steadily increased. This increase was far more pronounced for the outer (north and south) strands than it was for the center (east and west) strands. In fact, by the end of the test, the outer strands had measured strains above the yield level at 0% drift. The increase in strain at 0% drift was the result of intense cyclic yielding. While strands in previous tests experienced these zero drift changes, the changes were not nearly as dramatic as observed in PreT-SF-ROCK-HyFRC and PreT-SF-ROCK. This difference suggests that the strands in these two specimens underwent significantly more yielding, and consequently more strain hardening, than in previous tests.

5.9 STRAND SLIP

Load cells were placed at the top of the column on each strand to detect any slip that might occur during the tests. Due to the shorter bond length at the top of the column, researchers assumed that, if the strand slipped in the footing then it would also slip at the top of the column, hence load cells were not installed on the strands beneath the column. Researchers stressed each load cell to an initial load (approximately 5 kips) prior to testing by backing out the screw thread device after the strand chucks were set. During the test, any increase in that initial load would be a sign of anchorage slip. Figures 5.41 and 5.42 show the force in each load cell throughout the test. For comparison purposes, researchers zeroed each load cell so that their initial load was zero kips. In specimen PreT-SF-ROCK-HyFRC, the load cell on the southeast strand did not function during the test. As a result, that load cell is omitted from the plots.

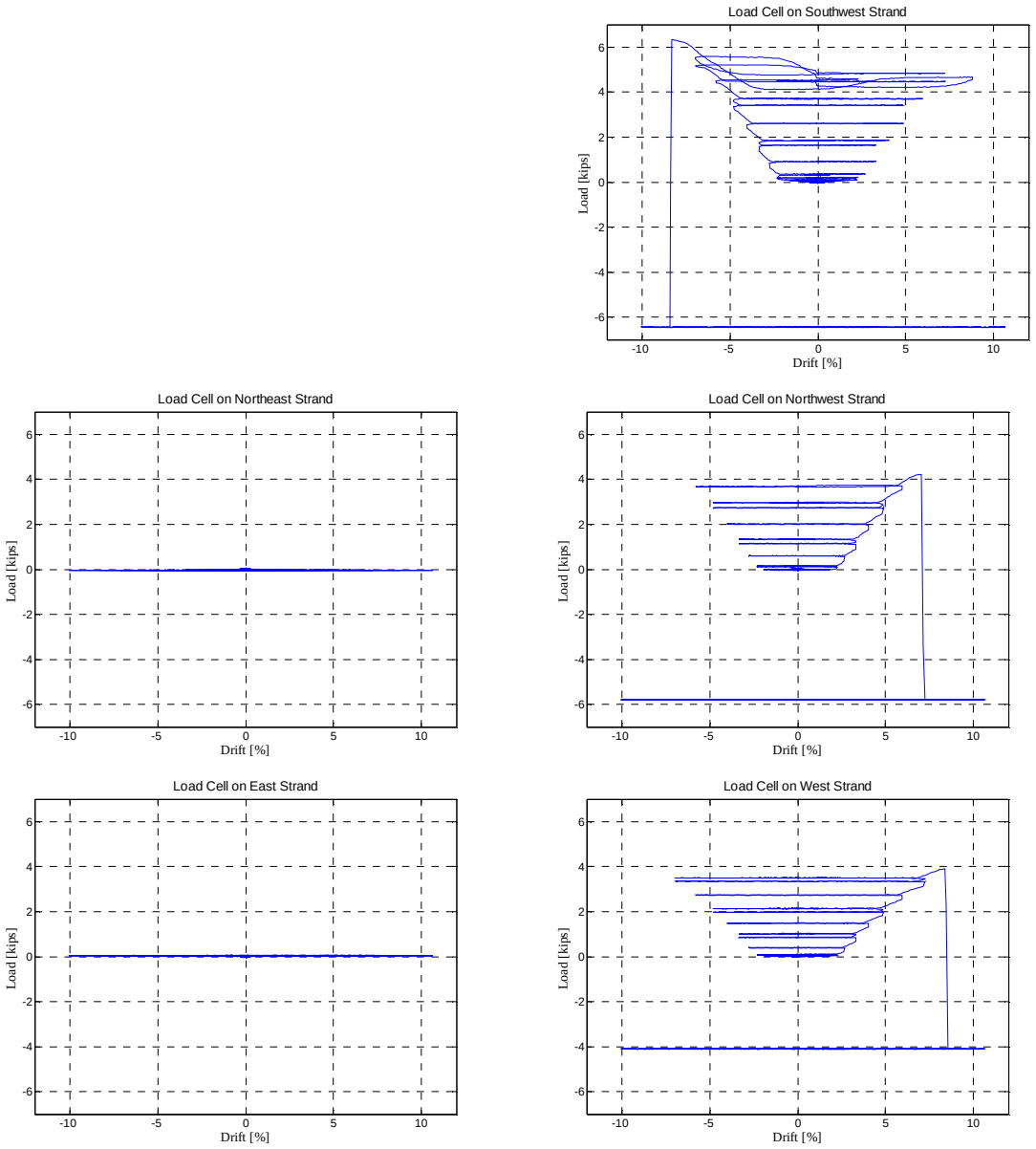

Figure 5.41 Load vs. drift on strand load cells for specimen PreT-SF-ROCK-HyFRC.

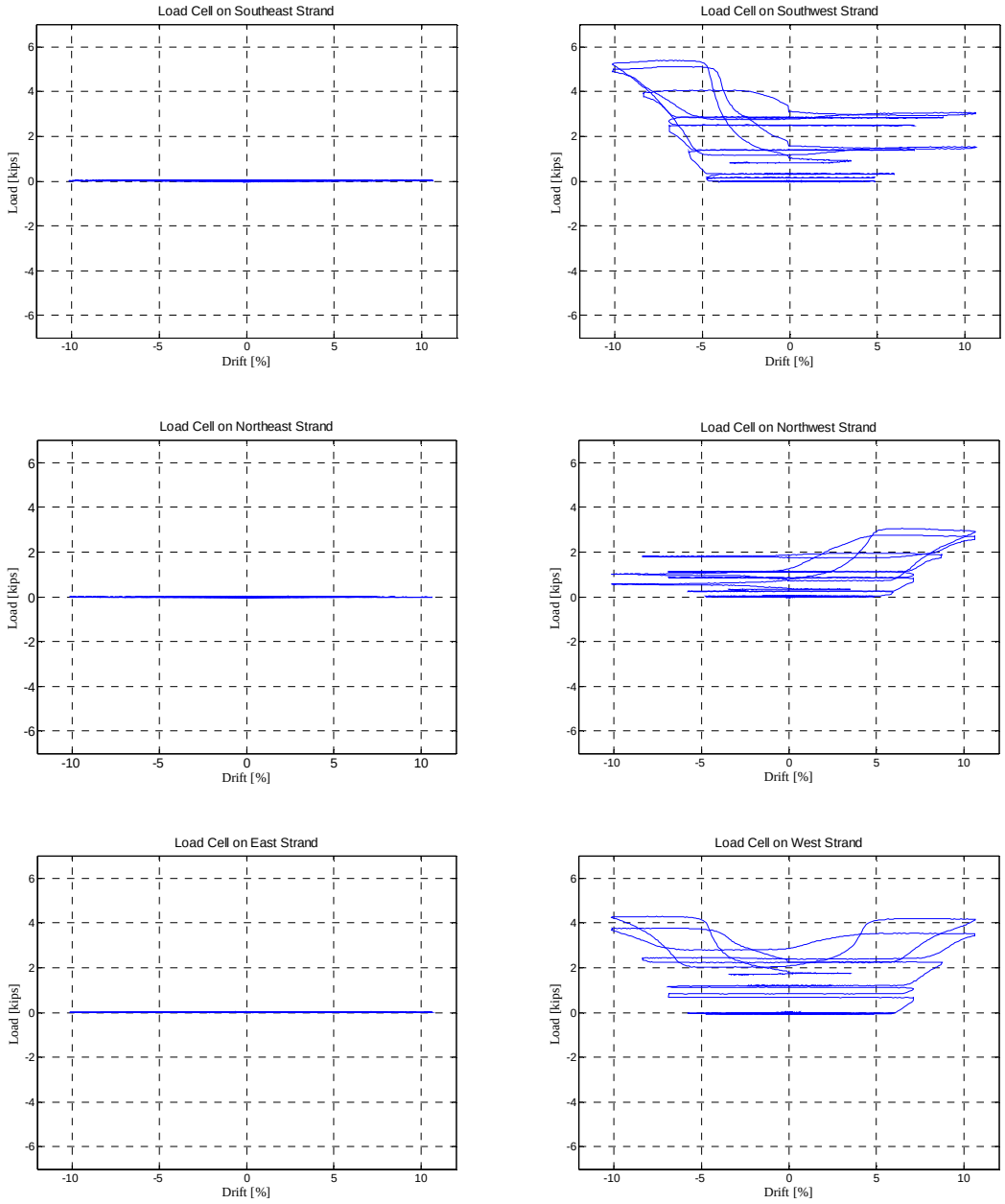

Figure 5.42 Load vs. drift on strand load cells for specimen PreT-SF-ROCK.

The plots above show that some slip occurred in six of the eleven strands containing functioning load cells. Three of the strands that slipped also fractured, considering the drastic loss of load these strands experienced almost instantaneously. The three slipped strands, all located on specimen PreT-SF-ROCK, began losing load at approximately 5% drift and continued to lose load the remainder of the test. The maximum measured load loss at the load cell (5.4 kips) occurred on the southwest strand of specimen PreT-SF-ROCK.

Prior to losing their entire load, the strain gauges on the three fractured strands on Specimen PreT-SF-ROCK-HyFRC detected an increase in strain. Researchers expected this behavior because, prior to fracture, the strand's experience some slip.

Since no slip or fracture occurred before 5% drift in the specimen, it is likely that the anchorage in the prototype would be adequate. After all, the strand diameter in the full-scale column would be proportionally smaller than it is in these two specimens. As a result, the bond strength will be higher, further reducing the chance of slippage. The bond strength in relation to ACI requirements is discussed further in Section 7.6 of the Comparison with Calculations Chapter.

5.10 AXIAL ELONGATION

Researchers estimated the column's axial elongation using the Optotrac system measures, combined with Equation 5.7:

(5.7)

where δ is the axial elongation at a specified column height, L_o is the initial length between two LED chord lines at their centers, and L_i is the changed length between two LED chord lines at their centers during loading. Figure 5.43 graphically depicts these variables. Figures 5.44 and 5.45 show the axial elongation of both columns.

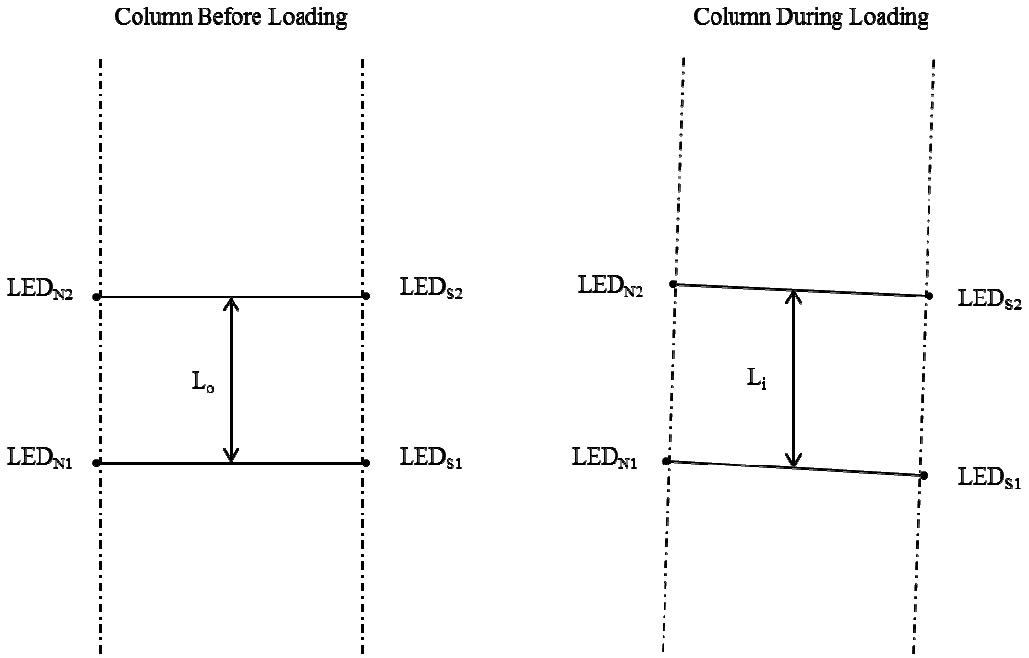

Figure 5.43 Definitions of variables for Equation 5.7.

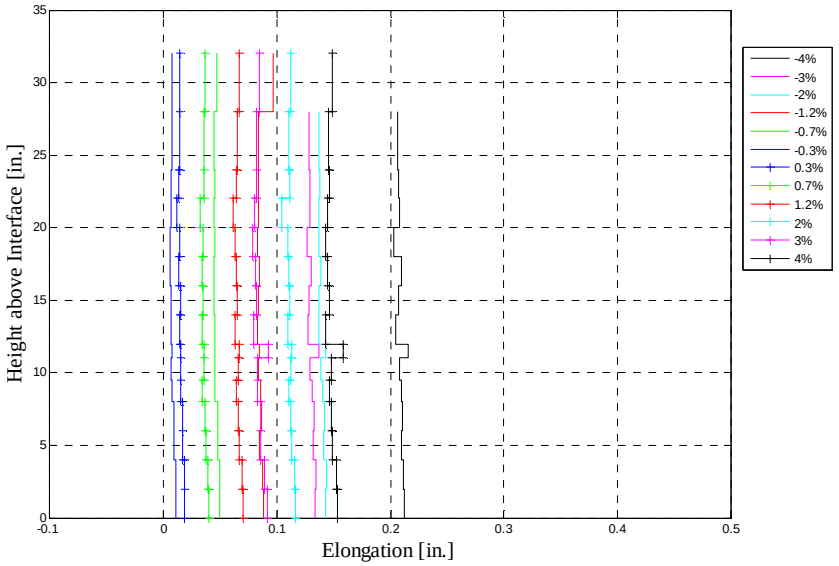

Figure 5.44 Axial elongation in PreT-SF-ROCK-HyFRC.

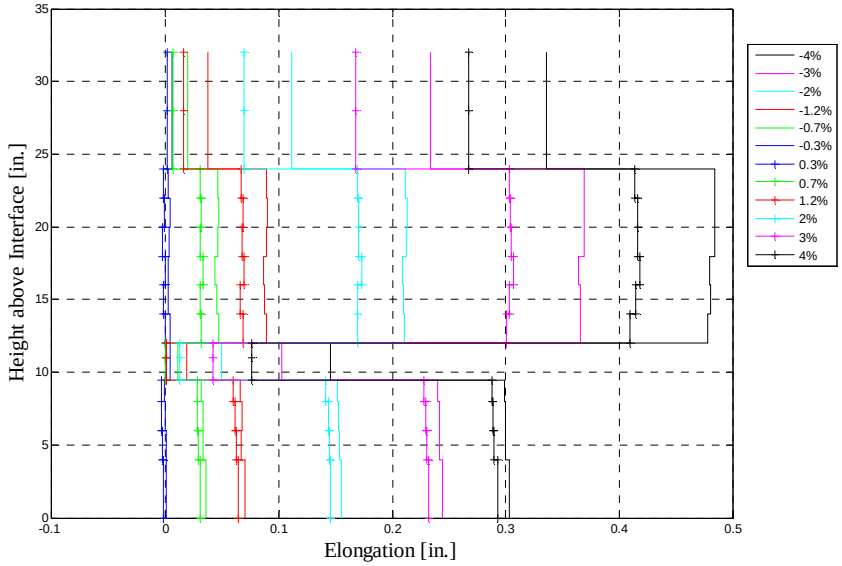

Figure 5.45 Axial elongation in PreT-SF-ROCK.

The axial elongation plot of PreT-SF-ROCK-HyFRC shows behavior that is consistent with researcher's expectations. PreT-SF-ROCK-HyFRC appears to have elongated as it cycled back and forth. The majority of the elongation was concentrated at the base of the column, with a minor blip of elongation change above the steel shoe. This behavior was consistent with the concept of a small amount of rubble in the crack at the base of the column that would inhibit perfect crack closure.

The axial elongation plot of PreT-SF-ROCK shows a different behavior. While a good portion of the axial strain occurs at interface, there is also a sizeable amount of axial change at 12” and 24” above interface. Researchers are unsure what caused this discrepancy as the Optotrac data yielded reasonable results for both rotation and curvature. The inconsistency, however, appears at only two locations. The other data points reflect an axial elongation similar to that of specimen PreT-SF-ROCK-HyFRC. As PreT-SF-ROCK cycled back and forth, the specimen appeared to elongate at its base.

6 Comparison with Previous Tests

This chapter analyzes the measured responses of specimens PreT-SF-ROCK-HyFRC and PreT-SF-ROCK and compares them with the responses of columns tested by Finnsson et al. (2013) and Davis et al. (2011). These previous tests both contained the same quantity of unbonded prestressing strands and longitudinal reinforcement, and had the same cross-sectional dimensions. The specimen constructed by Finnsson had HyFRC in the plastic hinge region above and below interface, whereas the Davis specimen was constructed with conventional concrete throughout. Neither Finnsson's nor Davis subassemblies had a steel shoe.

6.1 PEAK STRENGTH AND STRENGTH DEGRADATION

The envelope to the cyclic moment-drift curves provides a compact measure of column resistance. Figure 6.1 shows the moment envelopes for the positive and negative peaks of PreT-SF-ROCK-HyFRC, PreT-SF-ROCK, PreT-SF-HyFRC and PreT-SF-CONC. The moment envelopes are similar for the two rocking specimens. The measured moment for the PreT-SF-ROCK-HyFRC specimen was slightly larger in the positive direction but nearly identical in the negative direction up to a drift ratio of approximately -7%.

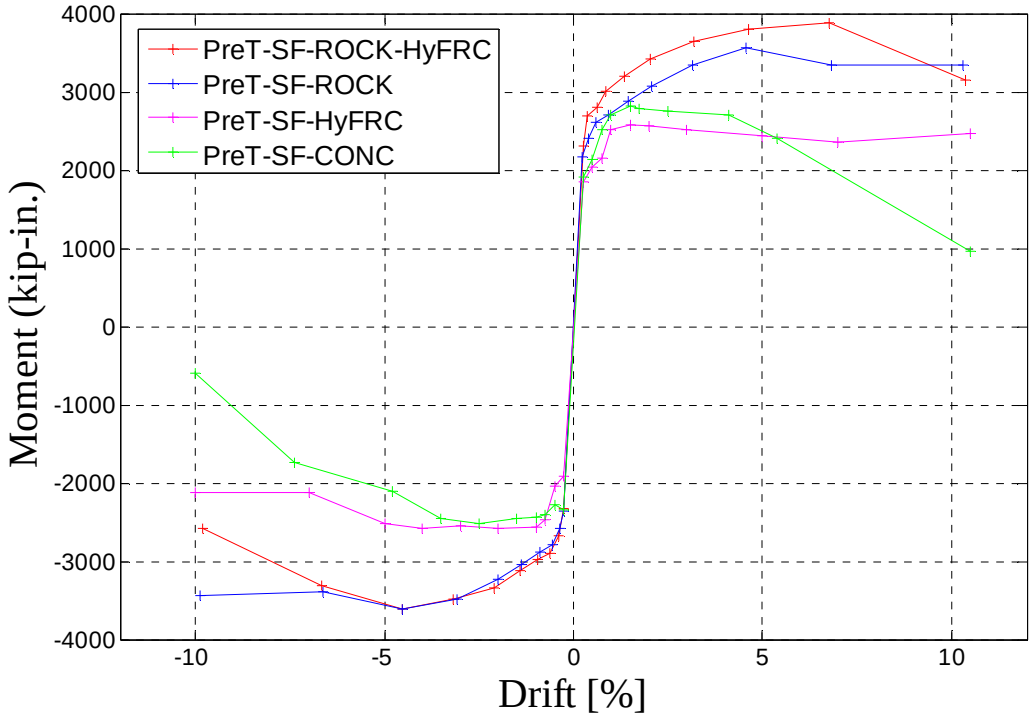

Figure 6.1 Moment vs. drift envelopes.

Despite having the same cross-sectional area of steel bridging the crack plane, the moment capacities of the two rocking specimens were significantly higher than those of the specimens tested by Finnsson et al. (2013) and Davis et al. (2011). The moment capacities of the columns in the two previous studies fell within a range of 2533-3083 kip-in. In comparison, the PreT-SF-ROCK-HyFRC and PreT-SF-ROCK's maximum moments exceeded the largest value (3093 k-in.) by 20.6% and 17.3%, respectively. It is likely that this increased moment capacity resulted from the added confinement provided by the steel shoe, which caused the center of the compression face to shift nearer to the column's edge, creating a larger lever arm.

Figure 6.2 shows the effective force envelopes, normalized by the peak effective force for all four columns. The normalized envelopes are convenient for evaluating strength degradation. The strength of the two rocking columns degraded little. To the contrary, the two columns continued to gain strength until they reached a drift ratio of approximately 5%. At the highest drift ratios (~10%) the strength of PreT-SF-ROCK degraded less than that of PreT-SF-ROCK-HyFRC in both the positive and negative directions. This difference may have been the result of the fracture of strands in specimen PreT-SF-ROCK-HyFRC (starting at a drift ratio of 7.3%) that did not occur in PreT-SF-ROCK. It is possible that the dowel bar placed in the center of the prestressing strand pattern in Specimen PreT-SF-ROCK-HyFRC caused three strands to kink and then fracture. Regardless of these small differences, both rocking specimens retained over 80% of their peak strength with the exception of specimen PreT-SF-ROCK-HyFRC in the negative direction, whose strength had decayed to 71% of its peak strength.

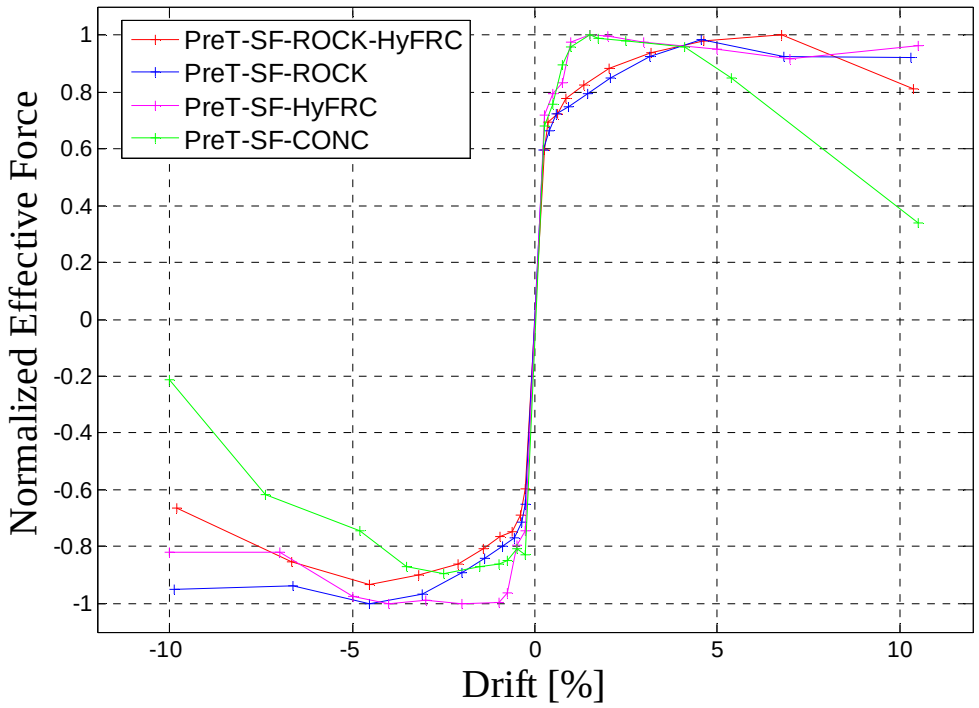

Figure 6.2 Normalized strength degradation comparisons.

The specimens without the rocking detail (PreT-SF-HyFRC and PreT-SF-CONC) reached their peak strength at approximately ±2% drift while specimens PreT-SF-ROCK-HyFRC and PreT-SF-ROCK reached their peak strength at approximately ±5% drift. This difference is likely the result of the steel shoe feature. In the previous specimens, a steel shoe did not confine the columns at interface, resulting in the concrete crushing in the plastic hinge region. In PreT-SF-ROCK-HyFRC and PreT-SF-ROCK, the confinement of the steel shoe prevented crushing and allowed the concrete to withstand more compressive stress as the columns underwent higher drift levels.

With the exception of Davis' column, the other three columns retained the majority of their strength even at extreme drift levels. Specimen PreT-SF-CONC retained its peak strength only until approximately ±4% drift. Afterwards, however, PreT-SF-CONC experienced a sharp loss in strength. Specimen PreT-SF-ROCK-HyFRC, on the other hand, retained its strength until approximately 10% where it decreased roughly 20%, a behavior likely caused by the fracture of the prestressing strands. Specimens PreT-SF-ROCK and PreT-SF-HyFRC maintained their strength even better, maintaining their strength past 10%. In the positive direction, the strength retention was nearly identical whereas in the negative direction PreT-SF-ROCK retained slightly more strength than PreT-SF-HyFRC. These envelopes show that the rocking column provides as much ductility as the HyFRC column in Finnsson's experiment. Furthermore, these envelopes show that the absence of HyFRC in the rocking column tested here did not adversely affect ductility.

Researchers designed all of the compared columns above for use in bridge systems. In such systems, the design-level earthquakes would cause drift ratios in the range of 1-2% whereas the maximum expected earthquake might induce drift ratios of maybe 3%. In all circumstances, the four above columns would not undergo any strength loss. If the columns experienced drift higher than 4%, PreT-SF-CONC would likely significantly lose strength but the remaining three columns would not.

6.2 ENERGY DISSIPATION

Structures in earthquake-prone regions dissipate energy when they undergo cyclic, inelastic deformations. Researchers calculated the energy dissipation for both columns (which corresponds to the area enclosed by each force-displacement loading cycle). Figure 6.3 shows the energy dissipated in each cycle while Figure 6.4 shows the cumulative energy dissipation throughout the whole test for both PreT-SF-ROCK-HyFRC and PreT-SF-ROCK.

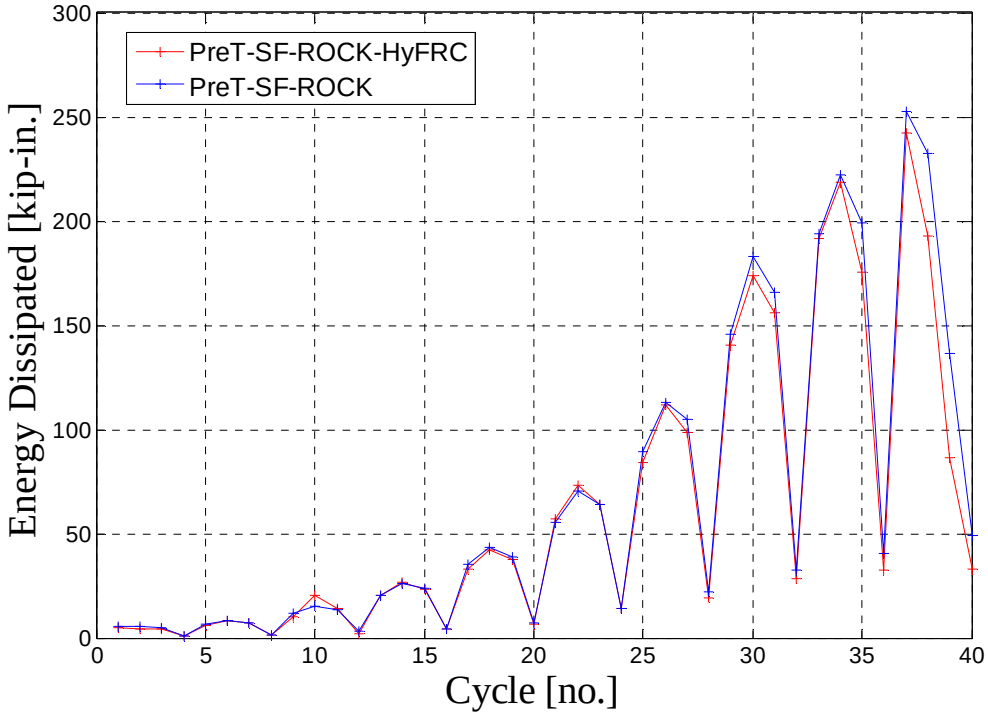

Figure 6.3 **Energy dissipation per cycle.**

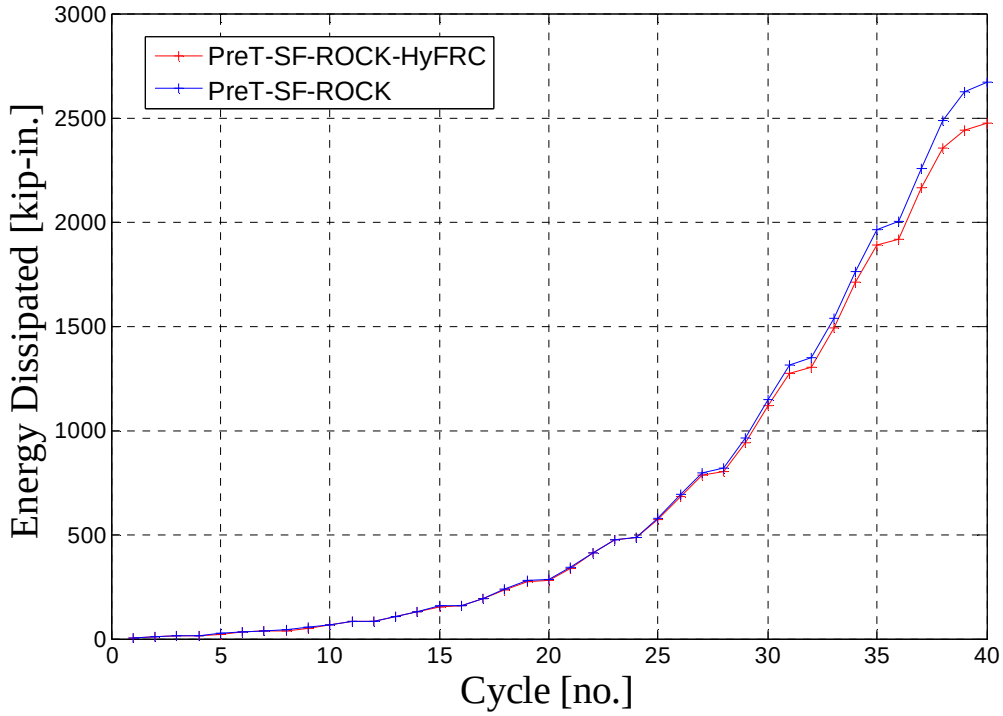

Figure 6.4 **Cumulative dissipated energy history.**

As shown in Figure 6.3, the energy dissipation for each set of cycles followed the same pattern: the second cycle dissipated the most energy while the fourth cycle dissipated the least. This pattern is the result of the imposed deformation history, which had a displacement ratio of 1.0, 1.2, 1.2 and 0.4. The fourth cycle in each set was small in comparison to the others. As a result, it is not surprising that this cycle dissipated the least energy in each set. While the third cycle and second cycle had the same loading ratio, the third cycle consistently dissipated less energy than did the second. This behavior is likely because the second cycle caused some damage.

The two plots above show that the PreT-SF-ROCK-HyFRC and PreT-SF-ROCK specimens dissipated nearly exactly the same energy. This similarity was expected, because bar yielding is the primary contributor to this performance parameter. Therefore, the inclusion or absence of HyFRC should make little difference.

The only other difference between the two columns was the inclusion of the dowel bar in PreT-SF-ROCK-HyFRC. The dowel bar should not contribute to the column's energy dissipation either because it was placed in such a way (using the welded cup) to allow rotation. If the dowel bar had deformed inelastically, then it would have increased the energy dissipation. Since PreT-SF-ROCK-HyFRC dissipated slightly less cumulative energy (7.4%) than PreT-SF-ROCK did, it appears likely that the dowel bar did not deform inelastically.

Researchers also compared the energy dissipated in PreT-SF-ROCK-HyFRC and PreT-SF-ROCK to that of specimens PreT-SF-HyFRC and PreT-SF-CONC. Researchers normalized the energy dissipated in all of the columns using a method found in Pang et al. (2008). In this method, the cumulative dissipated energy per cycle was divided by the area of a rectangle defined by the maximum (F_{max}) and minimum forces (F_{min}) for the entire test, and the maximum ($\Delta_{max(i)}$) and minimum displacements ($\Delta_{min(i)}$). Figure 6.5 depicts this normalization technique while Figure 6.5 shows the dissipated energy comparison of all four specimens.

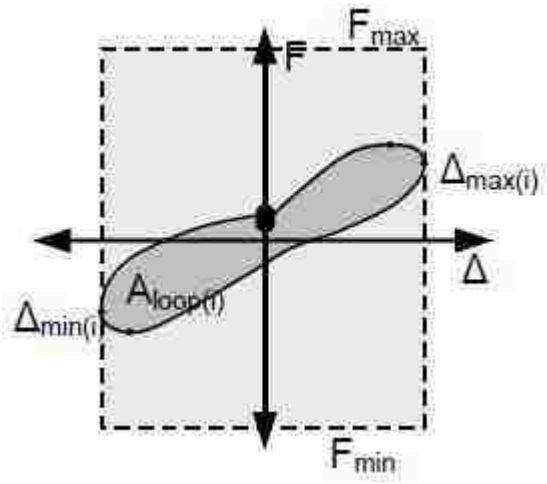

Figure 6.5 Normalization method for energy dissipation, Pang et al. (2008).

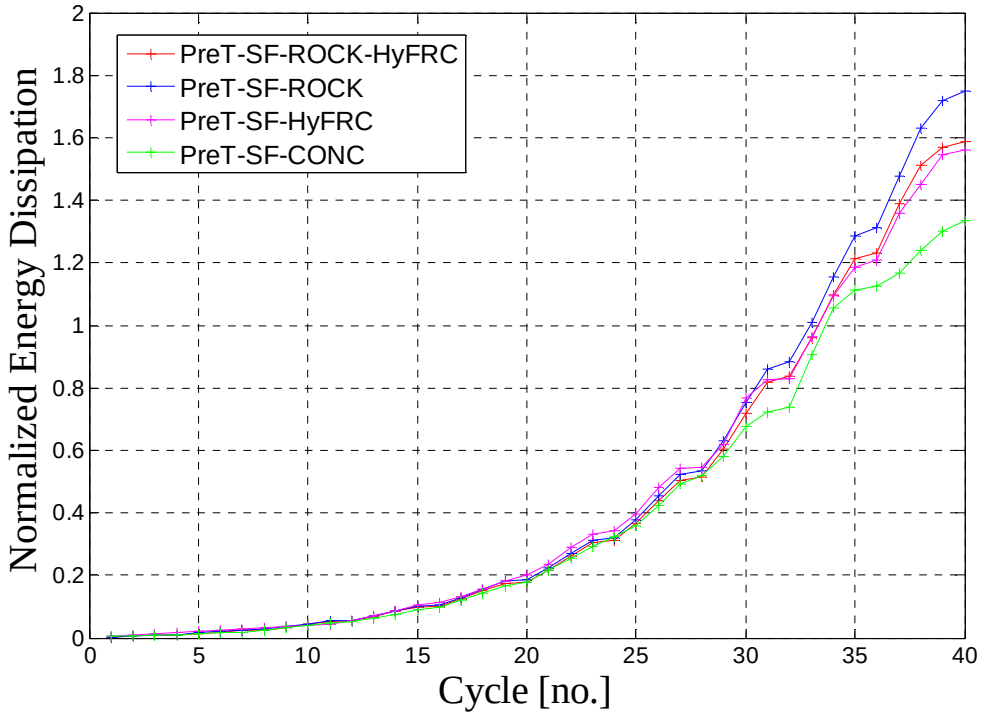

Figure 6.6 Comparison of normalized cumulative dissipated energy.

The four specimens showed similar energy dissipation characteristics until approximately Cycle 35, at which point Specimen PreT-SF-CONC began to dissipate less energy, and Specimen PreT-SF-ROCK began to dissipate more energy than the others. Specimens PreT-SF-ROCK-HyFRC and PreT-SF-HyFRC dissipated a similar amount of energy throughout the entire test. However, even as the specimens deviated at later cycles, the highest normalized energy dissipation (PreT-SF-ROCK) and the lowest normalized energy dissipation (PreT-SF-CONC) differed by a maximum of only 24.0%. The relatively close energy dissipation results make sense considering the fact that all four specimens contained prestressing. The prestressing re-centers the column, creating a pinching effect in the moment-drift response (demonstrated by Figures 5.5 and 5.6), which reduces the area enclosed by each force-displacement cycle.

6.3 EQUIVALENT VISCOUS DAMPING

Equivalent Viscous Damping (EVD) is a parameter closely related to energy dissipation. Researchers determined the EVD of each specimen using Equation 6.1:

$$\zeta = \frac{2}{\pi} \cdot \frac{A_{loop}}{A_{box}} \tag{6.1}$$

where A_{loop} is the area enclosed by each loading cycle and A_{box} is the area enclosed by the rectangles circumscribing each loading cycle. Figure 6.7 compares all four specimens' EVD with respect to load cycle, and Figure 6.8 compares the specimens' EVD with respect to drift ratio. In the plots below, researchers only calculated the EVD for the first cycle of each set.

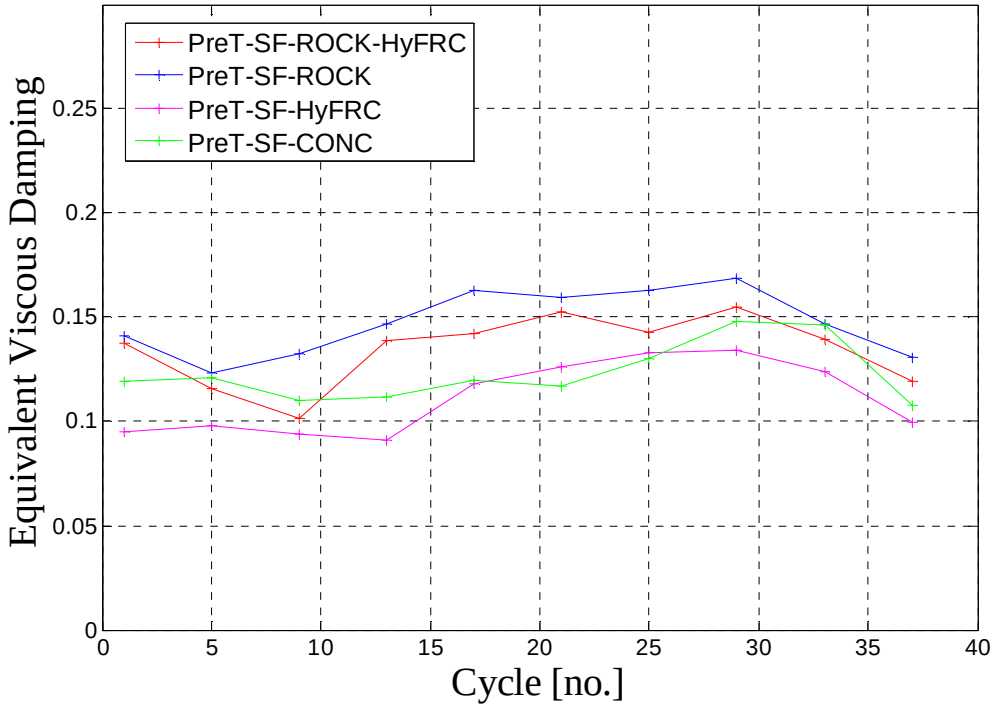

Figure 6.7 **Equivalent viscous damping versus cycle number.**

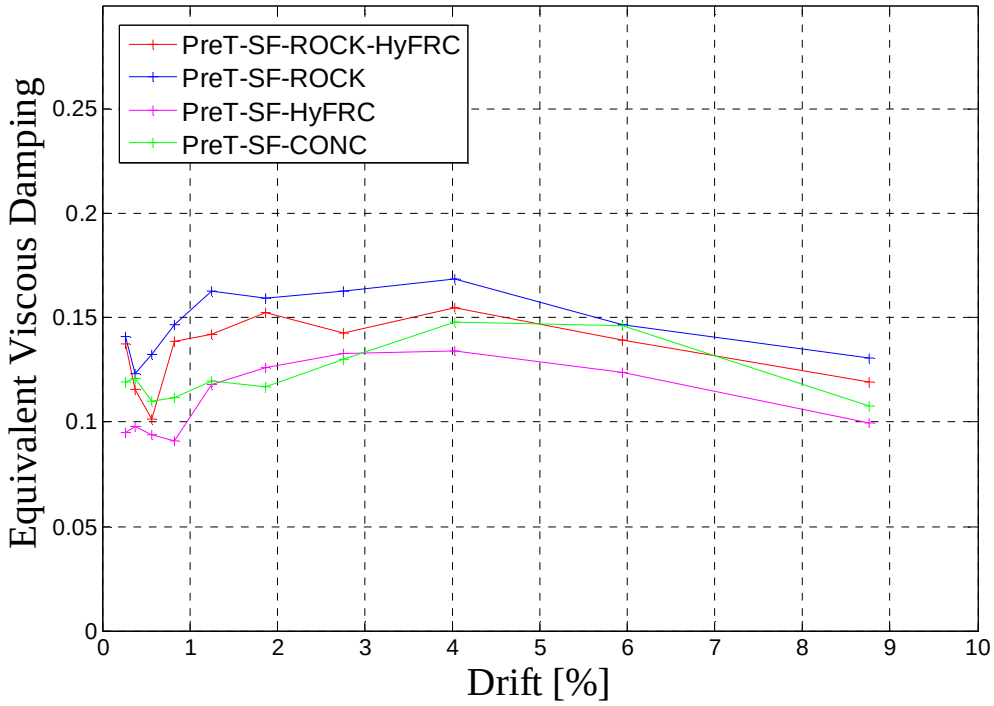

Figure 6.8 **Equivalent viscous damping versus drift ratio.**

The calculated Equivalent Viscous Damping was similar amongst all four specimens. Specimens PreT-SF-ROCK-HyFRC and PreT-SF-ROCK have slightly higher EVD factors until roughly 5% drift, at which point their EVDs became nearly identical to those of Specimen PreT-SF-CONC. Specimen PreT-SF-HyFRC consistently had a lower EVD than the other three specimens. These differences are very small:all of the specimens had an EVD in the range of 10-15%.

6.4 RE-CENTERING OF COLUMNS

6.4.1 Re-Centering Ratio

Hieber et al. (2005) developed a method for characterizing a system's tendency to re-center. The method calculates the ratio between the nominal restoring moments (cause by axial load and prestressing strands) and the resisting moments (provided by the longitudinal reinforcement). Figure 6.9 shows these forces in relation to the column.

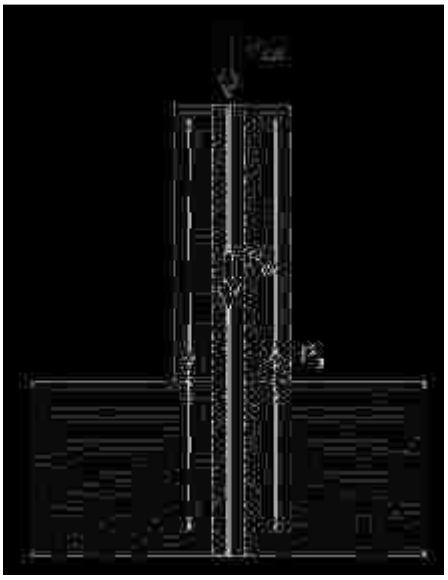

Figure 6.9 Forces used to calculate the re-centering ratio, Hieber et al. (2005).

Summing the moment caused by these two sets of forces about the centroid of the compression block yields the re-centering and resisting moments. The equation that calculates the resisting moment assumes that the longitudinal reinforcement (mild steel) is in tension in the unloaded condition. The strain profiles in Section 5.6.1 are consistent with this assumption.

$$M_{re-centering} = (P_{col} + F_{pt}) \cdot \alpha D \tag{6.2}$$

$$M_{resisting} = F_s \cdot \alpha D \tag{6.3}$$

The re-centering ratio, λ_{re}, is the ratio of the two moments calculated at zero drift after peak loading. A ratio λ_{re}>1.0 implies that the column will re-center.

$$\lambda_{re} = \frac{M_{re-centering}}{M_{resisting}} = \frac{P_{col} + P_{pt}}{P_s} = \frac{P_{col} + A_p \cdot f_{p0}}{A_s \cdot f_y} \tag{6.4}$$

Specimens PreT-SF-ROCK and PreT-SF-ROCK-HyFRC had the same applied axial load, cross-sectional area of strand and longitudinal reinforcement, and initial strand stress. As a result, both specimens had a design re-centering ratio of 3.5 (based on nominal properties) and an actual re-centering ratio of 3.1 (based on actual properties). The two ratios differ because the longitudinal reinforcement's yield stress exceeded its nominal yield stress (Section 5.1.3).

6.4.2 Normalized Cross-over Displacement

The Normalized Crossover Displacement (NCOD), plotted in Figure 6.10, is a parameter that measures a column's tendency to re-center itself after cyclic loading. Haraldsson et al. (2011) defines the crossover displacement as the displacement at which the effective force returns to zero after reaching a larger displacement. To normalize this value, the range of crossover displacements was divided by the range of peak displacements. Under this definition, a NCOD value of zero corresponds to perfect re-centering while a NCOD value of one corresponds to no re-centering. Figure 6.11 compares the re-centering ratios of the four specimens. To avoid clutter, this plot only includes points from the first and second cycles of each set.

$$\text{Normalized Crossover Displacement} = \frac{\Delta_{cross1} - \Delta_{cross2}}{\Delta_{peak1} - \Delta_{peak2}} \tag{6.5}$$

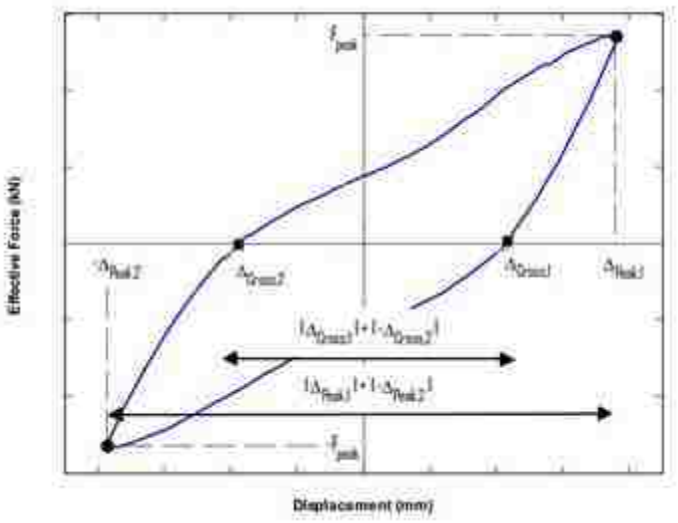

Figure 6.10 Definition of the crossover displacement, Haraldsson et al. (2011).

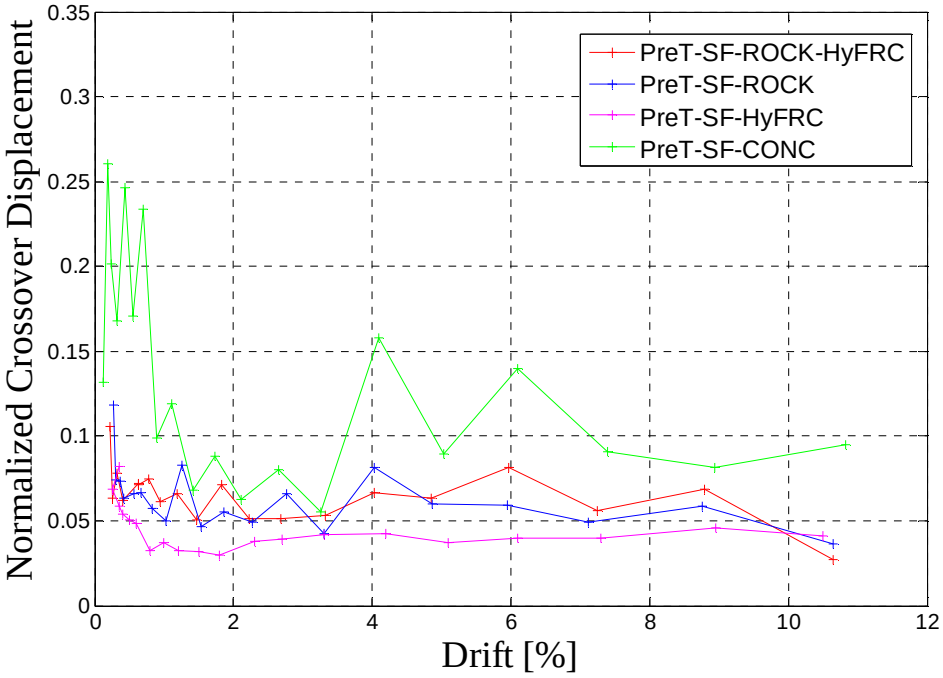

Figure 6.11 Comparison of normalized crossover displacement.

The NCOD values at small drifts are likely unreliable for two reasons. First, at low drifts none of the columns have experienced significant yielding, allowing the friction between the PTFE plate and stainless steel channel in the test rig to have a greater influence. Secondly, the residual displacements are so small that even a slight variation would reflect large differences in NCOD values. Researchers

Specimens PreT-SF-ROCK-HyFRC and PreT-SF-ROCK had nearly identical NCOD values, remaining within a range of approximately 5-8%. This suggests that added complexity of specimen PreT-SF-ROCK-HyFRC would not improve re-centering performance. Specimen PreT-SF-ROCK-HyFRC included a dowel bar to reduce any sliding that might have occurred in PreT-SF-ROCK; however, specimen PreT-SF-ROCK does not appear to have had larger residual displacements than PreT-SF-ROCK-HyFRC.

Specimen PreT-SF-CONC had the highest NCOD values, increasing markedly after 3.5% drift. The gradual increase is likely a caused by the column's degradation, which was accelerated relative to the other three specimens, since it did not include HyFRC or the steel shoe rocking feature.

Specimen PreT-SF-HyFRC displayed slightly smaller NCOD values to the two specimens in this thesis. This suggests that HyFRC alone provides similar re-centering capability as that of the steel shoe feature if not minimally better. Furthermore, including HyFRC in the steel shoe had little to no effect in terms of re-centering.

7 Comparison with Calculated Response

This chapter compares the measured and observed specimen behavior with analytical estimates.

7.1 COLUMN STIFFNESS

Researchers calculated the columns' secant stiffness at first yield using Eq. (7.1)

$$\text{Initial Secant Stiffness} = \frac{F_{eff,y}}{\Delta_y} \tag{7.1}$$

In Eq. (7-1), $F_{eff,y}$ is the measured lateral force at first yield and Δ_y is the corresponding displacement at first yield. Researchers defined the yield point, as prescribed by Elwood and Eberhard (2009), as the point where the longitudinal reinforcement first yielded in tension or the concrete reached a strain of 0.002, whichever occurred first. Table 7.1 shows the initial secant stiffness of the four columns in both the North and South directions. The secant stiffness of specimen PreT-SF-ROCK-HyFRC in the South direction was estimated, because no strain gauges functioned on the north bar at the interface, the location of highest strain. Without such measurements, researchers could not determine an exact Δ_y, instead they used moment-curvature analysis to estimate a yield force and then found the displacement at which that force first occurred

Table 7.1 Column secant stiffness at first yield.

Specimen	North Direction Stiffness [kip/in.]	South Direction Stiffness [kip/in.]	Average Stiffness [kip/in.]
PreT-SF-ROCK-HyFRC	188	212*	200
PreT-SF-ROCK	220	233	227
PreT-SF-HyFRC	128	116	122
PreT-SF-CONC	180	175	178

***Note= values with an asterisk used moment-curvature analysis to estimate the displacement at first yield since strain measurements were not available.**

The columns' modulus of rigidity was then calculated as follows:

$$EI_{eff,meas} = \frac{F_{eff,y} \cdot l^3}{3 \cdot \Delta_y} \tag{7.2}$$

where $F_{eff,y}$ is the effective force at yield, l is the cantilever length, and Δ_y is the corresponding displacement at first yield. These values were then compared to the recommendations of Elwood and Eberhard (2009), repeated in Equation 7.3:

$$\frac{EI_{eff,calc}}{EI_g} = \frac{0.45 + 2.5 \cdot \frac{P}{A_g \cdot f'_c}}{1 + 110 \cdot \frac{d_b}{D} \cdot \frac{D}{a}} \tag{7.3}$$

In Equation 7.3, P is the column's axial load, A_g is the column's cross-sectional area, f'_c is the concrete compressive strength, d_b is the bar diameter, ais the cantilever length, and D is the column diameter. For the purpose of this equation, the column's axial load was taken as the vertical load applied by the Baldwin plus the initial restoring force in the prestressing strands. Using the initial force in the strands is not exact because the force in the prestressing strands increases as the column displaces; however, the column displacement at yield is so small that the change in the axial load was negligible. Table 7.2 compares the measured and calculated moduli of rigidity of the four columns. The measured stiffnesses were lower than the calculated stiffnesses by 2-25%.

Table 7.2 Comparison of measured and calculated EI.

Specimen	$EI_{eff,meas}/EI_g$ [kip-in^2]	$EI_{eff,calc}/EI_g$ [kip-in^2]	Calc/measured]
PreT-SF-ROCK-HyFRC	0.27	0.33	1.22
PreT-SF-ROCK	0.32	0.33	1.03
PreT-SF-HyFRC	0.30	0.34	1.13
PreT-SF-CONC	0.31	0.39	1.26

7.2 FLEXURAL STRENGTH OF COLUMNS

Researchers calculated the flexural strength of the columns and compared the expected moments to those observed during the tests. To calculate the moments, researchers used a moment-curvature program and sectional analysis. The prestressing strands' modulus of elasticity was manually reduced by a factor of three to simulate the unbonded region. Researchers used a Kent-Park model for the concrete and a tri-linear steel model for the longitudinal reinforcement. The points along the steel model were defined by the reinforcement's modulus of elasticity, yield stress, strain hardening onset strain, ultimate strain and ultimate strength.

Researchers accounted for the steel shoe feature by treating the concrete as heavily confined using a model created by Galeota et al. (1992). This model (Equation 7.4) required researchers to convert the thickness of the steel shoe wall to an equivalent spiral. They did so by setting $A_s/s=t_{wall}=0.25$".

$$f'_{cc} = f'_c + 3.25\left(\frac{2 \cdot f_y}{d_c} \cdot \frac{A_s}{s}\right) \tag{7.4}$$

The variables of Equation 7.4 are defined as f'_{cc}=confined concrete compressive strength, f'_c=nominal concrete compressive strength, f_y=steel shoe wall tensile strength, d_c=outer diameter of steel shoe, and A_s/s=steel shoe wall thickness. According to this model, the properties of the steel shoe increase the concrete compressive strength through confinement by a factor of 1.48.

Using a moment-curvature program and a concrete compressive strength of $1.48 \cdot f'_c$, researchers estimated the columns' flexural strength to be 3302 kip-in. This value underestimates the measured flexural strength of both columns. The effect of the confinement may have been larger than an increase in strength of 48%, because the base plate was not included in the analysis. To evaluate the effect of accounting for the increased confinement, researchers conducted two additional analyses, one where confinement allowed the concrete to reach 4 times its unconfined compressive stress and a second where confinement allowed the concrete to reach 40 times its unconfined compressive stress, and compared the results. The computed values from all three analyses are presented in Table 7.3.

Table 7.3 Calculated moment and observed moment strengths

Specimen	$M_{observed}$ [k-in.]	Concrete Confinement	$M_{calculated}$ [k-in.]	$M_{calculated}/M_{observed}$
PreT-SF-ROCK-HyFRC	3885	**1.48x f'_c (Equation 6.13)**	3302	0.85
		4x f'_c	3689	0.97
		40x f'_c	3905	1.03
PreT-SF-ROCK	3731	**1.48x f'_c (Equation 6.13)**	3302	0.89
		4x f'_c	3689	0.99
		40x f'_c	3905	1.05

In both columns, the observed flexural strength lies within the narrow range of the calculated flexural strengths where the confined concrete compressive strength was taken as $4.0 \cdot f'_c$ and $40.0 \cdot f'_c$. These results suggest that a moment-curvature program using a concrete compressive strength of $4.0 \cdot f'_c$ gives a lower bound to the column's flexural strength. This is useful for future designers because it provides a means for accurately calculating the flexural strength of the rocking column.

7.3 SHEAR STRENGTH OF COLUMNS

Researchers estimated the shear strength of the columns using equations 7.5-7.7, which came from ACI 318-11.

$$V_c = 2 \cdot \left(1 + \frac{N_u}{2000 \cdot A_g}\right) \cdot \sqrt{f'_c} \cdot b_w \cdot d \qquad (7.5)$$

$$V_s = \frac{A_v \cdot f_{yt} \cdot d}{s} \quad (7.6)$$

$$V_n = V_c + V_s \quad (7.7)$$

In the above equations, V_n is the nominal shear strength, V_c is the concrete contribution, V_s is the steel contribution, N_u is the axial load, A_g is the gross cross-sectional area, f'_c is the concrete compressive strength, b_w is the column diameter, d is the depth from the extreme compression face to the centroid of the tensile steel, A_v is the cross-sectional area of the spiral reinforcement, f_{yt} is the spiral yield strength, and s is the spiral spacing. N_u was taken as the applied axial load from the Baldwin plus the force in the prestressing strands.

Table 7.4 shows the nominal shear strengths of the two columns at onset and at the point where the strands yielded. In all cases, $V_{meas}/V_n<0.35$ because the load was limited by the column's flexural strength, so only about one third of the calculated shear strength capacity was needed. The result is consistent with the fact that no shear damage was observed in any of the columns.

Table 7.4 Results for shear strength calculations.

	V_c [kips]	V_s [kips]	V_n [kips]	V_{meas} [kips]	V_{meas}/V_n
PreT-SF-ROCK-HyFRC –initial	102.0	89.4	191.4	64.7	33.8%
PreT-SF-ROCK-HyFRC –yield	107.4		196.8		32.9%
PreT-SF-ROCK – initial	102.4	89.4	191.8	62.2	32.4%
PreT-SF-ROCK – yield	107.8		197.2		31.5%

7.4 DRIFT RATIO AT BAR FRACTURE

Researchers compared the drift ratio at which bar fractured occurred in the four specimens (PreT-SF-ROCK-HyFRC, PreT-SF-ROCK, PreT-SF-HyFRC, and PreT-SF-CONC) with the damage progression model proposed by Berry and Eberhard (2004 and 2005). In previous tests, researchers compared column spalling and bar buckling to Berry and Eberhard's model; however, since neither column spalling nor bar buckling occurred in PreT-SF-ROCK-HyFRC or PreT-SF-ROCK, such comparisons were not relevant. The damage model proposed by Berry and Eberhard estimates the drift value at which bar fracture occurs, as follows:

$$\frac{\Delta_{calc,bf}}{L}[\%] = 3.5 \cdot \left(1 + 150 \cdot \rho_{eff} \cdot \frac{d_b}{D}\right)\left(1 - \frac{P}{A_g \cdot f'_c}\right)\left(1 + \frac{L}{10D}\right) \quad (7.8)$$

where L is the cantilever length, d_b is the bar diameter, D is the column diameter, P is the axial load, A_g is the cross-sectional area, f'_c is the concrete compressive strength, and ρ_{eff} is a ratio

given as $\rho_s * f_{ys}/f'_c$. In this ratio, ρ_s is the transverse reinforcement ratio and f_{ys} is the transverse reinforcement's yield stress. The above model (Eq. 7.8) does not include the effects of prestressing. To accommodate this, researchers added the prestressing force to the applied axial load. Two series of comparisons were done, one with the initial force in the strands and another with the yield force. Table 7.5 shows the comparison between the predicted and observed values.

Table 7.5 Comparison between predicted and observed drift values at bar fracture

Specimen	PreT-SF-ROCK-HyFRC			PreT-SF-ROCK			PreT-SF-HyFRC	PreT-SF-CONC
Drift ratio at bar fracture [%]	Pred.	Obs.	Obs/Pred	Pred.	Obs.	Obs/Pred	Obs/Pred	Obs/Pred
Initial Force	5.24	5.96	1.14	5.26	5.94	1.13	0.77	0.77
Yield Force	5.14	5.96	1.16	5.14	5.94	1.16	0.72	0.77

The tables above show that the model by Berry and Eberhard underestimates the drift values of bar fracture for both PreT-SF-ROCK-HyFRC and PreT-SF-ROCK. This is expected because the longitudinal reinforcement is debonded 8" in both specimens and the model by Berry and Eberhard does not account for the effects of debonding. Compared with PreT-SF-HyFRC and PreT-SF-CONC, the two specimens in this thesis have delayed bar fracture—one of the goals of this design—suggesting that debonding the longitudinal reinforcement had beneficial effects. The difference between PreT-SF-ROCK-HyFRC and PreT-SF-ROCK was minimal, suggesting that HyFRC and the dowel bar do not help delay bar fracture.

7.5 COLUMN ROTATION AND VERTICAL DISPLACEMENT

The researchers sought to develop a method to relate the measured strain in the No. 4 bars to the observed column rotation. The development of an accurate methodology would be beneficial to future practice because designers could estimate the expected reinforcing strain a column would experience given an expected rotation or drift ratio. Using measured bar strains, the total bar elongation was estimated with Equation 7.9.

$$\delta = 0.5 * \left(L_u + 2 * h_B - \frac{h_B - L_u}{\varepsilon_T - \varepsilon_M} * \varepsilon_T - \frac{h_B - L_u}{\varepsilon_B - \varepsilon_M} * \varepsilon_B \right) * \varepsilon_M \tag{7.9}$$

The variables of Equation 7.9 are illustrated in Figure 7.1 and defined as:

δ=the bar's total elongation
L_u=the unbonded length of the bar

h_B=the distance from the interface to the location of the strain gauges in the bonded region.

ε_T=the strain measured from the strain gauge in the bonded region above interface

ε_B=the strain measured from the strain gauge in the bonded region below interface

ε_M=the strain measured from the strain gauge at interface

In Equation 7.9, researchers assumed that the strain was constant in the unbonded region and linearly varying in the bonded region.

Researchers could only compute the bar deformation for specimen PreT-SF-CONC-CON-RK since none of the strain gauges at interface functioned during the PreT-SF-CONC-FIB-RK test. Figure 7.2 compares the bar deformations with the expected deformations based on the rotations derived from the measurements of the curvature rod system at 2.5" above interface, and the Optotrac system at 2" above interface, and a theoretically rigid body. Since the y-intercept of the slope for the rigid body was unascertainable, it was fitted to pass through the same y-intercept of the expected deformations slope for the Optotrac rotations. This method allowed for an easy comparison of the slopes. All four slopes were calculated for the following drifts: ±0.3%, ±0.7%, and ±1.2%.

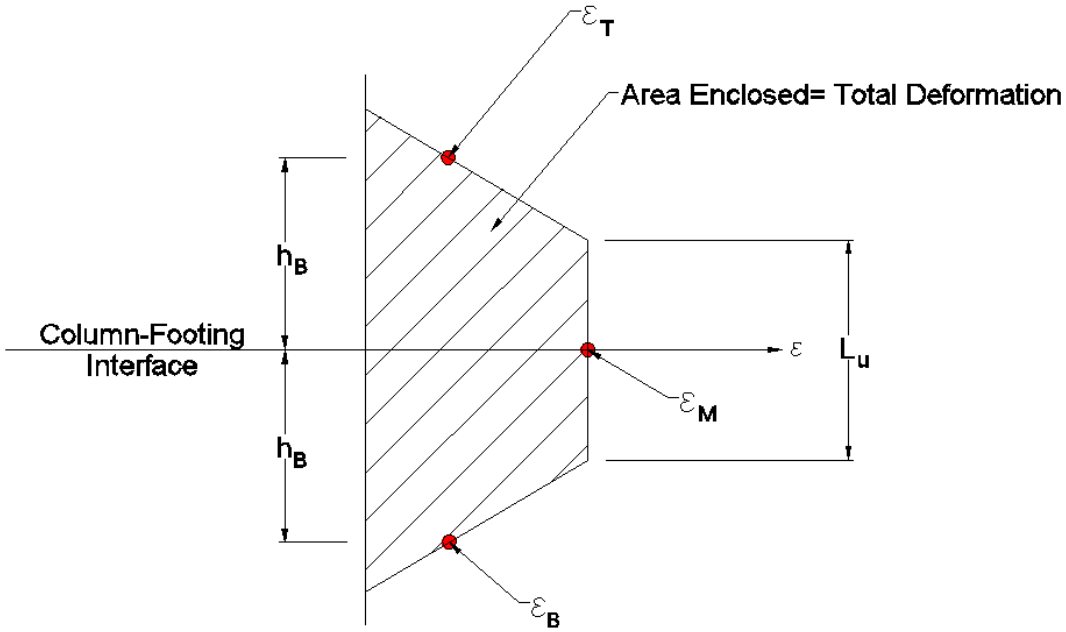

Figure 7.1 Definition of variables for Equation 7.9.

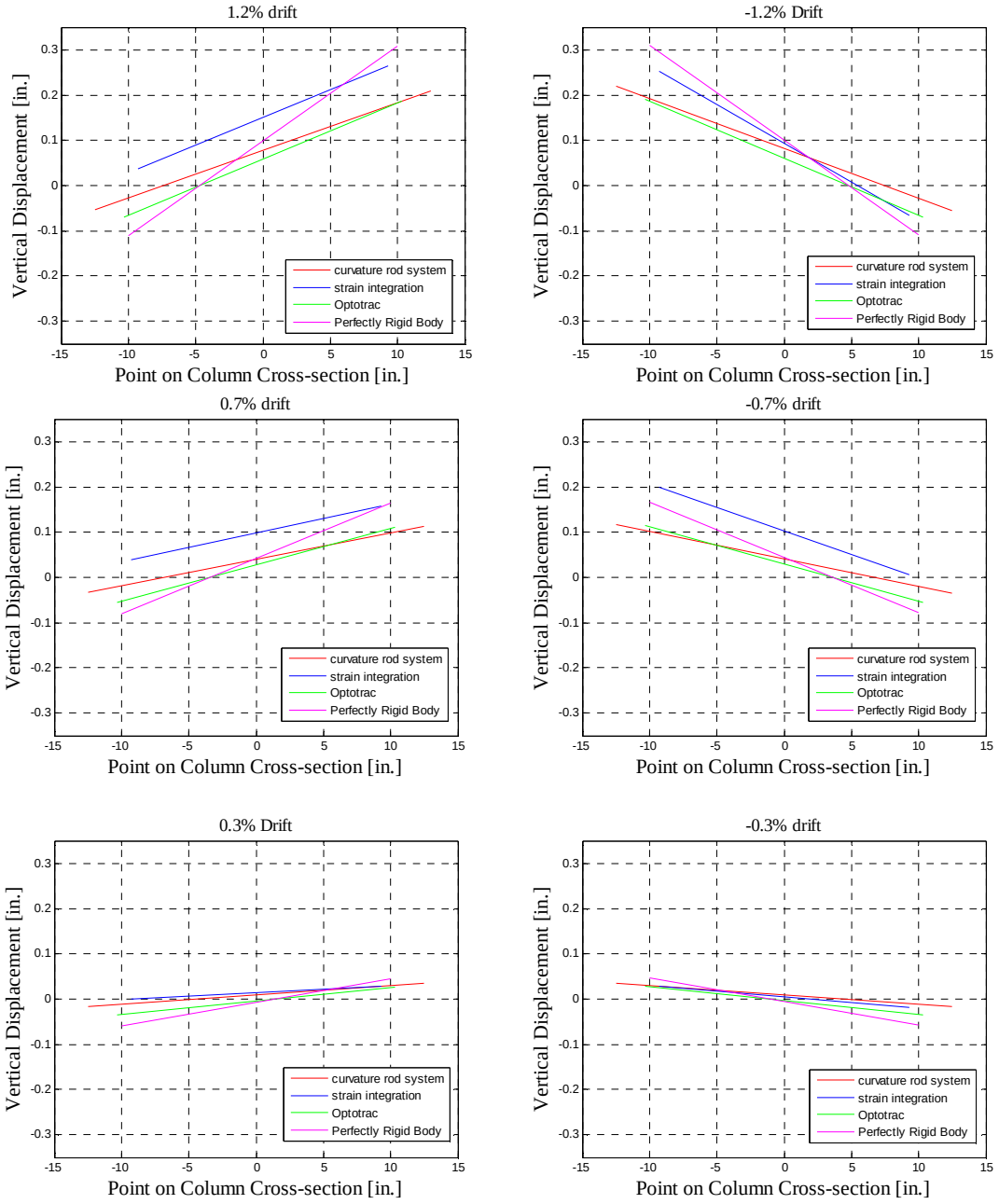

Figure 7.2 Comparison of vertical displacement and column rotation computed from different sensors.

The slopes derived from the reinforcing bar strain integration are very similar to the slopes derived from the curvature rod system and Optotrac rotations. Furthermore, these three slopes are all slightly lower than the slope of the theoretically rigid body. This result is consistent with the researchers' expectations, because while the column behaved nearly like a rigid body, some deformation nonetheless occurred at locations other than at the interface.

The change in height lines derived from the strain integration, while having similar slopes, are translated slightly upwards compared to those derived from the rotation mechanisms. This observation is more apparent at higher drift levels (±1.2% and ±0.7%)

than lower ones (±0.3%). One possible explanation for this discrepancy is that the measured strain at the interface is higher due to the method of placing the instrumentation. When researchers installed the strain gauges, the bars were prepped by grinding away some material. This reduction in material inevitably created a strain concentration at the measured location, which is not found at other locations in the unbonded region. Consequently, the real strain distribution might more closely resemble that shown in Figure 7.3. Accounting for the strain concentration would lead to a smaller predicted vertical displacement and rotation. Researchers, however, have no means of retroactively determining the extent to which this strain concentration overestimates the true strain.

While the bar strains appear to overestimate the total deformation relative to the rotation mechanisms, both methods are still reasonably close. This result suggests that designers could use anticipated drift ratios to calculate the strain demand in the reinforcing bars.

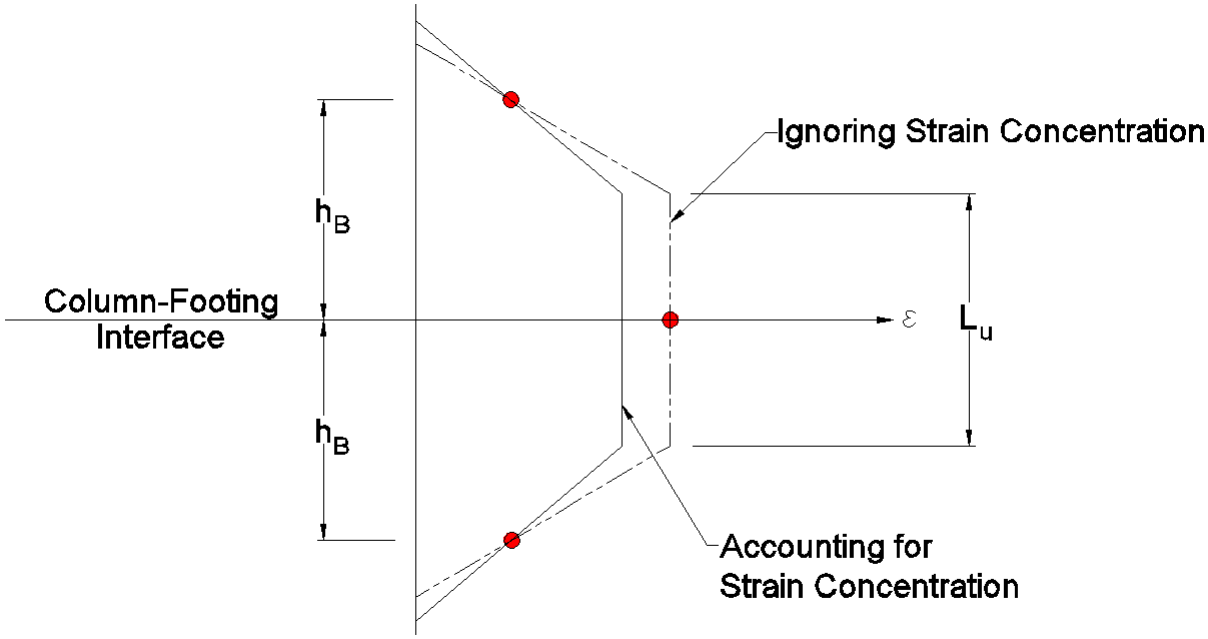

Figure 7.3 Comparison of assumed and measured bar strain concentrations.

7.6 STRAND BOND STRENGTH

Based on the drift ratio at which the load cells indicated strand slip and the strain gauge readings on the strand, researchers could compare the average bond strength between the strand and concrete with the calculated bond strength from ACI Equation 12-4:

$$L_d = \left(\frac{f_{se}}{3} + \frac{f_{ps} - f_{se}}{1}\right) * d_b \tag{7.10}$$

where L_d is the development length, f_{se} is the effective prestressing stress, f_{ps} is the maximum stress carried by the strand, and d_b is the strand diameter.

Both columns used 3/8" diameter strand. Additionally, the strands had an average effective prestressing stress of 156.9 ksi and were developed 24" into the top of the column. Given these values, the ACI Equation dictates that the bond should fail when the stress in the strands exceed 168.6 ksi. In order to carry the strands' full capacity, 250 ksi, the strands would need a development length of 56.25" (150 d_b). Table 7.6 lists the stress in each strand at first slip for each of the six strands (out of eleven) that slipped.

According to these results, the slipped strands on specimen PreT-SF-ROCK reached a stress of at least 220 ksi before any load was lost. The slipped strands on specimen PreT-SF-ROCK-HyFRC had much lower stresses; however, researchers believe that this occurrence was an anomaly. After all, the majority of the strands (8 of 11) either did not slip or slipped only after experiencing stresses greater than 220 ksi. The misaligned dowel bar is one possible reason the three strands in specimen PreT-SF-ROCK-HyFRC did slip under much lower stresses. These strands eventually fractured, unlike the other strands, so it is likely that the dowel bar caused the strands to kink, slip prematurely and ultimately fracture.

The majority of the strands exhibited bond strength that was significantly higher than that given in ACI 318-11. That behavior is attributed to the configuration. The strands were placed near the center of the column. At the bottom of the column, a significant volume of column concrete surrounded the strands. Hoop tension capacity that inhibited splitting was therefore provided by the column concrete, the column spiral and the surrounding footing concrete. At the top, the concrete surrounding the strands was confined by a significant amount of reinforcement, and by the tensioned bolts that attached the actuator to the specimen.

Table 7.6 Stress in prestressing strands at first slip

	Stress in Strand (ksi)					
Specimen	**Southeast Strand**	**Southwest Strand**	**East Strand**	**West Strand**	**Northeast Strand**	**Northwest strand**
PreT-SF-ROCK-HyFRC	**N/A**	**160* (2.25%)**	**N/A**	**120* (2.25%)**	**N/A**	**149* (1.48%)**
PreT-SF-ROCK	**N/A**	**250 (5.85%)**	**N/A**	**229 (6.23%)**	**N/A**	**220 (4.87%)**

***Note: strands that fractured are indicated with an asterisk while strands that did not slip are indicated with N/A. The number in parenthesis is the drift ratio at which first slip occurred.**

8 Summary and Conclusions

8.1 SUMMARY

This thesis describes the development and testing of two unbonded, pre-tensioned bridge column-footing subassemblies with a rocking detail. The work forms part of a larger study at the University of Washington with goals to develop a system that contains three advantages over the current conventional bridge bent design: (1) decreased on-site construction time, (2) improved re-centering capability, and (3) reduced damage due to cyclic lateral loading.

The first goal, decreased on-site construction time, is achieved through using a "wet socket" connection at the column-footing connection and a "dry socket" connection at the column-cap beam connection. The "wet socket" connection was developed and tested by Haraldsson et al. (2011) for a precast concrete column that contained no prestressing. The wet socket connection allows the column to be pre-cast in a fabrication plant and then delivered to the site. The column is then erected in the excavation, the footing steel is placed around it, and the footing concrete is cast in place. The surface of the precast column is roughened to increase the shear transfer between the column and footing. The longitudinal reinforcing bars are anchored in the column concrete using mechanical anchors, which obviate the need to bend the bars outward into the footing and facilitate transportation. Khaleghi et al. (2013) documented the use of this connection in the field. The same connection concept was used in the tests described in this thesis, but here the columns were pre-tensioned.

Davis et al. (2011) addressed the second goal (re-centering) by including prestressing strands in addition to the mild reinforcing steel. Davis' test specimens represented the top and bottom connections in a column in which the strands were bonded at the ends of the column and unbonded over the free height between the top of the footing and the underside of the cap beam. The unbonded prestressing strands were placed near the columns' centers and caused the column to re-center after the lateral load was released. The debonded region distributed the strain in the strands so that they remained elastic up to the design drift ratio. Each strand was also coated in epoxy to reduce the succeptibility to corrosion.

Davis' specimens had low residual displacements, as intended, but spalling, bar bucking and bar fracture occurred at lower drift levels than observed in comparable non-prestressed columns (e.g. Haraldsson et al., 2011). The earlier onset of damage was attributed to the added axial load caused by the prestressing strands and by the short length over which the strength of the small bars were developed.

Finnsson et al. (2013) tested two columns that were designed to delay the onset of damage through the use of ductile materials: hybrid fiber reinforced concrete (HyFRC) and stainless steel reinforcing bars. The HyFRC was placed only in the plastic hinge region, because it is more expensive than conventional concrete. Both of Finnsson's specimens contained HyFRC, but only one specimen contained stainless steel reinforcement; the other specimen used conventional "black" steel. The HyFRC delayed column spalling, but the stainless steel provided little benefit.. Bar bucking and bar fracture still occurred earlier than desired.

The two columns tested for this thesis represent a development beyond those investigated by Finnsson and Davis. They contained unbonded prestressing strands identical to those used by Davis et al. (2011) and a socket connection identical to that of Haraldsson et al. (2011), but they

used a different strategy to minimize damage. In both specimens, a steel shoe confined column concrete at the column-footing interface. It consisted of a short length of steel pipe with an annular plate welded to it. The intent was that the column would undergo rigid body rocking on the foundation, and would be protected against damage by the confining effects of the steel shoe. Above the steel shoe, the axial stress caused by the moment and vertical load would be low enough that the unconfined concrete would not spall. To further inhibit such spalling, No.6 bars were welded to the annular base-plate of the shoe and extended upward 2.15 column diameters (43”). These bars did not cross the rocking interface and so did not contribute to the flexural strength of the column.

Since the steel shoe provided such a high degree of confinement, the need for HyFRC in this region was unclear. To answer this question, one specimen contained purely conventional concrete (PreT-SF-CON-RK) while the second specimen contained a mix of conventional concrete and HyFRC (PreT-SF-FIB-RK). The region that contained HyFRC in specimen PreT-SF-FIB-RK began at the column-footing interface and extended 24” up into the column. A dowel and cup feature at the center of the column-footing interface of specimen PreT-SF-FIB-RK was also included to inhibit possible shear sliding at the column’s base. The dowel and cup system was designed so that it provided shear resistance but no bending resistance. Specimen PreT-SF-CON-RK did not have this feature.

Another feature included in both specimens described here but absent in previous specimens was the partial debonding of the mild reinforcement. In both specimens, the mild reinforcing was bonded to the concrete except at the column-footing interface where it was unbonded 4” above and 4” below. This unbonded region distributed the elongation caused over a longer length and reduced the resulting strain, consequently allowing the specimens to reach higher drifts before bar buckling and bar fracture occurred.

Once constructed, the two specimens were subjected to constant axial loading paired with cyclic transverse loading. The experimental results showed that the steel confining shoe combined with the partial debonding of mild reinforcement eliminated both column spalling and bar buckling, and delayed bar fracture. The strength of the two specimens was also higher than that of the previous pre-tensioned specimens, despite containing an identical amount of reinforcement, both prestressed and deformed bar, across the column-footing interface. This higher strength was attributed to the longer lever arm made possible by the smaller compressed area, which in turn was the result of the confining shoe.

8.2 CONCLUSIONS

8.2.1 Overall Conclusions

1. The two specimens tested here, both containing steel shoe features but one with and one without HyFRC, achieved their main design objectives of excellent re-centering behavior accompanied by low damage. The residual drift ratios were approximately 0.5% (i.e. 0.005) even after peak drift ratios of over 10%.
2. In both specimens, concrete spalling and bar buckling were eliminated by the rocking detail.
3. Debonding the reinforcing bars locally with a plastic tube at the rocking interface delayed bar fracture. The first bar fracture occurred near a drift ratio of 6%, as compared with 4% with the column-footing subassemblies tested by Finnsson et al. and Davis et al.

8.2.2 Detailed Conclusions

1. The steel shoe effectively confined the concrete at the rocking interface. It led to minimal damage, and represents a great improvement over other means to limit damage, such as the use of HyFRC alone.
2. The flexural strengths of both rocking specimens (PreT-SF-FIB-RK and PreT-SF-CON-RK) were significantly higher than the strengths of similar specimens without the steel shoe detail. The increase in strength was attributed to the longer lever arm that resulted from the smaller compression region, which was in turn caused by the higher contact stresses.
3. Both specimens also demonstrated flexural strengths within 3% of that calculated by moment curvature analysis in which the influence of the steel shoe was accounted for by changing the concrete strength to $4f'_c$.
4. The performances of both PreT-SF-FIB-RK and PreT-SF-CON-RK were nearly identical in terms of strength, re-centering and energy dissipation. This suggests that the HyFRC and dowel bar in specimen PreT-SF-FIB-RK provided negligible benefits.
5. The No. 6 reinforcing bars welded to the shoe experienced compressive stresses at the base of the shoe and tensile stresses at the top. The maximum tensile and compressive stresses lay in the range $0.25f_y$ to $0.50f_y$. This implies that they were effective in distributing the concentrated force at the interface into the concrete, which might otherwise have caused local crushing there, and in minimizing the width of the crack that inevitably started at the top of the shoe due to the discontinuity there.
6. As in previous tests, the wet socket connection performed well, and suffered no visible damage throughout the tests.
7. In both specimens, only 50% of the strands suffered from bond slip, and they slipped only after drift ratios greater than 5%. The slip was small, thanks to the back-up anchorage system that had been implemented for that purpose. The strands were larger in diameter than the model scale demanded because smaller epoxy-coated strands could not be obtained commercially. The bond demand on them was thus unduly high, and the fact that some of them slipped in the tests does not imply that they would slip in a full-scale prototype.
8. In Specimen PreT-SF-FIB-RK, the three strands that slipped also fractured. This fracture was attributed to misalignment of the dowel and cup feature, which is believed to have come into contact with the strands and kinked them when the column was at a peak drift of 7.0%. Space limitations at the center of the column meant that the strands were very close to the cup.
9. The transverse reinforcement (spiral) within the steel shoe region experienced strains no greater than 10% of the yield strain, suggesting that it is not necessary for confinement within that region.

8.3 RECOMMENDATIONS

8.3.1 Practice and Design Recommendations

1. The steel shoe feature provides enough confinement that the use of HyFRC is unnecessary, and its use is discouraged because the material is expensive, the casting procedure is difficult, and the uneven fracture pattern at the interface might have contributed to the slightly worse re-centering in specimen PreT-SF-ROCK-HyFRC .
2. The dowel and cup detail should not be used. It provided no noticeable improvement in performance, because friction was sufficient to prevent slip, and it contributed to congestion in the column.
3. The mild reinforcement that is continuous across the interface should have an unbonded length there no shorter than $16d_b$ (8" in these tests.)
4. The detailing of the concrete at the top of the tube should be changed to minimize the cosmetic damage that occurred there. This could be achieved by a tapered transition from a hexadecagonal shape at the top of the steel shoe to an octagonal shape a few inches above the steel shoe.

8.3.2 Recommendations for Future Research

1. The addition of the steel shoe rocking feature resulted in minimal damage to the concrete, even at 10% drift ratio. However, both specimens described in this thesis represented column-footing connections. It is essential to develop and investigate experimentally the behavior of a comparable rocking detail for the column-cap beam connection.
2. Future tests should also investigate the possibility of delaying bar fracture by further increasing the unbonded length at the interface.

REFERENCES

ACI Committee 318. (2011). "Building Code Requirements for Structural Concrete and Commentary." *ACI 318-11*. American Concrete Institute, Farming Hills, MI.

Berry, M.P. and Eberhard, M.O. (2005). "Practical Performance Model for Bar Buckling." *Journal of Structural Engineering, ASCE*, Vol. 131, No 7, July 2005, pp. 1060-1070.

Berry, M.P., Parrish, M. and Eberhard, M.O. (2004). "PEER Structural Performance Database: User's Manual (Version 1.0)". Pacific Earthquake Engineering Research Center Report 2004, University of California, Berkeley, CA

Brown, W. (2008). "Bar Buckling in Reinforced Concrete Bridge Columns." Master's Thesis, University of Washington, Seattle, WA.

Building Seismic Safety Council for the FEMA. (2004). "NEHRP Recommended Provisions for Seismic Regulations for New Buildings and Other Structures (FEMA 450-1 / 2003 Edition)." National Institute of Building Sciences, Washington, D.C.

Chopra, A.K. (2007). "Dynamics of Structures – Theory and Applications of Earthquake Engineering, Third Edition". Pearson Prentice Hall, Upper Saddle River, NJ.

Cohagen, L.S., Pang, J.B.K., Eberhard, M.O. and Stanton, J.F. (2008). "A Precast Concrete Bridge Bent Designed to Re-center After an Earthquake." *Washington State Department of Transportations*. Report No. WA-RD 684.3, Washington State Department of Transportation, Olympia, WA.

Davis, P. M., Janes, Todd M., Eberhard, M.O., Stanton, J.F. and Haraldsson, O.S. (2012), "Unbonded Pre-tensioned Columns for Accelerated Bridge Construction in Seismic Regions," submitted to Journal of Bridge Engineering, ASCE.

Davis, P.M., Janes, T.M., Eberhard, M.O, and Stanton, J.F. (2011). *Unbonded Pre-Tensioned Columns for Bridges in Seismic Regions*. Pacific Earthquake Engineering Research Center Report 2011.

Elwood, K. and Eberhard, M. (2009). "Effective Stiffness of Reinforced Concrete Columns", *ACI Structural Journal*", Vol. 106, No. 4, July-August 200p, pp 476-484.

Fam, Amir, Frank S. Qie, and Sami Rizkalla (2004) "Concrete-Filled Steel Tubes Subjected to Axial Compression and Lateral Cyclic Loads", ASCE Journal of Structural Engineering, April, pp. 631-640.

Finnsson, G., Stanton, J.F., Eberhard, M.O. (2013) *Unbonded Pre-Tensioned Bridge Columns with Hybrid Fiber-Reinforced Concrete Shells.* Pacific Earthquake Engineering Research Center Report 2013.

Galeota D., Giammatteo M., and Marion R., (1992) "Strength and Ductility of Confined High Strength Concrete", Earthquake Engineering, Tenth World Conference, pp. 2609-2613

Haraldsson, O. and Berry, M. (2011). “Accelerating Bridge Construction to Reduce Congestion.” Transportation Northwest Final Report, TNW2011-08. University of Washington, Seattle, WA.

Haraldsson, O., Janes, T.M., Eberhard, M.O. and Stanton, J.F. (2011). “Laboratory Tests of Column-to-Footing Socket Connections”. *Highways for LIFE Technology Partnership Program*. Federal Highway Administration, Washington, DC.

Hieber, D., Wacker, J., Eberhard, M.O. and Stanton, J.F. (2005a). “Precast Concrete Pier Systems for Rapid Construction of Bridges in Seismic Regions.” *Washingon State Department of Transportation Report No. WA-RD-511.1*. Washington State Department of Transportation, Washington, 2005.

Khaleghi, B., Schultz, E., Seguirant, S., Marsh, L., Haraldsson, O., Eberhard, M.O. and Stanton, J.F. (2012). “Accelerated Bridge Construction in Washington State: From Research to Practice”. *PCI Journal*. Precast/Prestressed Concrete Institute, Fall, pp. 34-49.

Osanai, Y., Watanabe, F. and Okamoto, S., (1996) “Stress Transfer Mechanism of Socket Base Connections with Precast Concrete Columns”, ACI Structural Journal, American Concrete Institute, May-June, pp.266-276.

Ostertag, C.P., Jen, G. and Trono, W.(2013). “Self-Compacting Hybrid Fiber Reinforced Concrete Composites for Bridge Columns”. Cement and Concrete Composites. Submitted.

Pang, J.B.K., Eberhard, M.O. and Stanton, J.F. (2010). Large-Bar Connection for Precast Bride Bents in Seismic Regions. *Journal of Bridge Engineering, ASCE*, 15(3), 231-239.

Priestley M.J.N., Verma, R. and Xiao, Y., (1994), “Seismic Shear Strength of Reinforced Concrete Columns”, *Journal of Structural Engineering*, Vol. 120, No. 8, August 1994.

Roeder, C., Lehman, D., and Bishop, E. (2010). “Strength and Stiffness of Circular Concrete-Filled Tubes.” *J. Struct. Eng*., 136(12), 1545-1553.

Appendix A: Materials

This appendix includes extra information about the structural materials (conventional concrete, HyFRC and longitudinal reinforcing steel) used in this study.

Concrete

Two concretes were used in the test specimens: conventional concrete and HyFRC. Specimen PreT-SF-ROCK contained only conventional concrete whereas specimen PreT-SF-ROCK-HyFRC contained both conventional concrete and HyFRC. HyFRC is a referred to as a hybrid concrete, because it contains two types of fibers: steel, which increase the concrete's tensile strength, and polymer, which increase the concrete's ductility by minimizing crack opening. The steel fibers used in the mix were Dramix ZP 305, which have a length of 1.18", diameter of 0.02", tensile strength of 195 ksi and Young's modulus of 30,500 ksi (Bekaert 2010). A hook at each end improves the steel fibers' interlock with the rest of the concrete. The polymer fibers used in the mix were Kuralon RECS 15x8mm, which have a length of 0.31", tensile strength of 190 ksi, and Young's modules of 5,800 ksi (Kuraray 2012). The HyFRC was mixed at the University of Washington's structures lab in four equal batches. The mix proportions per batch are given in Table A.1. CalPortland, a local Seattle ready mix company, provided the conventional concrete.

The same mix design, outlined in Table A.2, was used for both the columns and footings, although batched on separate days; Finnsson used the same mix design for his specimens. The conventional concrete had two design goals: workability and early strength gain. The workability requirement stemmed from the horizontal casting of the column; gravity alone could not ensure that every space was filled.

The steel shoe feature compounded this problem because it limited visibility to verify whether the concrete did in fact fill every void within the shoe. It was important, however, to ensure that concrete did fill the steel shoe in its entirety for it to function properly. To achieve consolidation the concrete had a 9" slump on arrival and a small hole was also drilled at the top of the shoe. When concrete paste flowed out of this hole during casting, researchers felt confident that the concrete completely filled the shoe. The early strength criterion derived from the prestressing operation and schedule. In order to obtain the proper bond, the concrete needed to acquire a compressive strength of 5,000 psi before releasing the prestressed tendons without risking any slip. Due to the strict schedule, researchers wanted to release the strands as quickly as this requirement would allow. At the time of release, the concrete compressive strength exceeded 7,000 psi, well above the 5,000 psi criterion. Appendix A describes the strength gains of all concretes in more detail.

Table A.1 Design mix for one batch of HyFRC used in specimen PreT-SF-ROCK-HyFRC.

Material	Design Quanity
Fine Aggregate	104.3 lb
Pea Gravel	41.0 lb
Cement Type I/II	38.6 lb
Fly Ash	12.7 lb
ZP305 Steel Fiber	9.9 lb
RECS15	114.5 g
Water	16.9 lb
Viscosity-Modifying Admixture	0.4 oz
Superplasticizer	92.1 mL

Table A.2 Design mix for one cubic yard of concrete used for both column and footings.

Material	Design Quanity
Fine Aggregate	1240 lb
Pea Gravel	1940 lb
Cement Type I/II	752 lb
Water	240 lb
RECS15	30.0 oz
Water	30.0 oz

Concrete strength

This study contained three different concrete casts: column conventional concrete, column HyFRC, and footing conventional concrete. The strength history is provided, in tabular and graphical form, for all three of these casts.

Column concrete

Table A.3 Column conventional concrete compressive strength history.

Day	Strength [psi]
7	7677
8	7288
14	7506
28	8388
79	10273
90	9894

***Note: Day 8= release of prestressing strands, Day 79= PreT-SF-ROCK test day, Day 90= PreT-SF-ROCK-HyFRC test day**

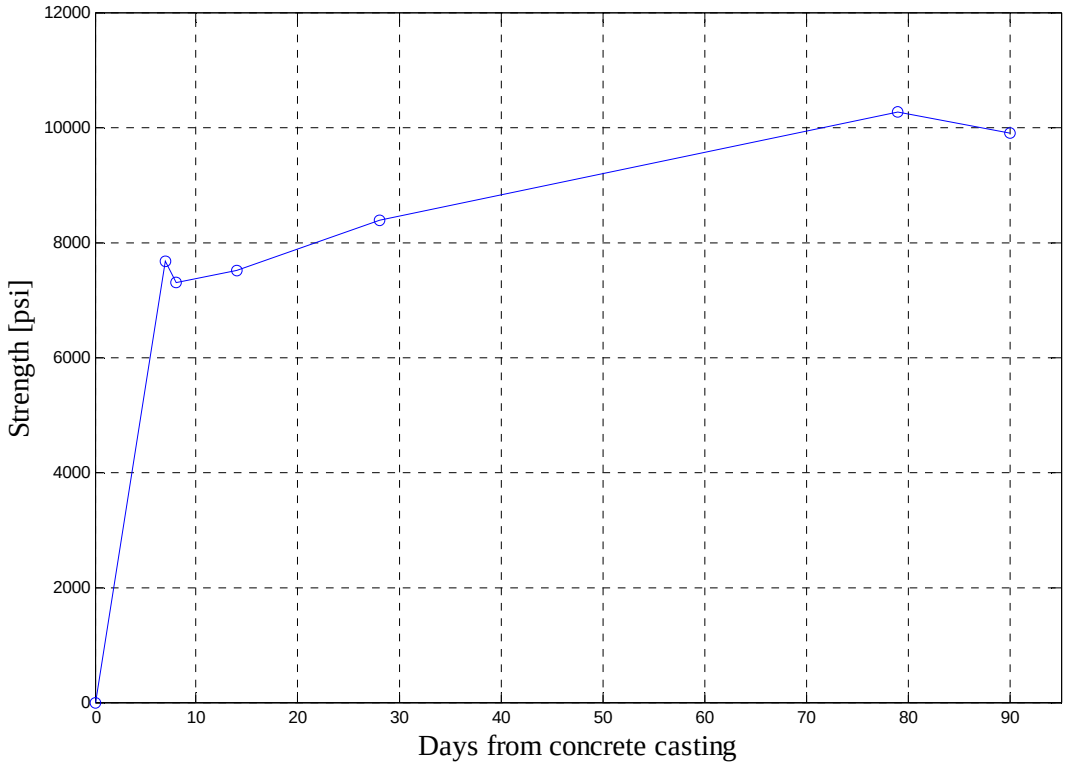

Figure A.1 Column conventional concrete compressive strength history.

Table A.4 Column conventional concrete E-MOD history.

Day	Strength [ksi]
8	3464
79	3747
90	3881

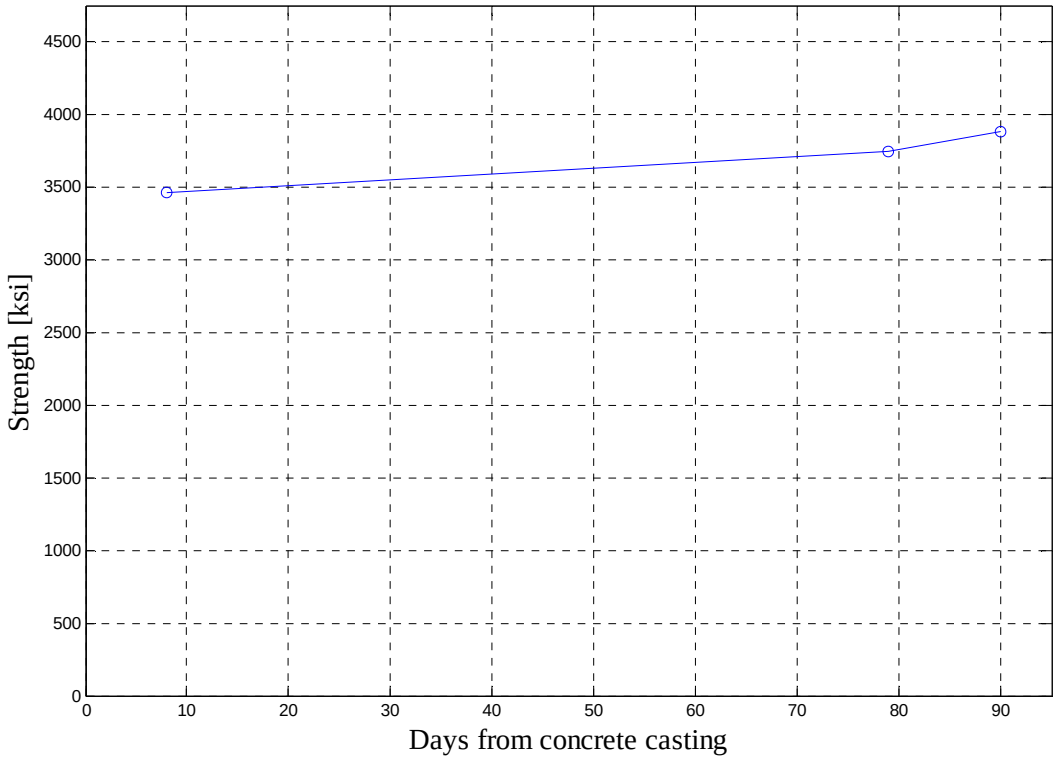

Figure A.2 E-MOD history for the column conventional concrete.

Table A.5 Column conventional concrete tensile strength

Day	Strength [psi]	Strength/f'_c
90	673	6.8%

Table A.6 HyFRC compressive strength history.

Day	Strength [psi]
7	6400
10	7150
14	7915
28	8685
92	10203

***Note: Day 10= release of prestressing strands, Day 92= PreT-SF-ROCK-HyFRC test day**

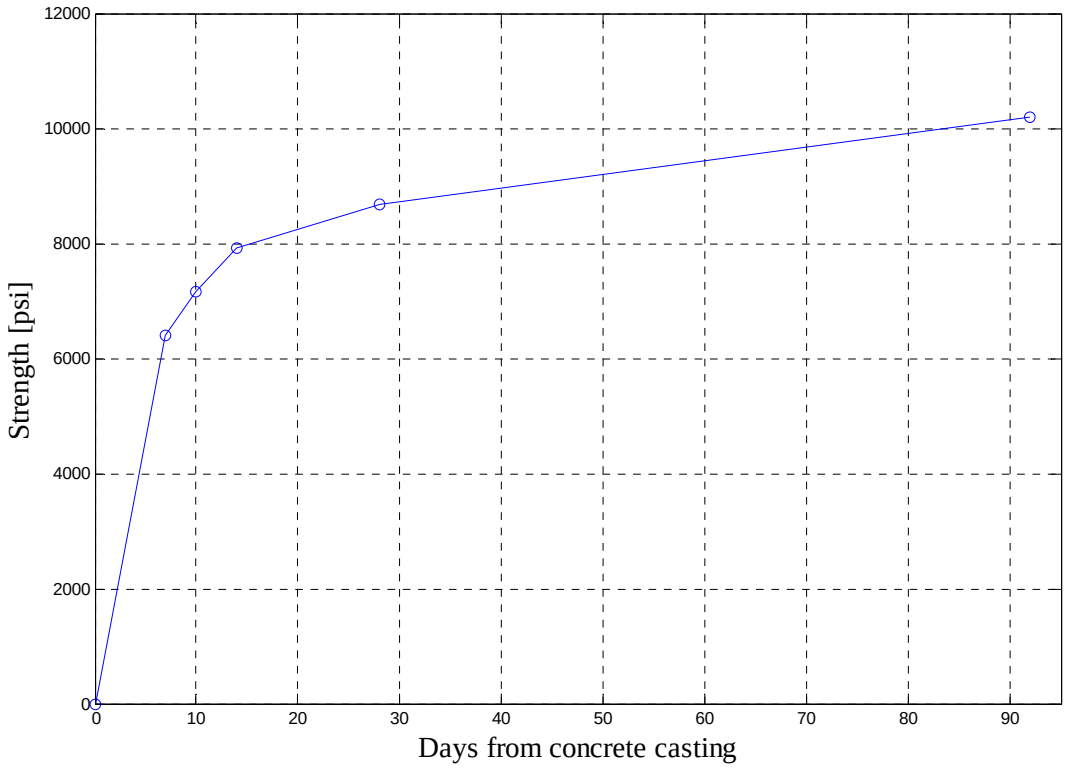

Figure A.3 HyFRC compressive strength history.

Table A.7 HyFRC E-MOD history.

Day	Strength [ksi]
8	3535
28	4491
92	4496

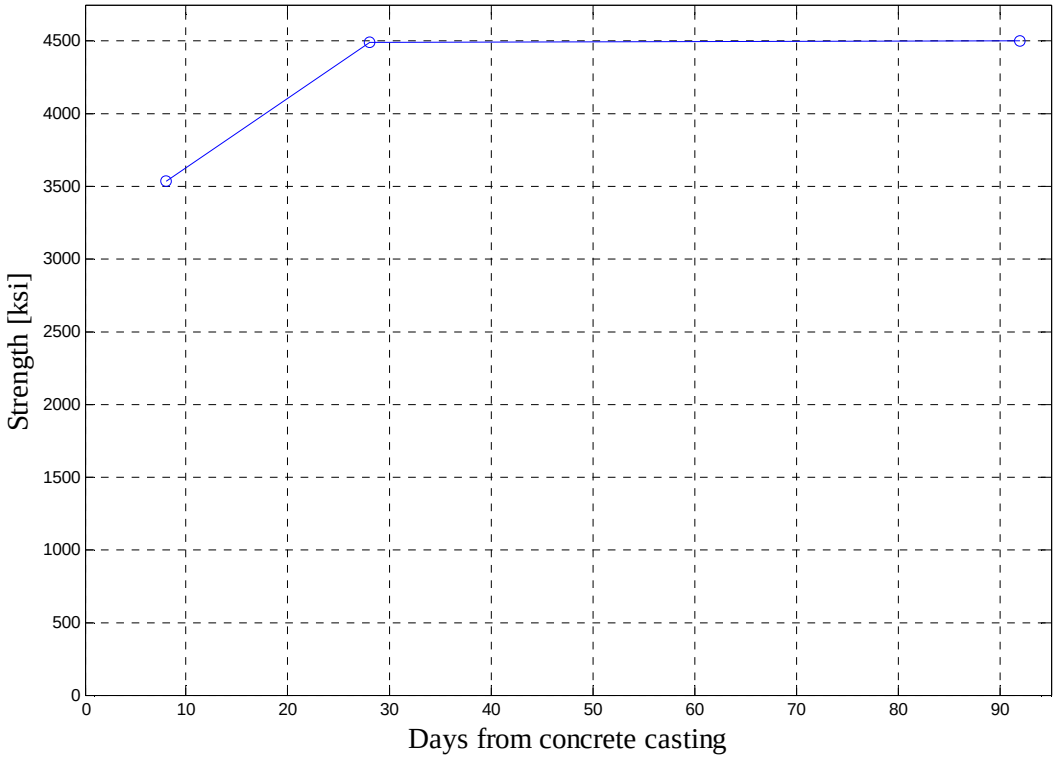

Figure A.4 E-MOD history for the HyFRC.

Table A.8 HyFRC tensile strength

Day	Strength [psi]	Strength/f'_c
92	1452	14.2%

Footing concrete

Table A.9 Footing conventional concrete compressive strength history

Day	Strength [psi]
7	6225
14	6822
28	8890
35	9022
46	9326

***Note: Day 35= PreT-SF-ROCK test day, Day 46= PreT-SF-ROCK-HyFRC test day**

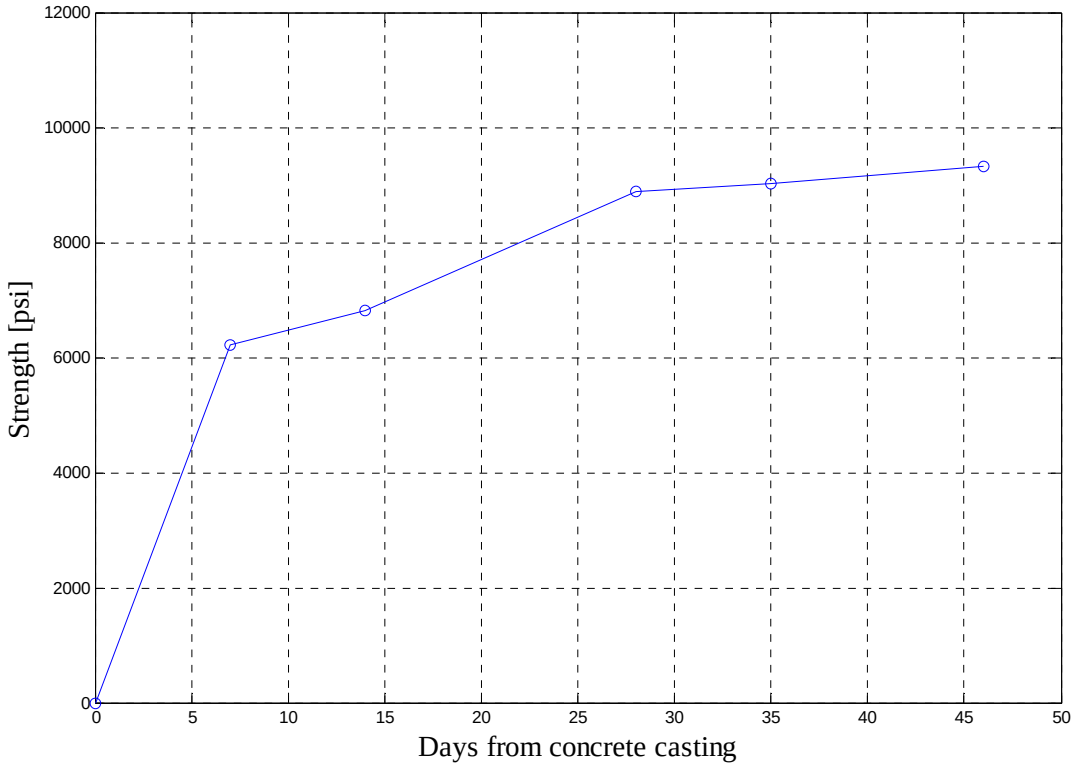

Figure A.5 Footing conventional concrete compressive strength history.

Table A.8 Footing conventional concrete tensile strength

Day	Strength [psi]	Strength/f'_c
92	1452	14.2%

Steel

In both columns, all longitudinal mild reinforcement bars satisfied ASTM A706 Gr. 60 per seismic design requirements. The footing, however, did contain some A615 steel, an unavoidable circumstance, because No. 3 bars were needed but unavailable in A706. Although A615 is less ductile that A706, its use was deemed acceptable since the No. 3 bars were expected to remain elastic. Furthermore, the No. 3 bars were located at the top of the footing where they would experience minimal compression and could share the load with the surrounding concrete. The prestressing strand in this study was the same used in Finnsson et al. (2013) and Davis et al. (2011). The strand was 3/8" in diameter and coated in epoxy to improve its resistance to corrosion. Jimenez (2012) showed that the low-slip bond strength of epoxy-coated strand is nearly identical to that of black (i.e.,, uncoated) strand.

Spiral made from No. 3 gauge smooth steel wire provided the columns' transverse reinforcement. The spiral had a cross-sectional area of 0.041 $in.^2$, pitch of 1.25" and an outer diameter of 18 5/16". This meant the cover in the test specimens was 13/16", corresponding to a typical 2" cover at full scale. Due to the steel shoe, the spiral was discontinuous at the column-footing interface. The spiral terminations on either side of this location adhered to ACI requirements, consisting of three closely spaced turns followed by a bend that extended into the columns' core. The same method was used for the spiral terminations at the top and bottom of the columns. Spiral reinforcement also confined the prestressing strands at the top of the column where they were bonded. The spiral used in this reinforcement had the same specifications as that used for the longitudinal reinforcement except that its spun diameter was 8".

A36 steel was used for all components of the steel shoe and dowel cup, whereas higher strength steel, Gr. 80, was used for the dowel bar to minimize its required size.

Reinforcing Steel

Below are the stress-strain relations plots for the steel reinforcement used in both specimens.

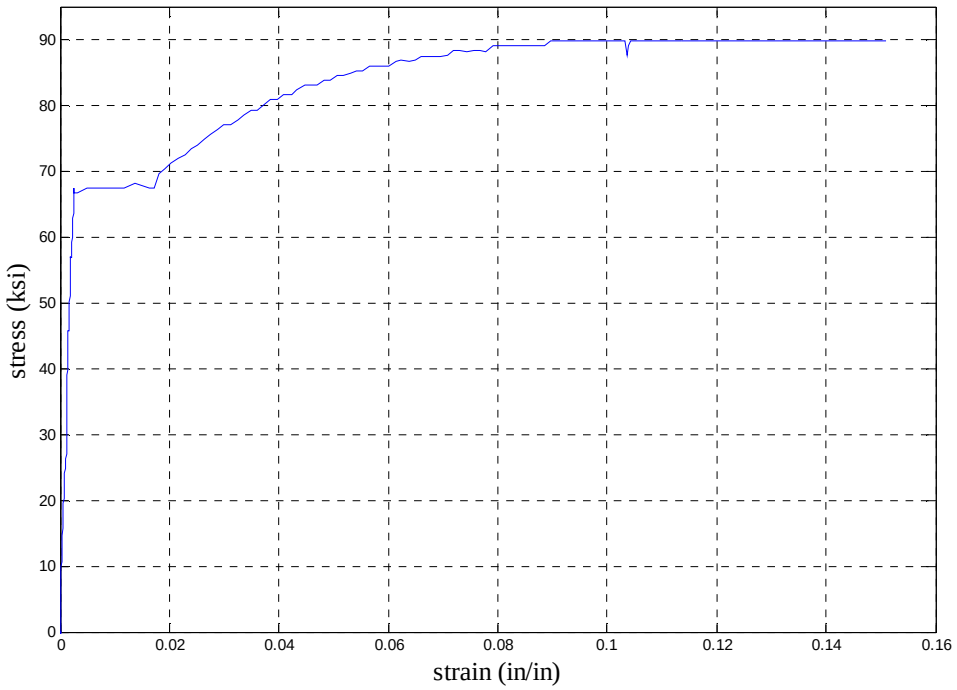

Figure A.6 Stress-strain relations for #4 reinforcement.

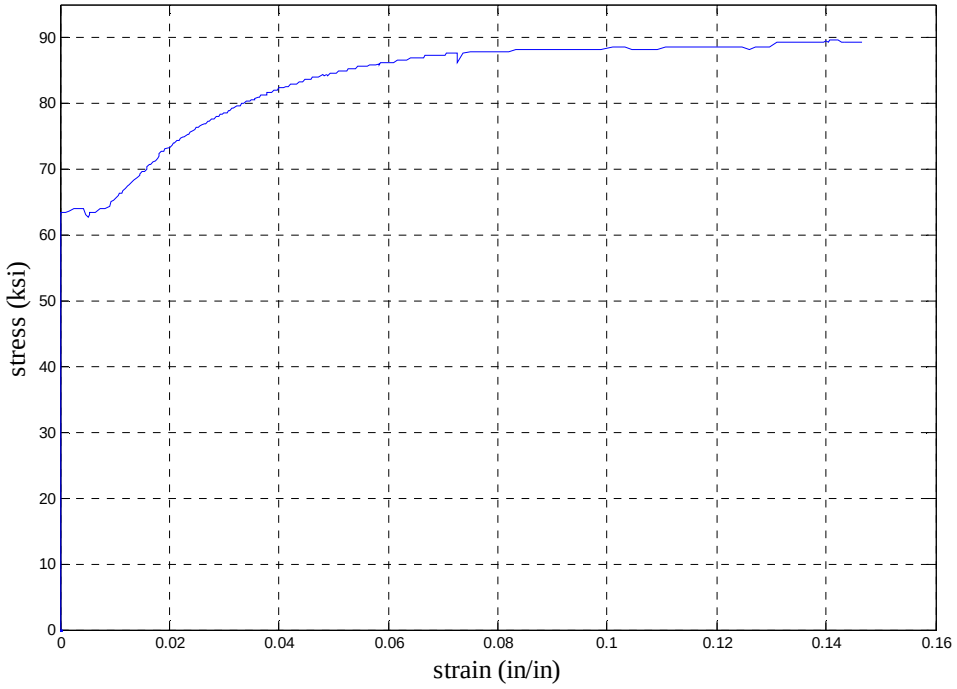

Figure A.7 Stress-strain relations for #6 reinforcement.

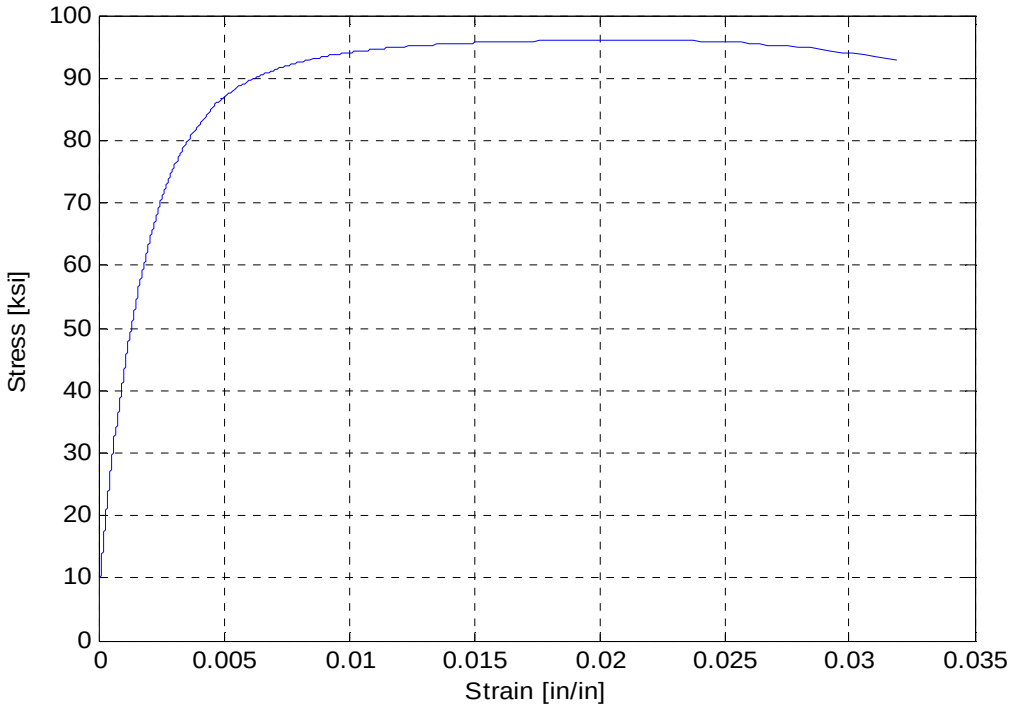

Figure A.8 Stress-strain relations for 3 gauge spiral reinforcement.

Appendix B: Specimen Drawings

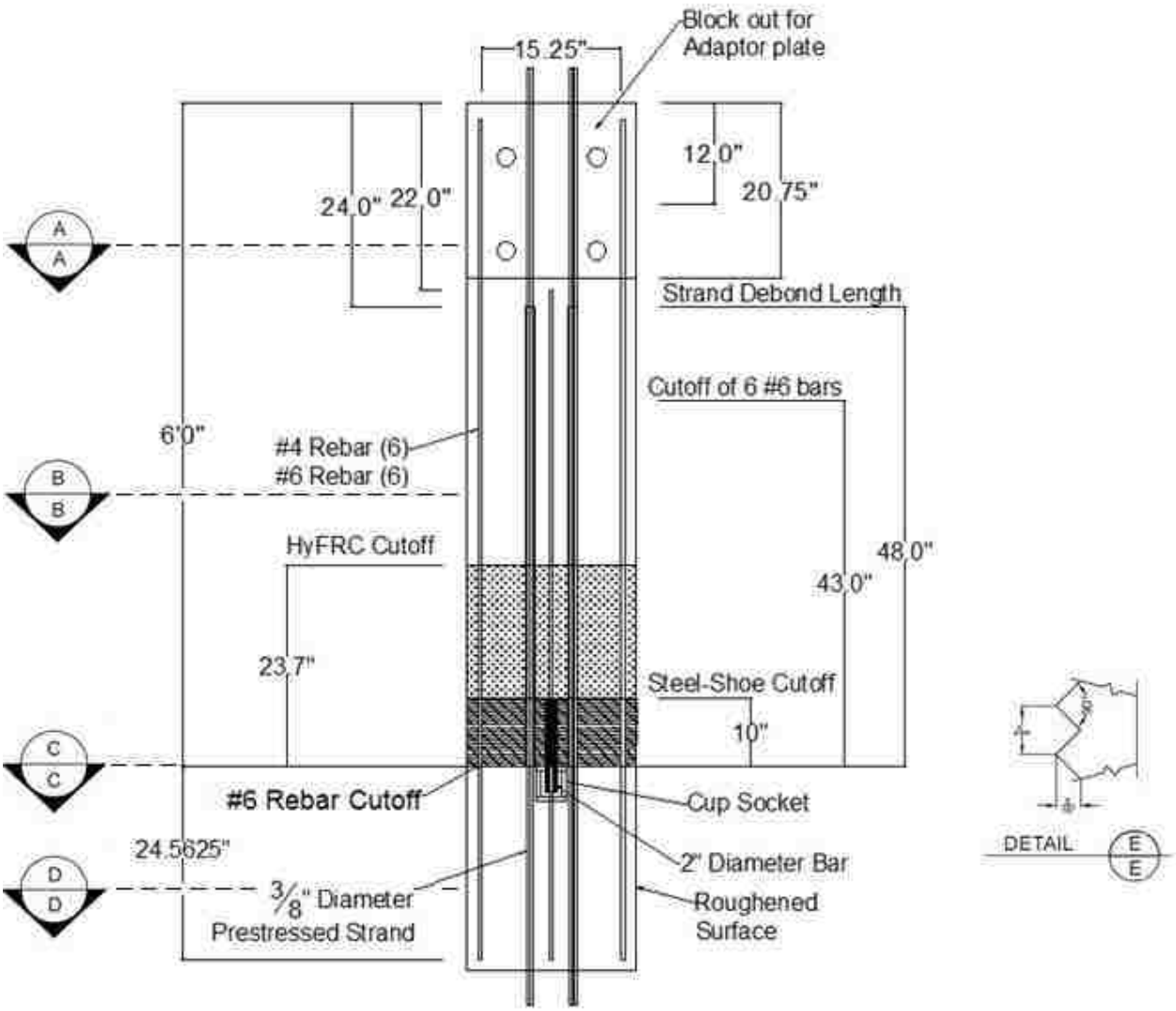

Figure B.1 Column elevation.

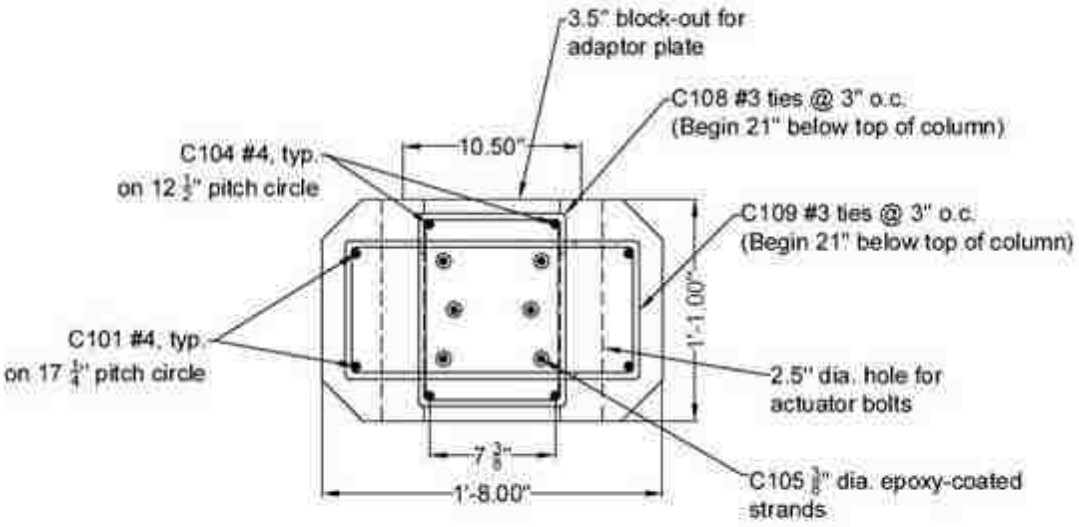

Section A
A

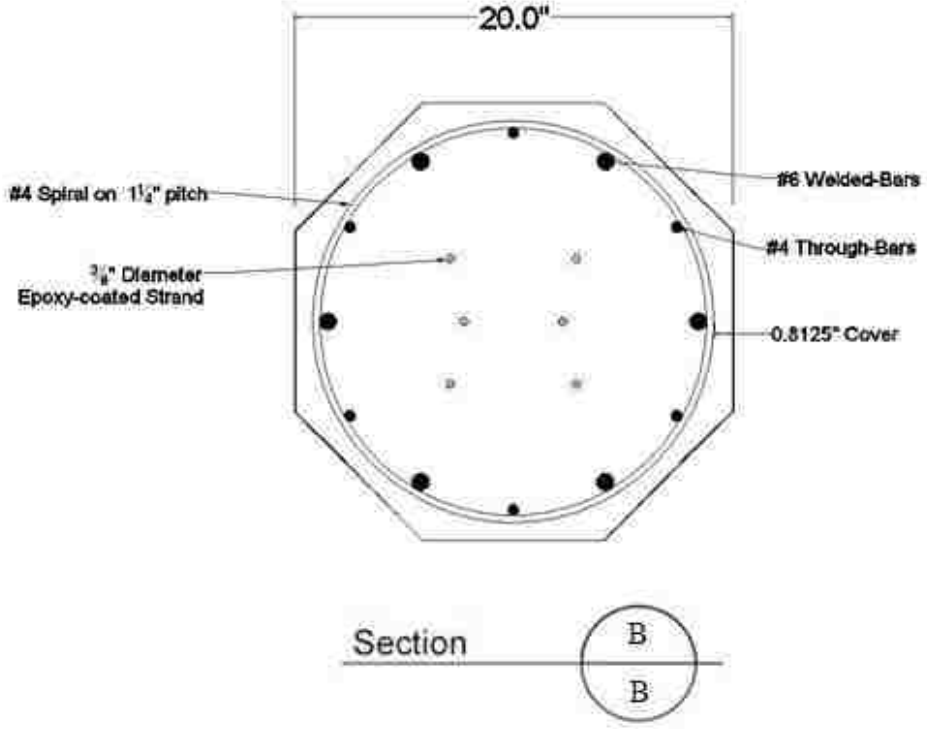

Section B
B

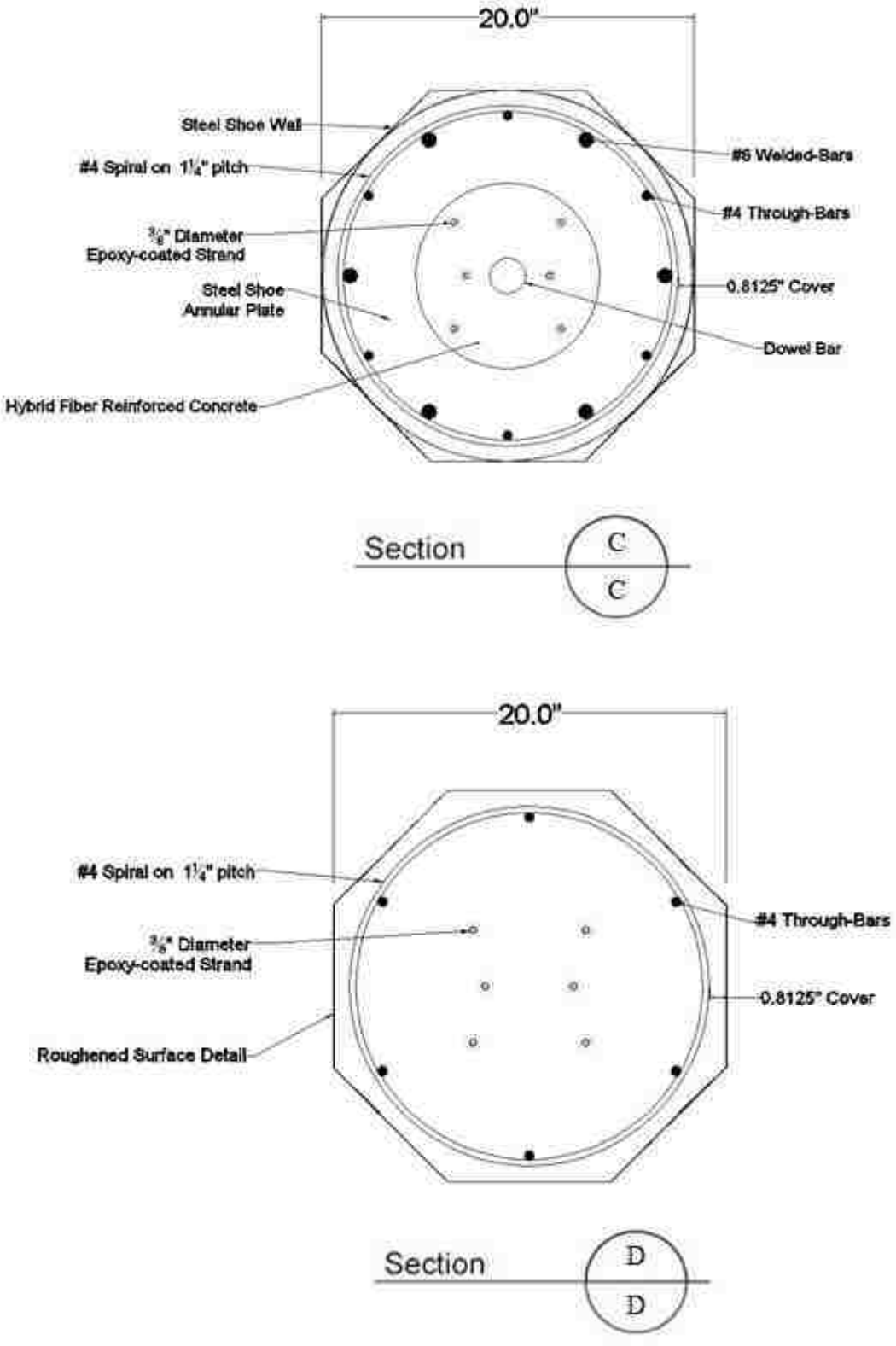

Figure B.2 Column cross-sectional views.

Dimensions											
Quantity	Bar Size	Shape	A	B	C	Special Notes					
14	#6	Straight	43"	-	-						Longitudinal Short Bars
14	#5	Straight	73.5"	-	-						Footing Bars
18	#5	Straight	65.5"	-	-						Footing Bars
8	#4	Straight	93 1/4"	-	-	Lenton Terminator Heads on One side					Longitudinal Long Bars
2	#4	Straight	93 1/4"	-	-						
4	#4	Straight	72 1/2"	-	-	Lenton Terminator Heads on One side					Longitudinal Long Bars
4	#4	Straight	55"	-	-						Footing Bars
8	#4	Straight	37"	-	-						Longitudinal Bars (Top of Column)
14	#3	Straight	73.5"	-	-						Footing Bars
18	#3	Straight	65.5"	-	-						Footing Bars
4	#3	Straight	55"	-	-						Footing Bars
8	#3	Rectangle	-	8 5/8"	11"	135° hook stirrups					Actuator Blockout Stirrups
8	#3	Rectangle	-	16 3/4"	9"	135° hook stirrups					Actuator Blockout Stirrups

Shapes:

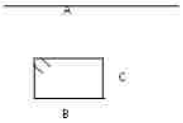

Straight

Rectangle *Dimensions are Outside Diameter

Quantity	Shape	Length	
1	HSS20.000x0.500	8.00"	A36
1	HSS3.500x0.250	3.00"	A36
1	Bar A	11.00"	80 ksi yield
1	Annular Plate A	-	A36
1	Annular Plate B	-	A36
1	Annular Plate C	-	A36

Figure B.3 Steel schedule for both specimens.

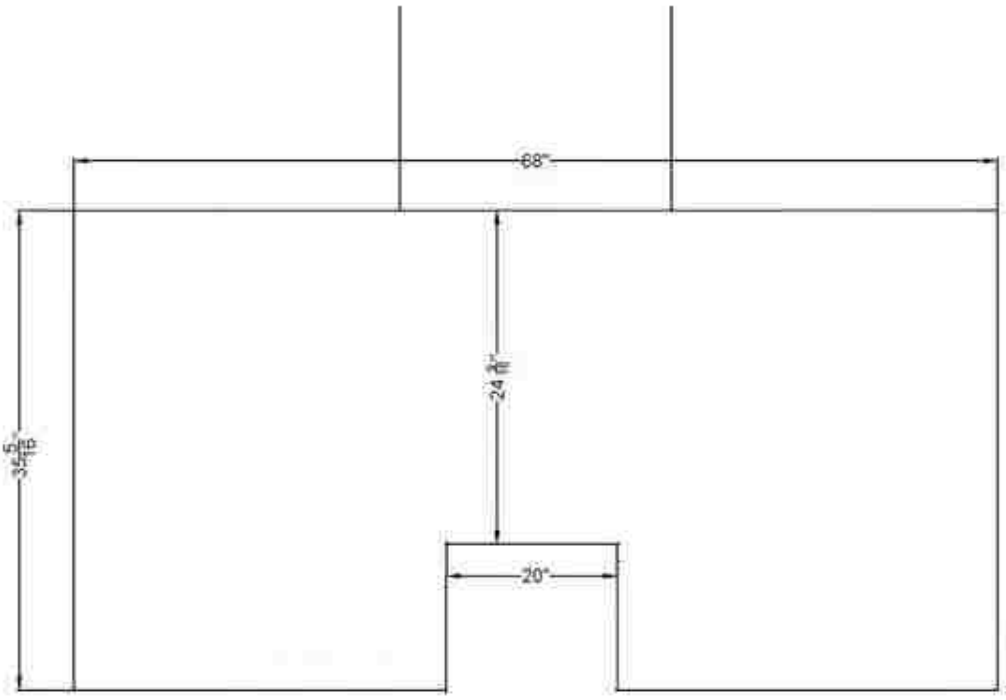

Figure B.4 Footing dimensions, profile view.

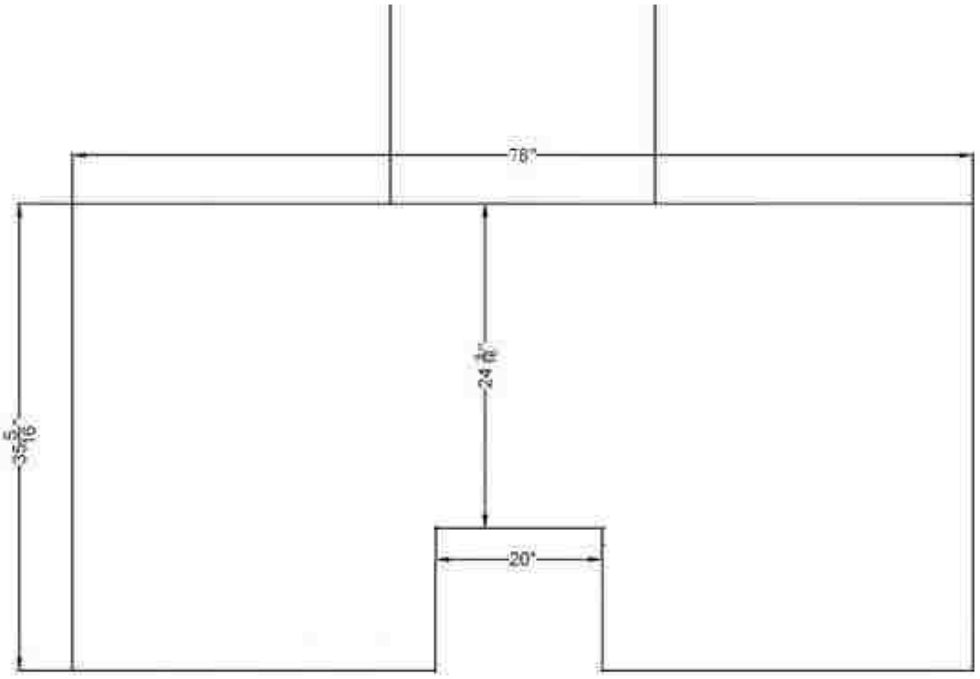

Figure B.5 Footing dimensions, transverse view.

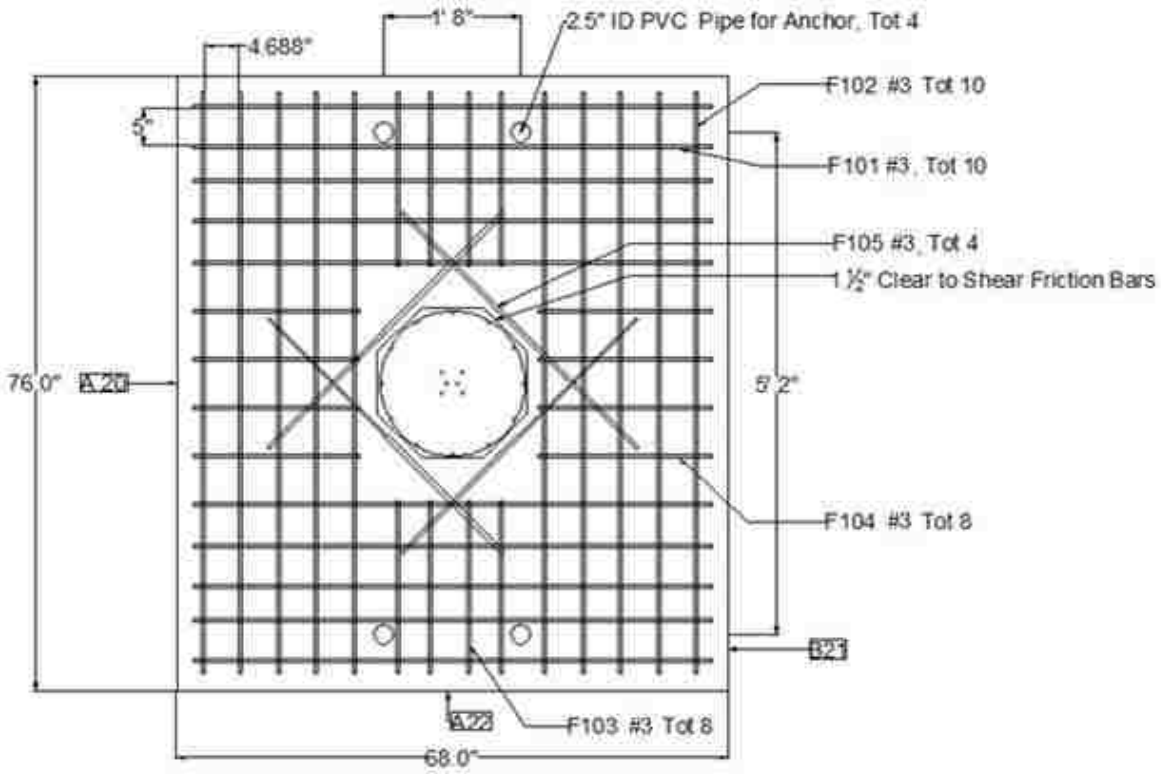

Figure B.6 Footing top mat.

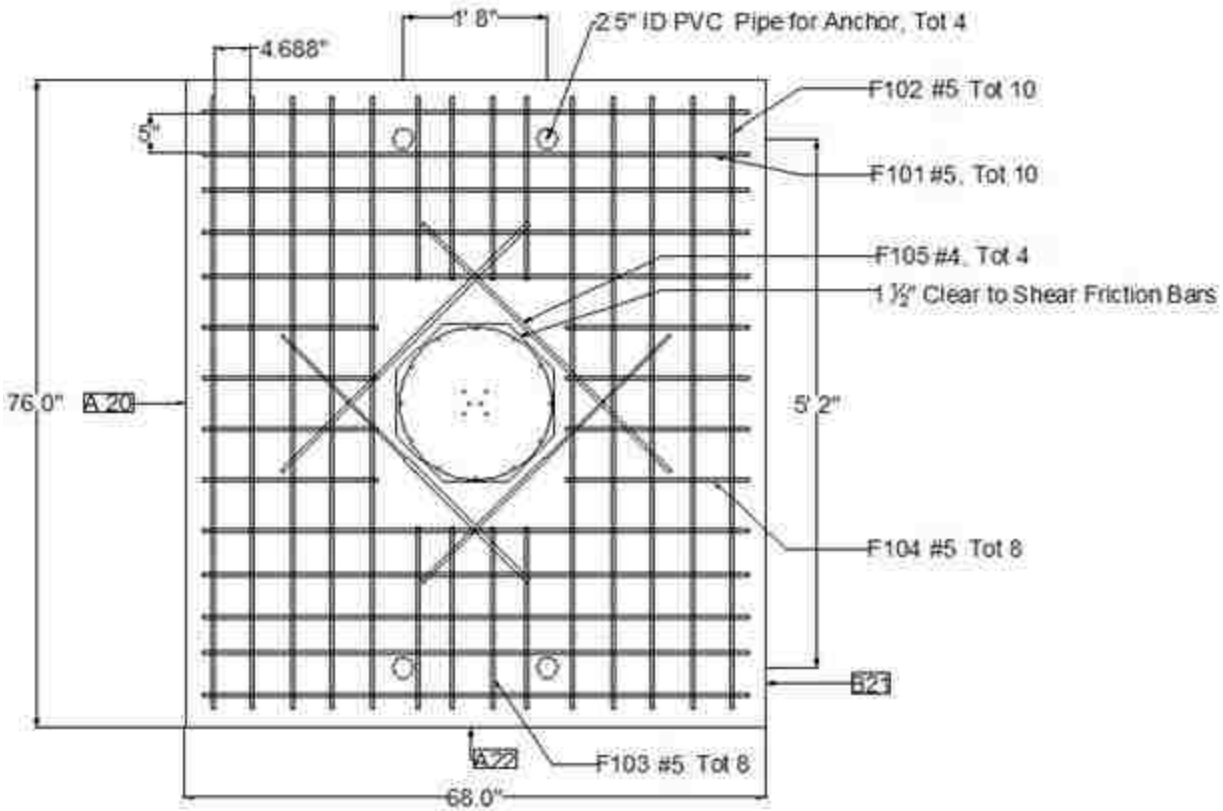

Figure B.7 Footing bottom mat.

Appendix C: Test photos

PreT-SF-ROCK-HyFRC

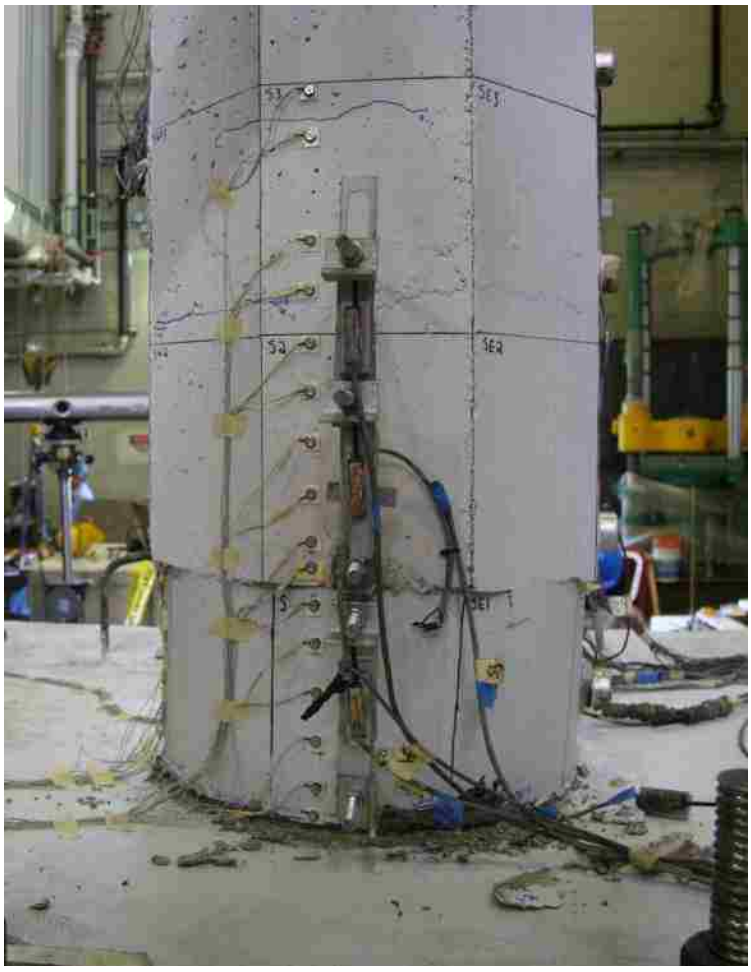

Figure C.1 South view after 6% drift, cycle 9-1.

Figure C.2 Footing fillet-spalling.

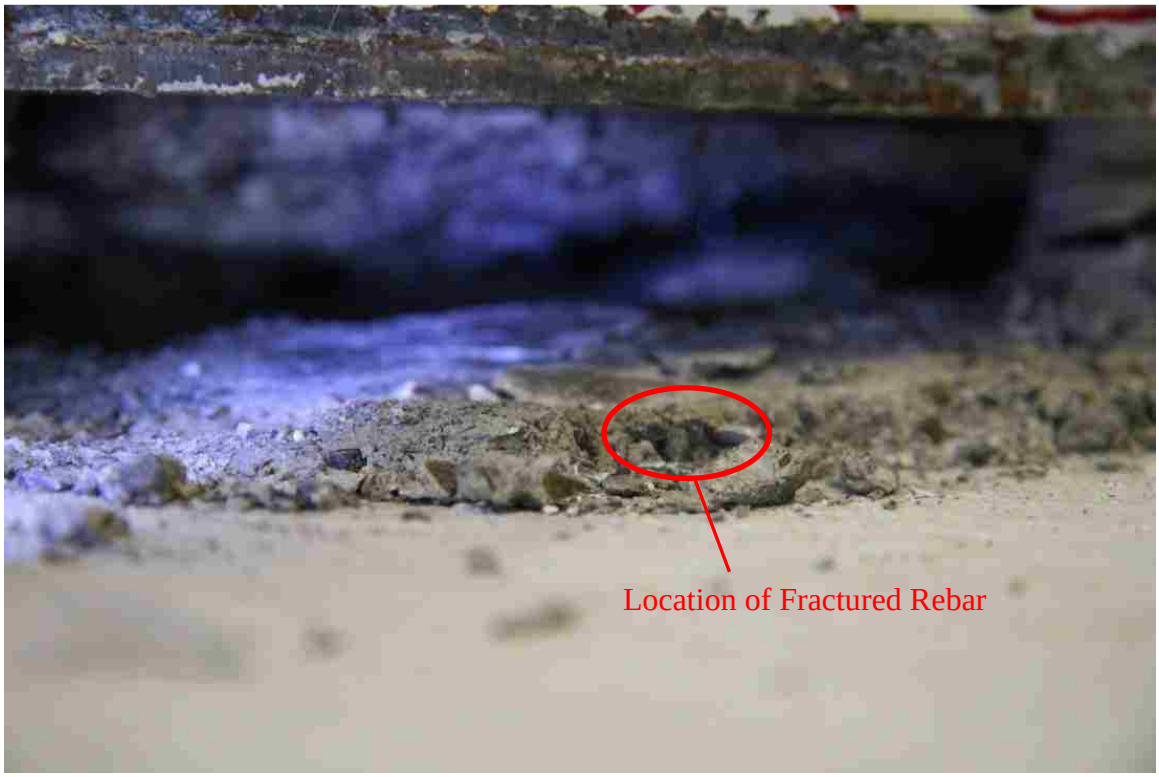

Figure C.3 Fractured Rebar, cycle 9-1.

Figure C.4 Fractured Strand, cycle 9-2.

Figure C.5 End of test.

Figure C.6 Bottom of shoe after testing.

Figure C.7 Top of footing after testing.

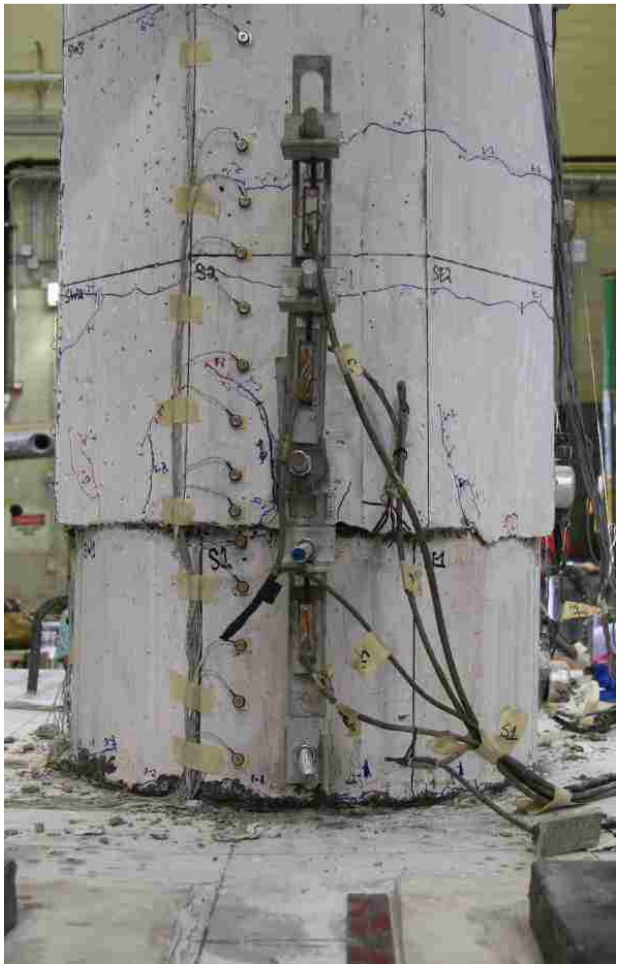

Figure C.8 South View after 6% drift.

Figure C.9 Cosmetic spalling at top of shoe.

Figure C.10 Footing fillet-spalling.

Figure C.11 Exposure of rebar.

Figure C.12 Fracture of rebar.

Figure C.13 End of test.

Appendix D: Construction

HyFRC Pour

Since PreT-SF-ROCK-HyFRC contained both conventional concrete and HyFRC, two separate pours were required, an issue also experienced in Finnsson's columns. Finnsson addressed this issue by constructing two separate forms: one for a HyFRC shell and the other for the remainder of the column. Finnsson first poured HyFRC into the shell mold, and then after curing inserted it into the greater formwork for the conventional concrete pour. This scheme resulted in a cross-section at the HyFRC region depicted by Figure D.1.

This solution, however, was deemed inadequate because it was very labor-intensive and demanded low tolerances to achieve a proper fit of the concrete shell into the main form. As a result, this study used a new approach. Rather than construct two separate forms, workers created a single form and inserted a dividing mesh at the appropriate HyFRC cutoff levels (Figure D.2). Before implementing this method, researchers conducted a test pour on a foot-length section of equal geometry as the test specimen. The concern was that during vibration the mesh would leak an unacceptable amount of cement paste; however, the mesh proved fine enough that it withheld the HyFRC even after vibration. Some cement paste did seep through the mesh but it was not excessive. Prior to pouring the conventional concrete, laborers quickly chiseled out the overflow of paste. Figure D.3 shows specimen PreT-SF-ROCK-HyFRC after the HyFRC pour but before the conventional concrete pour.

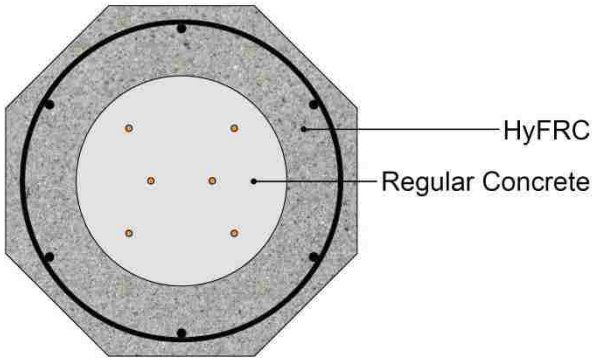

Figure D.1 Section through the column at the level of the HyFRC shell, Finnsson et al. (2013).

Figure D.2 Dividing mesh used to separate the HyFRC and conventional concrete pours (Image before casting).

Figure D.3 Dividing mesh used to separate the HyFRC and conventional concrete pours. (Image after casting).

Effective Prestressing force

All twelve strands were stressed on the same day using a 100 kip hydraulic ram powered by an electric pump. Each strand was stressed individually in a star pattern in order to equalize the stress on the rig. The target stress was 170 ksi, which corresponds to 14.45 kips per strand. This is the same stress used by Finnsson in his specimens. The strands were monitored continuously after stressing. The following day, the strands had an average force of 13.05 kips or an average stress of 153.5 ksi. To correct for the stress loss, the strands were re-stressed to the appropriate level. After casting, the strands were not released until the concrete compressive strength had exceeded 5,000 psi to prevent any strand slip. Prior to release, the strands displayed an average force of 14.66 kips (172.5 ksi). This led to a total compressive force of 87.96 kips on each column.

Using the measured modulus of elasticity of both the conventional concrete and HyFRC at release (3464 ksi and 3535 ksi respectively), the initial elastic loss in each strand was calculated as 2.2 ksi. Next, the creep loss was estimated as twice the elastic loss or 4.4 ksi per strand. Lastly, a 300 micro-strain was assumed to approximate the losses due to shrinkage, which equated to an additional loss of 9.0 ksi per strand. In all, the total losses were estimated at 15.6 ksi, yielding an effective stress of 156.9 ksi per strand and an effective stress of 241 psi in the concrete. These results are summarized in Table D.1

Table D.1 A summary of prestressing losses upon release and the resultant effective stresses.

Type	Stress Loss [ksi]	Stress in Strand [ksi]
Initial Jacking		172.5
Elastic shortening loss	2.2	170.3
Creep loss	4.4	165.9
Shrinkage loss	9.0	156.9